

Scanning Tunneling Spectroscopy of Graphene and Magnetic Nanostructures

by

Victor Watson Brar

A dissertation submitted in partial satisfaction of the

requirements for the degree of

Doctor of Philosophy

in

Physics

in the

GRADUATE DIVISION
of the
UNIVERSITY OF CALIFORNIA, BERKELEY

Committee in charge:

Professor Michael F. Crommie, Chair

Professor Feng Wang

Professor Ali Javey

Fall 2010

Scanning Tunneling Spectroscopy of Graphene and Magnetic Nanostructures

Copyright 2010

by

Victor Watson Brar

Abstract

Scanning Tunneling Spectroscopy of Graphene and Magnetic Nanostructures

by

Victor Watson Brar

Doctor of Philosophy in Physics

University of California, Berkeley

Professor Michael F. Crommie, Chair

This dissertation is divided into two parts, both of which describe measurements where a scanning tunneling microscope (STM) is operated to perform measurements of novel physical systems. In the first section I describe spin-polarized STM (SP-STM) measurements on individual adatoms on a ferromagnetic surface. The aim of the first section is to illustrate how a SP-STM can be used to probe magnetic phenomena at the atomic scale. After describing the explicit details of the SP-STM apparatus, I explain how to use SP-STM to study the magnetic coupling of different 3d adatoms (Fe, Cr and Cu) to a ferromagnetic surface. It is shown that the SP-STM is capable of distinguishing which species couple ferromagnetically vs. anti-ferromagnetically to the surface. The second section describes STM measurements performed on a graphene surface equipped with a back-gate electrode that can be used to vary the charge density of the graphene *in situ*. These measurements represent the first time an STM has been capable of measuring a gate-tunable surface, and this section describes the extra experimental and theoretical considerations that are required to set up such an experiment and accurately interpret the data. It is shown that electrons tunneling into graphene include a strong, phonon-mediated inelastic signal, and that an STM tip can be an invasive probe of graphene. After showing how to account for these effects, STM experiments are presented that examine (1) how impurities effect the large scale electronic structure of graphene, (2) how the quasiparticle lifetime in graphene depends on charge density, and (3) how Co adatoms can be reversibly ionized on graphene through the use of a back-gate electrode.

Contents

1	Introduction.....	- 1 -
1.1	Spin-Polarized STM.....	- 1 -
1.2	STM on Graphene.....	- 2 -
1.3	Outline of thesis.....	- 3 -
2	STM theory and operation.....	- 5 -
2.1	Bardeen and Tersoff-Hamann model for tunneling	- 5 -
2.1.1	Tunneling matrix element - s-wave tunneling	- 7 -
2.1.2	Tunnel current and conductance (dI/dV)	- 9 -
2.1.3	Tunneling into 2D Bloch states	- 11 -
2.2	STM Basics	- 12 -
2.3	UHV.....	- 14 -
3	Spin-Polarized STM.....	- 16 -
3.1	Motivation.....	- 16 -
3.2	SP-STM Fundamentals.....	- 16 -
3.3	Preparation of SP-STM Tip	- 19 -
3.3.1	Etching and annealing W tip.....	- 19 -
3.3.2	Cr film growth on annealed tip	- 22 -
3.3.3	Checking for spin polarization.....	- 24 -
3.3.3.1	Co islands on Cu(111) – non SP characterization	- 24 -
3.3.3.2	Spin-polarized dI/dV – normalization and contrast.....	- 25 -
3.3.3.3	Poking and Pulsing SP-tip - obtaining good contrast.....	- 29 -
3.4	SP-STM Measurement of Cr and Fe Adatoms on Co islands.....	- 31 -
3.5	SP-STM Measurement of Cu and Fe Adatoms on Co islands	- 36 -
3.6	Conclusions	- 37 -
4	STM on Graphene.....	- 39 -
4.1	Motivation.....	- 39 -
4.2	Graphene basics	- 40 -
4.2.1	Band-structure	- 40 -
4.2.1.1	Psuedospin	- 44 -
4.2.1.2	σ – bands	- 44 -
4.3	Graphene synthesis and sample mounting/annealing.....	- 45 -
4.3.1	Overview	- 45 -
4.3.2	Mechanical exfoliation (“peeling”) of monolayer graphene.....	- 46 -
4.3.3	Graphene production by CVD on Cu foils	- 48 -
4.3.4	Sample mounting and UHV annealing	- 49 -
4.4	STM measurements on graphene	- 51 -
4.4.1	Outline	- 51 -
4.4.2	STM-Graphene challenges	- 52 -

4.4.2.1	Quantum Capacitance and Tip-induced band bending.....	- 52 -
4.4.2.2	Tip Calibration	- 57 -
4.4.3	Gate-dependent STS on graphene – phonon assisted tunneling	- 58 -
4.4.4	Observing many-body effects in graphene via tunneling spectroscopy.....	- 69 -
4.4.4.1	Introduction	- 69 -
4.4.4.2	Many-body effects on graphene STS spectra.....	- 70 -
4.4.4.3	Conclusion	- 77 -
4.4.5	Charge density fluctuations in Graphene	- 77 -
4.4.5.1	Introduction	- 77 -
4.4.5.2	Charge puddles and back-scattering in graphene/SiO ₂	- 78 -
4.4.5.3	Conclusion	- 84 -
4.4.6	STS of adsorbates on graphene.....	- 85 -
4.4.6.1	Introduction	- 85 -
4.4.6.2	Observing Gate-controlled ionization of Co adatoms on graphene using STS	- 85 -
4.4.6.3	Conclusion	- 92 -
References	-93-

List of Abbreviations

2DEG	Two dimensional electron gas
CVD	Chemical Vapor Deposition
DFT	Density functional theory
<i>dI/dV</i>	Differential Conductance
DOS	Density of States
E _f	Fermi Energy
FWHM	Full Width at Half Maximum
FT	Fourier Transform
IETS	Inelastic Electron Tunneling Spectroscopy
LDOS	Local Density of States
LT	Low Temperature
LHe	Liquid Helium
LN ₂	Liquid Nitrogen
OFHC	Oxygen Free High Conductivity
STM	Scanning Tunneling Microscopy <i>or</i> Scanning Tunneling Microscope
STS	Scanning Tunneling Spectroscopy
UHV	Ultra High Vacuum

Acknowledgments

This work reflects the efforts of a lot of people who directly contributed to it and also made my life a lot of fun while it was going on. I would first and foremost like to thank Prof. Mike Crommie who has been a terrific advisor throughout my time here at Berkeley. It has always been important to Mike that I understand the principles behind the experiments we have worked on, and through his encouragement and tutoring I have learned a lot of physics. He has always made time for me to discuss physics questions or anything I might need, and he has always helped me get over a hump when I have been stuck. Through six years of his tutoring I have learned the importance of being a critical thinker and a clear presenter, and I am very grateful to have had him as an advisor.

I have also been fortunate to work with two outstanding post-docs who I learned a lot from while I was here and who contributed significantly to the work presented in this thesis. Yossi Yayon was the first person I worked with when I came to Berkeley and we spent a lot of time together getting the spin-polarized STM working. I learned a lot of good experimental technique from him, and I learned the importance of being persistent. He was extremely patient and helpful with me while I was learning the basics of STM and UHV systems, and he made sure I learned them well. Yuanbo Zhang was the second post-doc I got to work with, and we performed most of the graphene work in this thesis together. Yuanbo was a terrific advisor and a good friend who spent a lot of time teaching me basic physics and device fabrication stuff. He was big optimist and never backed down from any problems or perceived difficulties. These qualities made him a big inspiration to me and I feel extremely lucky to have gotten to work with him.

In addition to those two post-docs, there are a number of other co-workers who contributed to this work and who I have had a great time working with. Melissa Panlasigui did much of the early dirty work we needed to fabricate the graphene devices, and later on she performed many of the difficult spectroscopy measurements and did a lot of the data analysis on the graphene samples. She was always up for any challenge and has always had a very positive attitude that made her an absolute pleasure to work with. Cheol-Hwan Park, Sebastian Wickenburg and Tim Wehling performed many of the difficult calculations we needed to understand the graphene data. I spent many hours with them trying to figure out what it all meant, and I learned a great deal through those discussions. Cheol has also been helpful with a lot of my non-graphene related questions throughout my time here, and I am a big beneficiary of his patience and clear explanations. Hans-Michael Solowan, Regis Decker and Yang Wang also provided a great deal of help in obtaining and understanding the graphene data. Long discussions with them - and a lot of data taking by them - helped put a clear picture together for the Co adatom study. Kevin Chan and Hoonkyung Lee performed many of the difficult calculations we needed to understand many aspects of the Co adatom data. Finally, Xinghua Lu did much of the early fabrication and development of the spin-polarized STM. His hard work led to our future success with that experiment.

There were also a number of professors who helped us understand this data and took their time to explain things clearly to me. Prof. Feng Wang helped immensely in our understanding of the “phonon-floodgate” phenomena we observed in our data, and has

also answered numerous other questions that I have had during my time here. Prof. Dung-Hai Lee also spent many hours with us trying to figure out the early graphene data. Alexander Balatsky has been a great help in understanding the many-body phenomena we observed in the graphene data, and he has provided us with many ideas for future measurements. I have learned a lot through discussions with him and really appreciate his unique way of approaching problems. Professors Steve Louie, Marvin Cohen and Steve Erwin also provided explanations, ideas and support for much of the work shown here.

There have been a number of other people in the lab who I have learned a lot from and have been lucky to get to work around. Post-doc's Daniel Wegner, Yayu Wang, Chenggang Tao and Armen Kirakosian all provided me with a great deal of useful advice and ideas throughout my time here. Ryan Yamachika provided a lot of expertise and late night support with our experiments that helped us solve a lot of our problems. It has also been a pleasure to work in the same lab with graduate students Xiaowei Zhang, Niv Levy and Marilena Longobardi who have provided a lot of useful and/or fun discussions. A number of undergrads have also assisted me in the lab including Lorenzo Maserati (CVD graphene), Steve Sharma (magnetic molecules), Daniel Wiengarten (sp-stm), Yasaman Bahri (magnetic molecules), Brandon Giles (exfoliated graphene), Kunal Suhasrabuddhe (sp-stm), Dillon Wong (writing thesis) and Drew Edelberg (PtIr tips).

My graduate student work here could not have been completed without additional departmental help from Anne Takizawa and Donna Sakima. They kept me on the ball in terms of meeting deadlines and knowing what I needed to do, and I am very thankful to them for helping me get through it all.

In addition to those folks who helped me directly in the lab while at Berkeley, I also had two people who helped get me interested in physics while an undergrad at MIT and who gave me very good guidance and tutoring that has aided me immensely throughout my PhD. The first is Prof. Ado Jorio, who invested a lot of time into teaching me physics and basic experimentation early on, and was very supportive of me throughout my undergrad career. He taught me that there is always more to get out of the data than what meets the eye, and to always dig deep to try to find out what the little stuff is. I was very lucky to get to work with him and I greatly appreciate all the time he invested in me. The second is Prof. Mildred Dresselhaus, who was a huge inspiration for me to get into physics early on, and was a tremendous advisor for me during my undergrad career. She has always been a constant source of ideas that she is eager to share with everybody. She also always has her own way of thinking about things and tireless approach to working on problems, and she taught me the importance of those two qualities. I will always cherish the time I got to spend in her lab and the support that she has given me.

Finally, I have been blessed with tremendous friends and family who have supported me throughout my time here at Berkeley. Kenny Jensen and Caglar Girit in particular played a major role in making my PhD a lot of fun. Late night discussions about physics and the meaning of it all with them was one of the best things about working in Birge hall, and I have learned a lot of physics and useful knowledge in general from them. Many of my good times out here took place with them. Tim Anderson has been a constant source of happiness and motivation for me throughout my

time in Berkeley. Other than the things I learned in grad school, a great deal of the new things I learned out here have been through him. Jed Horne has also been a great friend of mine out here. He has gotten me involved with a lot of fun activities such as repairing buses and building warehouses and going to burning man, and I am very glad that he has been here with me throughout these past 6 years. I was also very fortunate to get to know Claire Wyart and Uzay Girit during my time out here, who both can always get me excited and energized about things, and who I shared a lot of happy experiences with. Other friends that I have made and spent a lot of quality time with in Berkeley and have really contributed to my life out here are Star Simpson, Moana Minton, Michelle Dolinski, Brendan Nee, Jim Mason, Hal Haggard, Gautum Agarwal, my roommates Greg Reft, Mike Parker, Billy and Mark Ribak, and Ki Kim.

In addition to these friends that have been with me in Berkeley, my friends from college and back home have provided a lot of support and generated a lot of good times for me out here. These include Ryan Perry, Rhett Creighton, Jacqueline Yen, Nick Ferrier, Manprit and Gurprit Brar (my cousins), Kate Ricke, Allison Stephenson, Cary Martin, Danielle Smith and Andy Lieserson. It is really great to have such a strong base of friends to talk to and to bounce ideas and misery and jokes off of.

The last two and a half years of my PhD has been a particularly happy time for me because of my girlfriend Brie Fuqua. She has provided a lot of emotional support for me and has kept me energized and excited about life.

Finally, my family, Gurdip, Dorothy and Gloria, has supported me immensely throughout graduate school and throughout my life. They got me interested into science early on, and they have kept me motivated ever since. They have always been a source of inspiration and encouragement, and knowing they are there for me allows me to aggressively pursue my goals.

During my undergrad career and during my first year at Berkeley I was very lucky to have my friend Edgar Gonzalez in my life. From him I learned a lot of new ways to communicate with people, including how to write a good e-mail and how to talk to shy people and small children. I also learned from him that there was always something funny to say or a positive way to look at things if I just try, and even if I can't figure out what it is I should act like it's right there. I miss him dearly. If anybody ever finds any part of this thesis interesting or useful in anyway, I dedicate that part to him.

1 Introduction

Since the invention of the scanning tunneling microscope (STM) by Binnig and Rohrer in 1982 [1], it has served as one of the premier surface probes for studying the atomic and electronic structure of conductive surfaces. The sub-Å spatial resolution and sub-meV energy resolution provided by a low temperature STM can be used to correlate atomic configurations with electronic structure in ways not possible with other techniques. Early STM experiments, for example, were used to definitively determine the atomic reconstruction patterns of a number of semiconductor surfaces [2-4] and provide clues to the microscopic mechanisms involved. The energy-resolved spatial mapping capabilities of the STM have been used to determine the dispersion relation of metallic surface states [5], and to probe the electronic structure of highly correlated materials such as high-T_C superconductors [6]. The successes of these types of experiments have established STM as a desirable technique to probe new materials and surfaces that have non-zero electrical conductance.

In addition to these capabilities, the STM has many other useful experimental modes. It has been shown, for example, that an STM tip can be used to manipulate the positions of atoms and molecules on conductive surfaces [7]. This capability has been exploited to build patterns that modify the electronic structure of the underlying surface [5], and to also carry out chemical reactions at the ultimate, single molecule scale by forcing atoms and molecules together [8]. In other experiments, STM's have been used to measure the high frequency components of the tunneling signal. These studies have allowed the STM to probe the Rabi precession of underlying atoms [9], and produced spatial maps of the frequency dependent impedance [10] - and therefore dielectric function - of surfaces. These new techniques have been accompanied by new theoretical understanding of the basic STM tunneling signal. Inelastic tunneling spectroscopy, for example, has been used to determine the vibrational [11] and magnetic [12] structure of several systems at the atomic scale.

This thesis describes two sets of experiments, involving spin-polarized measurements and the exploration of graphene, where STM techniques have been pushed into new experimental regimes and used to probe properties that could not have been measured otherwise. It describes both the challenges that must be overcome to perform these experiments and the additional theoretical modeling needed to properly interpret them.

1.1 Spin-Polarized STM

The first experiment described in this thesis is a spin-polarized STM (SP-STM) experiment performed on individual magnetic adatoms. SP-STM is a technique that was first developed by Roland Wiesendanger in 1990 [13]. The basic principle of SP-STM is to use a ferromagnetic electrode for the STM tip and to then tunnel into a magnetic

surface, effectively creating a scanning tunneling magneto-resistance (TMR) junction [14]. Unlike a typical TMR device, however, the STM tip is capable of forming a tunnel junction with an individual atom within - or on top of - a surface, and thus the tunneling magneto resistance is sensitive to the spin polarization state of that atom. This technique has been used extensively in the past decade – primarily by the Wiesendanger group – to image the spin of individual atoms in ferromagnetic and anti-ferromagnetic thin films, often finding a hidden complex spin structure that would not have been possible with conventional spatially averaging techniques. These studies, for example, have been able to image spin vortices within magnetic films [15] as well as spin spirals which have a periodicity of only a few atoms within a thin film [16]. The result of these atomic length scale spin measurements is that the dominant magnetic coupling mechanism for these surfaces can be determined with a high degree of certainty. In many cases the dominant mechanism is a simple ferromagnetic or antiferromagnetic coupling due to the exchange interaction [17], but in other cases more exotic magnetic interactions can be observed, such as the RKKY [18] and Dzyaloshinskii-Moriya [16] interactions. These experiments have established SP-STM as the premier probe of the local magnetic order of conductive surfaces.

In the work shown in this thesis, I will present a SP-STM study where an elemental variable is tuned while the magnetic coupling is monitored with the SP-STM tip. We first grow a ferromagnetic system with known magnetic properties that can be used to calibrate our SP-STM tip. Then, magnetic adatoms of different chemical species –Fe, Cr, and Cu – are deposited onto the ferromagnetic surface. The spin polarization state of each type of adatom is then measured relative to the underlying magnetic surface, and thus the species-dependent magnetic coupling can be ascertained. The result is that we are able to see a clear difference in the way different chemical species interact magnetically at the single atom level, and we can compare our results to theoretical models which help understand those differences.

1.2 **STM on Graphene**

While STM experiments often provide a great deal of information about the surface of conductive materials, those surface properties do not always provide a great deal of information about the bulk material properties, such as the dielectric function or overall conductivity. Furthermore, because STM is most frequently performed in UHV conditions, the surface systems that are being measured do not necessarily exist in air, and the information gained from the STM can not always be utilized in a practical fashion. In the case of graphene, however, the story is different.

Graphene is a single, atomically thin layer of graphite, with a network of carbon atoms arranged into a honeycomb lattice. When placed on an insulating surface, its intrinsic properties can be preserved, as has been confirmed by transport[19, 20] and light absorption experiments [21]. When a graphene device (i.e. graphene on an insulator contacted by an electrode) is placed inside an STM it provides a unique opportunity from the perspective of an STM experimentalist. Unlike measuring the surface properties of a bulk material, in the case of graphene the surface *is* the material. Thus, the STM has

access to the same states that contribute to the bulk conduction and optical properties of graphene, and can directly image the same landscape that the graphene quasiparticles observe. This provides a good opportunity to use the results of STM measurements of local graphene features to help interpret macroscopic measurements of graphene.

Perhaps even more important is the fact that when a graphene device is equipped with a backgate electrode, it provides the first gate-tunable surface that can be probed using STM. This gives the STM experimentalist an extra “knob” that can be turned *in situ* that can be utilized to understand the intrinsic graphene properties with great detail, but can also be used to controllably dope surface impurities on graphene, ionizing and de-ionizing them in the process. This extra feature makes graphene a surface that is likely to have widespread use in future STM experiments, especially those that seek to understand the properties of adsorbed molecules and individual atoms.

In the work shown in this thesis, I present the first STM measurements of a gate-tunable graphene surface. By utilizing this new gate-tunability, it is shown that the tunneling signal of graphene is dominated by an inelastic process, and that it also contains signatures of many-body interactions in the graphene. It is further shown that the STM can image the potential landscape of the graphene, and we reveal that this landscape is disordered, and fluctuates due to impurities trapped beneath the graphene sheet. We further use the STM to monitor the ionization of individual Co adatoms on graphene, observing a screening cloud to form and disappear depending on the ionization state of the adatoms. Most importantly, we discuss the theoretical and experimental challenges that need to be overcome to measure graphene surfaces in an STM and to properly interpret the data.

1.3 Outline of thesis

This thesis is divided into three chapters: (1) STM theory and operation, (2) Spin-Polarized STM, and (3) STM of Graphene.

In the first chapter I review the original tunneling theory developed by Bardeen as well as how it has been applied to STM by Tersoff and Hamann, and then I describe the basic experimental setup used for the STM experiments performed in the later chapters. The theoretical portion of this section is presented in explicit, step-by-step detail, which I feel is necessary to understand the subtle tunneling effects that are observed in the later two chapters, especially the graphene section.

The second chapter discusses how to perform SP-STM experiments using an Omicron LT-STM, and then describes SP-STM measurements of individual magnetic adatoms on a ferromagnetic surface. This chapter describes every step necessary to prepare and calibrate a Cr-coated, spin-polarized STM tip. I provide the explicit experimental parameters used for preparing SP-STM tips inside the Omicron UHV system, and I describe the problems one might encounter during the tip preparation process. This chapter also describes how to calibrate a SP-STM tip on a Co/Cu(111) surface, and outlines strategies used to improve the tip quality. After reviewing the tip preparation process, I describe SP-STM results obtained on different species of magnetic adatoms coupled to ferromagnetic nanoislands. This latter section closely follows a

paper I co-authored with Yossi Yayon [22], and also includes unpublished data where Cu adatoms are interrogated

The third chapter of this thesis describes STM experiments on graphene. I first review the electronic structure of graphene, deriving key results that are relevant to our STM experiments including how the STM tip can become and invasive probe when measuring graphene. I then discuss how graphene flakes were synthesized and describe how they are prepared for experiments inside the Omicron LT-STM. Details and hints concerning how to properly calibrate an STM tip prior to measuring a graphene surface are also provided. Finally, I describe a number of results obtained on gate-tunable graphene surfaces inside the STM. Each of these results correlate with previously published work that I co-authored, mostly with Yuanbo Zhang. The results presented are, (1) the observation of phonon-assisted tunneling in graphene [23], (2) many-body effect observed in the tunneling signal of graphene [24], (3) spatial inhomogeneity of the graphene electronic structure [25], and (4) the observation of gate-controlled ionization of Co adatoms on graphene [26].

2 STM theory and operation

2.1 Bardeen and Tersoff-Hamann model for tunneling

The basic formalism used to explain tunneling current flowing between two electrodes (the fundamental geometry of an STM) was developed by Bardeen in 1961 [27]. Here I give an overview of that formalism as described by Chen, Ch. 2 [28] and derive the key results using a planar tunneling model. I then show how to use the basic tunneling model to understand the specific case of tunneling from an STM tip into the 2D Bloch states of a surface - a result first derived by Tersoff and Hamann[29]. While the results shown here can already be found in existing literature, I present them again in detail because I find them necessary to understand the subtle tunneling effects described in the graphene section of this thesis.

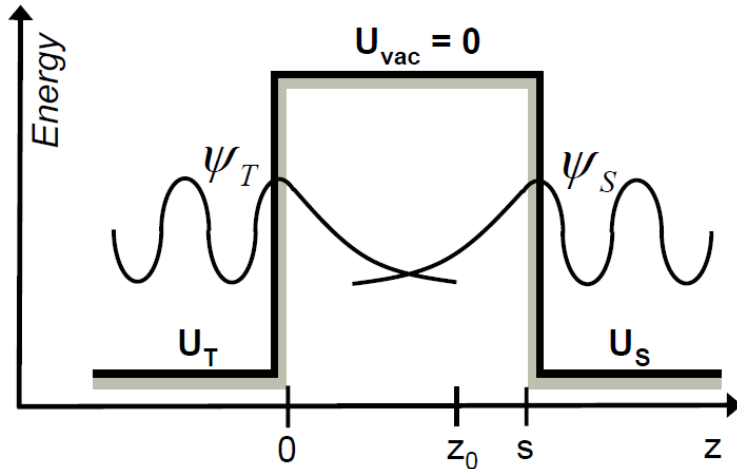


Figure 2-1 – Schematic of a planar tunnel junction between two electrodes with zero bias between them. The wavefunctions on each electrode decay into the vacuum region between them.

Figure 2-1 shows a schematic of a planar tunneling junction between two electrodes separated by a vacuum barrier, with the left and right electrodes representing the tip and sample, respectively. Each electrode has an associated potential and eigenstates that satisfy the Schrödinger equation within that electrode, e.g.,

$$i\hbar \frac{\partial \Psi}{\partial t} = \left[-\frac{\hbar^2}{2m} \frac{\partial^2}{\partial z^2} + U_s \right] \Psi \quad (1)$$

with stationary states given by:

$$\Psi = \psi_s e^{-iE_s t/\hbar} \quad (2)$$

Where E_s is an eigenvalue given by:

$$\left[-\frac{\hbar^2}{2m} \frac{\partial^2}{\partial z^2} + U_s \right] \psi_s = E_s \psi_s, \quad (3)$$

and likewise for the other electrode. Outside of each electrode the wavefunctions of these eigenstates decay into the vacuum. The first assumption of the Bardeen tunneling picture is that the sets of eigenstates on each side are assumed to be approximately orthogonal to each other, i.e.,

$$\int \psi_T^* \psi_s d^3r \sim 0 \quad (4)$$

The eigenstates on each side are, however, not solutions to the Schrödinger equation for the combined system,

$$i\hbar \frac{\partial \Psi}{\partial t} = \left[-\frac{\hbar^2}{2m} \frac{\partial^2}{\partial z^2} + U_s + U_T \right] \Psi \quad (5)$$

Hence there is some probability per unit time that an electron on one electrode will hop onto the other electrode. If we assume that the electron starts out in some eigenstate of the tip electrode, then the time evolution of the wavefunction is given by:

$$\Psi = \psi_T e^{-iE_T t/\hbar} + \sum_{S=1}^{\infty} c_S(t) \psi_S e^{-iE_S t/\hbar} \quad (6)$$

with $c_S(0) = 0$ for all T. After plugging (6) into (5) we get:

$$i\hbar \sum_{S=1}^{\infty} \frac{dc_S(t)}{dt} \psi_S e^{-iE_S t/\hbar} = U_S \psi_T e^{-iE_T t/\hbar} + U_T \sum_{S'=1}^{\infty} c_{S'}(t) \psi_{S'} e^{-iE_{S'} t/\hbar} \quad (7)$$

The second term on the right side is small because $U_T \psi_{S'}$ is small and so is $c_{S'}(t)$. After operating on the other terms with $\langle \psi_S |$ we get:

$$i\hbar \frac{dc_S(t)}{dt} = \int_{z>z_0} \psi_T U_S \psi_S^* d^3r e^{-i(E_T - E_S)t/\hbar} \quad (8)$$

If we define the tunneling matrix element as:

$$M_{TS} = \int_{z>z_0} \psi_T U_S \psi_S^* d^3r \quad (9)$$

then after an integration over time, we obtain that the probability of tunneling from the S -th state of the sample to the T -th state of the tip, is given by:

$$p_{TS}(t) = |c_S(t)|^2 = |M_{TS}|^2 \frac{4 \sin^2[(E_T - E_S)t / 2\hbar]}{(E_T - E_S)^2} \quad (10)$$

We now make the second assumption of the Bardeen tunneling formalism. We assume that the tunneling is **elastic**, such that the energy of the electron while on the tip, E_T , is the same as its energy after hopping to the sample, E_S . We also sum over all the possible states on the sample that have the energy E_S to obtain the total probability of tunneling from the tip to the sample in a time t :

$$p_{TS}(t) = \frac{2\pi}{\hbar} |M_{TS}|^2 \rho_S(E_S) t \quad (11)$$

Note that this is the same result we would have obtained by applying Fermi's golden rule, using U_S as the perturbing potential that scatters a state, ψ_T , from the tip into the continuum of states on the sample with the same energy.

2.1.1 Tunneling matrix element - s-wave tunneling

We now focus on the tunneling matrix element in Eq. (9). By using (3) we can rewrite (9) as:

$$M_{TS} = \int_{z>z_0} \psi_T \left(\frac{\hbar^2}{2m} \frac{\partial^2}{\partial z^2} + E_S \right) \psi_S^* d^3r \quad (12)$$

If we then remember that we have assumed elastic tunneling, $E_S = E_T$, this can be rewritten as:

$$M_{TS} = \int_{z>z_0} \left(\psi_S^* E_T \psi_T + \psi_T \frac{\hbar^2}{2m} \frac{\partial^2 \psi_S^*}{\partial z^2} \right) d^3r \quad (13)$$

By recalling that U_T is zero for $z > z_0$, this becomes:

$$M_{TS} = -\frac{\hbar^2}{2m} \int_{z>z_0} \left(\psi_S^* \frac{\partial^2 \psi_T}{\partial z^2} - \psi_T \frac{\partial^2 \psi_S^*}{\partial z^2} \right) d^3r \quad (14)$$

This can be rewritten as a two-dimensional integral as:

$$M_{TS} = -\frac{\hbar^2}{2m} \int_{z=z_0} \left(\psi_S^* \frac{\partial \psi_T}{\partial z} - \psi_T \frac{\partial \psi_S^*}{\partial z} \right) dx dy \quad (15)$$

This is Bardeen's tunneling matrix element. It is an integral in the 2D plane between the two electrodes. Note that it should not depend on where the plane of integration is, so long as it is between the two electrodes (i.e. the plane can be right near the tip or the sample). This follows from the elastic tunneling assumption that was made earlier and it is easy to see this by assuming that both the tip and sample eigenstates decay into the vacuum at a rate determined by their energy, i.e. $\psi_T \sim e^{-E_T z}$ and $\psi_S \sim e^{-E_S(s-z)}$. Plugging these two functions into (15) produces a result that will depend on where the plane of integration is, unless $E_S = E_T$.

Thus far we have assumed a simple planar tunneling geometry. In the general three-dimensional case of tunneling between two non-planar surfaces, a similar argument can be used to show that:

$$M_{TS} = \frac{\hbar^2}{2m} \int_{\Sigma} (\psi_T \nabla \psi_S^* - \psi_S^* \nabla \psi_T) \cdot dS \quad (16)$$

where the integration takes place on any surface, Σ , separating the tip from the sample.

If we now assume that the tip has a spherical apex (possibly a single atom), then we can make the approximation that the tip wavefunction can be taken as a spherical s-wave:

$$\psi_T \sim \frac{e^{-\kappa|r-r_0|}}{4\pi|r-r_0|} \quad (17)$$

where r_0 is the center of the sphere that defines the apex. Note that this function has the property that:

$$(\nabla^2 - \kappa^2)\psi_T = -\delta(r - r_0) \quad (18)$$

If we plug (17) into (16) and use the divergence theorem, we obtain:

$$M_{TS} = \frac{\hbar^2}{2m} \int_{\Omega_T} (\psi_T \nabla^2 \psi_S^* - \psi_S^* \nabla^2 \psi_T) \cdot d\tau \quad (19)$$

We have converted the surface integral into a volume integral on the tip side whose boundaries go to ∞ . We now use (18) and assume that the sample wavefunction decays at the same rate as the tip (as was explained above), such that $\nabla^2 \psi_S = \kappa^2 \psi_S$. This simplifies (19) to:

$$M_{TS} \sim \psi_S(r_0) \quad (20)$$

This is a critical result. It shows that, for a spherical s-wave tip, the tunneling matrix element is proportional to the value of the tunneling wavefunction evaluated at the apex of the tip. Thus, states on the surface that decay further into the vacuum will contribute more to the tunneling current. This result was first obtained by Tersoff and Hamann [29]. It is interesting to point out that if the tunneling occurs from a p-wave tip state, then the tunneling matrix element is proportional to the first z-derivative of the surface state evaluated at the tip, and for a d-wave tip state it depends on the second derivative of the surface state at the tip [28].

2.1.2 Tunnel current and conductance (dI/dV)

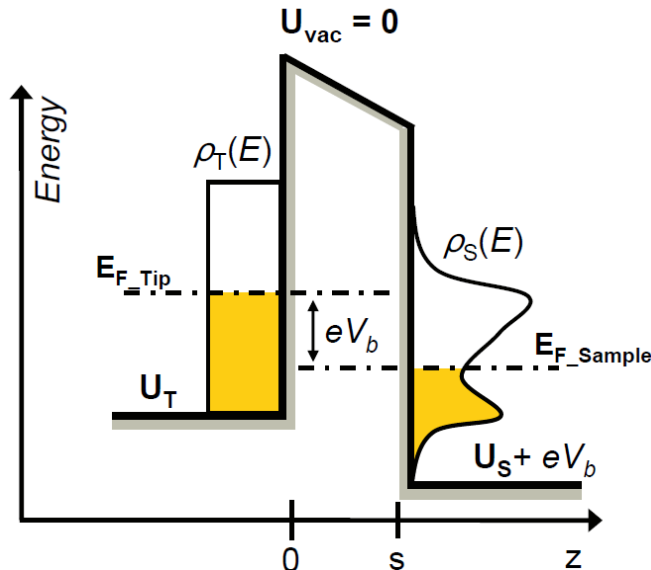


Figure 2-2 – Schematic showing a tunnel junction with a bias, V_b , applied between a sample with a complicated DOS(E) and a tip with a flat DOS(E).

Eq.(11) shows that the tunneling rate from a particular state on the tip to the surface is proportional to a tunneling matrix element as well as the density of states of the surface with the same energy. To obtain the total tunneling rate at that particular energy, we also need to multiply by the density of states on the tip at that energy, $\rho_T(E_S = E_T)$. This gives the total elastic tunneling rate at a particular energy, ε , as:

$$p_\varepsilon(t) = \frac{2\pi}{\hbar} |M_{TS}|^2 \rho_S(\varepsilon) \rho_T(\varepsilon) t \quad (21)$$

In order for an electron on the tip to actually hop onto the sample, however, it is necessary that the tip state is occupied and the sample state is unoccupied. At T = 0K, this occurs only when some bias is applied between the sample and tip, as shown in Figure 2-2. Here a bias, V_b , has been applied to the sample, so that the Fermi levels of the tip and sample are no longer aligned. Now there is a range of energies from E_{F_Tip} to $E_{F_Tip} - eV_b$ where electrons from the tip can elastically tunnel across the barrier into unoccupied sample states, at rates given by Eq. (21). If we integrate over all these possible states multiplied by their tunneling rates, we obtain the total tunneling current for a given V_b :

$$I = \frac{4\pi e}{\hbar} \int_0^{eV_b} \rho_T(E_F - eV_b + \varepsilon) \rho_S(E_F + \varepsilon) |M_\varepsilon|^2 d\varepsilon \quad (22)$$

Typically, the tunneling matrix element can be assumed to be energy independent over small energy ranges (~10% difference over 200meV) and so can be taken out of the integral. If we also assume that the tip has a flat density of states, as shown in Figure 2-2, then $\rho_T(E_F - eV_b + \varepsilon) = \rho_T$ for all ε and that can also be taken out of the integral. Then by taking the derivative of (22) with respect to V_b , (and setting $E_F = 0$) we obtain:

$$\frac{dI}{dV_b} = \frac{4\pi e^2}{\hbar} |M_0|^2 \rho_T \rho_S(V_b) \quad (23)$$

This is an important result which shows that the tunneling conductance is proportional to the density of states of the sample. Hence, by measuring the tunneling current as a function of applied bias, the electronic density of states in the sample can be extracted. Note that this requires the STM tip to have a flat, constant density of states, which is typically achieved by poking and pulsing the STM tip into a surface until it is free of spectroscopic anomalies.

2.1.3 Tunneling into 2D Bloch states

Eq. (20) shows that the tunneling matrix element is dependent on the decay rate of the sample state into the vacuum. In most cases the decay rate for a state of energy ϵ into the vacuum is given by:

$$e^{-\frac{\sqrt{2m(\bar{\Phi}-\epsilon)}}{\hbar}z} \sim e^{-\frac{\sqrt{2m(\bar{\Phi})}}{\hbar}z} \quad (24)$$

where $\bar{\Phi}$ is the average value of the work functions of the tip and sample ($\sim 4\text{-}6$ eV) and the approximation works for small ϵ (a few 100meV). In the case of a Bloch wavefunction of a crystal, a momentum dependent correction needs to be made, as was first shown by Tersoff and Hamann [29]. To see this, we begin by writing the 2D Bloch wavefunction of the surface with in-plane wavevector $\vec{k}_{||}$ as:

$$\psi_{\vec{k}_{||}} = \sum_{\vec{R}} f(\vec{r} - \vec{R}) e^{i\vec{k}_{||} \cdot \vec{R}} \quad (25)$$

where $f(\vec{r} - \vec{R})$ is, for example, the on-site atomic wavefunction. We can approximate this function as an s-wave centered on the atom, and rewrite (25) as:

$$\psi_{\vec{k}_{||}} = \sum_{\vec{R}} \frac{e^{-\lambda(\vec{r}-\vec{R})}}{\lambda |\vec{r} - \vec{R}|} e^{i\vec{k}_{||} \cdot \vec{R}} \quad (26)$$

If we Fourier expand the s-wave and re-organize terms this becomes:

$$\begin{aligned} \psi_{\vec{k}_{||}} &= \sum_{\vec{R}} e^{i\vec{k}_{||} \cdot \vec{R}} \int d^2 q \cdot b(\vec{q}) \exp[-(\lambda^2 + q^2)^{1/2} |z|] \exp[iq \cdot (\vec{x} - \vec{R})] \\ &= \int d^2 q \cdot b(\vec{q}) \exp[-(\lambda^2 + q^2)^{1/2} |z|] \cdot e^{iq \cdot \vec{x}} \sum_{\vec{R}} e^{i(\vec{k}_{||} - \vec{q}) \cdot \vec{R}} \end{aligned} \quad (27)$$

From this we can use the identity that $\sum_{\vec{R}} e^{i(\vec{k}_{||} - \vec{q}) \cdot \vec{R}} = \sum_{\vec{G}} \delta(\vec{k}_{||} - \vec{q} + \vec{G})$ to rewrite (27) as:

$$\psi_{\vec{k}_{||}} = \sum_{\vec{G}} b(\vec{k}_{||} + \vec{G}) \exp[-(\lambda^2 + k_{||}^2 + G^2)^{1/2} |z|] e^{i(\vec{k}_{||} + \vec{G}) \cdot \vec{x}} \quad (28)$$

Here \vec{G} are the reciprocal lattice vectors. If we take only the largest, $G = 0$ term we get:

$$\psi_{\vec{k}_\parallel} \sim \exp[-(\lambda^2 + k_\parallel^2)^{1/2} |z|] e^{i\vec{k}_\parallel \cdot \vec{x}} \quad (29)$$

By placing this result in Schrödinger's equation, $\left(-\frac{\hbar^2}{2m} \nabla^2 + \Phi \right) \psi = \varepsilon \psi$, it is easy to show that $\lambda^2 = \frac{\sqrt{2m\Phi}}{\hbar}$ as in Eq. (24). Equation (29) is different than (24) because of the k_\parallel^2 term. It shows that states with large k-vector decay much faster into the vacuum than states with zero k-vector, even if they have the same energy. Using (29) to define the wavefunction in (20) and considering the equation for tunneling current (22) we obtain:

$$I \sim \exp[-2(\lambda^2 + k_\parallel^2)^{1/2} |z|] \quad (30)$$

This shows that Bloch states with a large in-plane k-vector contribute less to the tunneling current than states with $k=0$, with the difference being a factor that is exponentially dependent on tip height. While this effect is not important in most cases, it will be shown later that for graphene it plays a critical role.

2.2 STM Basics

Figure 2-3 shows the basic setup of an STM experiment. A sharp metallic tip – which is typically an electrochemically etched PtIr or W wire – is mounted onto a piezoelectric transducer. The tip is then brought close to a conductive sample using some coarse motion scheme – piezoelectric motors (not shown in Figure 2-3) were used for the experiments described here. A bias, V_b , is then applied between the sample and the tip, and the tip is slowly brought closer to the sample by applying a voltage across the z-axis of the piezoelectric transducer. The current flowing through the tip, I , is continuously monitored, and once it reaches a certain setpoint value (typically a fraction of a nA) the tip is held at a constant height above the surface. The absolute value of the tip height is never known for sure, but it is typically estimated to be $\sim 5\text{\AA}$ above the surface for a current of a fraction of a nA.

Topographic imaging of the surface is then conducted by raster scanning the STM tip back and forth across the surface via application of x and y-axis biases to the piezoelectric transducer. The voltage on the tip is typically held constant and the current is continuously monitored. As shown in Eq. (30) above, the current has a strong exponential dependence on the distance from the tip to the surface, and this dependence allows for a feedback circuit to detect minute changes in the tip height and apply a

corrected z-bias to the transducer to bring the STM tip back to the correct height. An example topographic image is obtained of the underlying surface, as is shown in Figure 2-3 and Figure 2-4A. These images show that the STM can detect sub-Å height changes in the surface, thus revealing the topographic structure produced by single atoms. (Note that these and other images in this thesis were plotted using the WSxM software [30].)

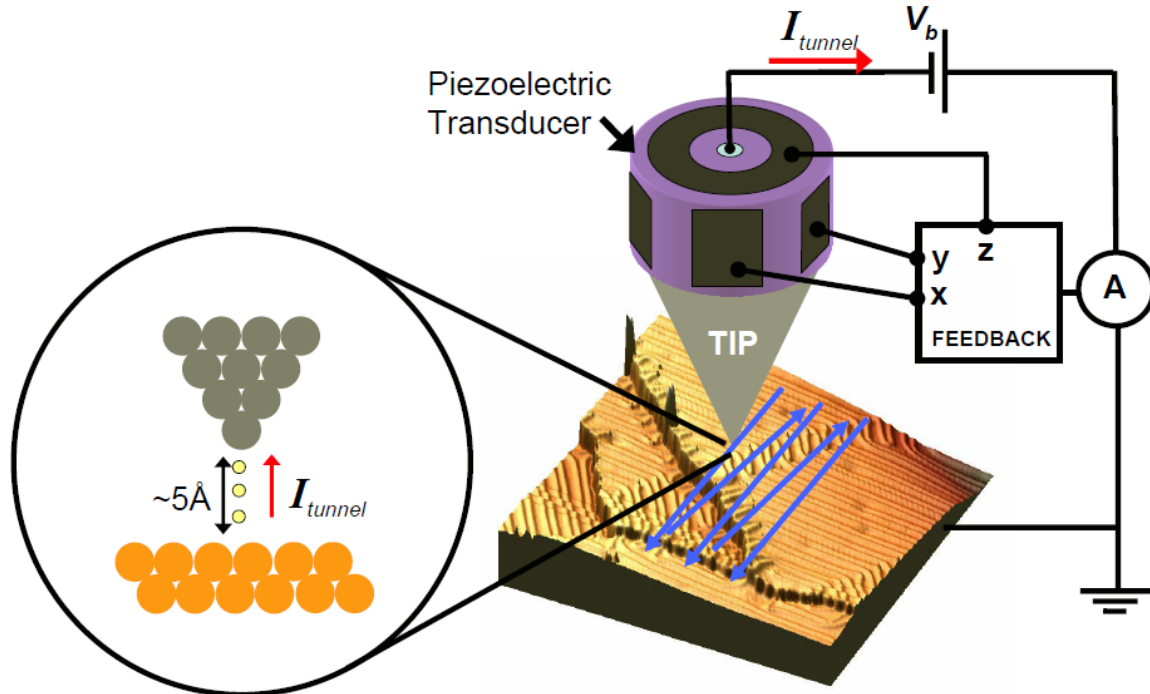


Figure 2-3 – Cartoon of an STM tip scanning an Au(111) surface. The Au(111) surface is revealed to have a “herringbone” reconstruction pattern as well as atomic step edges.

In another mode of operation, the STM tip is held fixed over a certain area of the surface, and the feedback is turned off. The tunneling bias is then varied over some range while the current is monitored. The resulting I-V curve typically contains information about the energy dependent density of states [DOS(E)] of both the tip and the sample, as was described by Eq. (22). Usually, the experimentalist is most interested about the DOS(E) of the sample, so an STM tip with a flat DOS(E) is used and the resulting derivative of the I-V curve gives the DOS(E) of the sample, as described by Eq. (23). In most cases, it is desirable to measure the dI/dV signal by use of a lock-in amplifier. Here, a small “wiggle voltage” is applied to the STM tip, usually with a magnitude of $V_{rms} = 1\text{-}5\text{mV}$ and frequency of 200-600Hz. The dI/dV signal is then obtained by lock-in detection of the resulting ac tunneling current. This technique typically produces a signal that is less noisy than would be produced by simply taking a derivative of the I-V curve. It is important, due to piezo-drift and thermal drift of the STM tip in the z-direction, to not turn off the feedback too long when performing dI/dV measurements. For the Omicron LT-STM used in all the work presented here, the feedback could typically be turned off for ~2-3 minutes without adverse effects.

The spatial imaging and DOS(E) sensitivity of the STM can be combined in the form of “dI/dV mapping” of surfaces. Here, the DOS(eV_b) is measured at a particular

bias as the feedback is left on and the STM tip is raster scanned across the surface. This produces a spatial map of the DOS at eV_b , allowing the experimenter to see how the electronic density of states changes across the surface at that particular energy. Often this technique can be used to show that parts of the surface that look similar topographically actually contain different electronic structures. Figure 2-4 provides a good example of this. Here, Co adatoms on a Pt(111) surface are imaged topographically at a certain bias while, simultaneously, a dI/dV map is obtained. As can be seen in these images, the adatoms all look the same in the topographic image, Figure 2-4A, but the dI/dV map, Figure 2-4B, reveals that the adatoms actually contain two different electronic structures. In this case, the different electronic structure is related to how the Co adatom sits on the underlying Pt(111) surface [31].

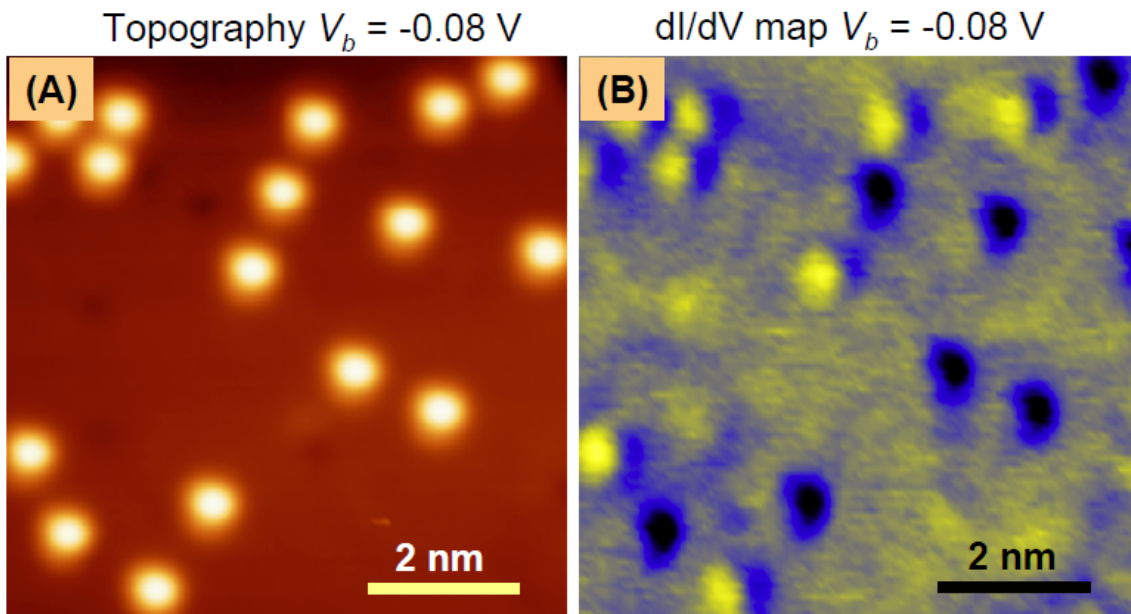


Figure 2-4 – A topographic image (A) and dI/dV map (B) of Co adatoms on a Pt(111) surface. These two images were obtained simultaneously using $V_b = -0.08\text{V}$ and $I = 0.1\text{nA}$.

All the experiments presented on this thesis were performed in an Omicron LT-STM at 4.8K. The STM stage in this machine is hung on springs inside a liquid helium cryostat with a liquid nitrogen shield, which helped reduce vibrational noise. Stable tunneling can be achieved in this system with currents as low as 2pA, and the spectroscopic energy resolution was typically dictated by the V_{rms} applied to the lock-in amplifier.

2.3 UHV

In order to obtain clean surfaces and stable STM tunneling conditions, all experiments here were performed under UHV conditions. Figure 2-5 shows a schematic of the UHV chambers for the Omicron LT-STM system. UHV conditions were achieved by pumping with a turbo molecular pump (TMP) mounted on the preparation chamber and two ion pumps mounted below the STM chamber and the preparation chamber.

While performing STM experiments, the TMP is turned off to reduce vibrational noise. Titanium sublimation pumps are mounted inside each chamber, and turned on at weekly increments to remove impurities that do not get pumped efficiently by the ion pumps. To obtain good UHV conditions, an insulating tent was built around the machine and it was internally heated to 150 °C for two days while being pumped on with the TMP. After cooling, pressures of $\sim 2 \times 10^{-11}$ torr are considered good.

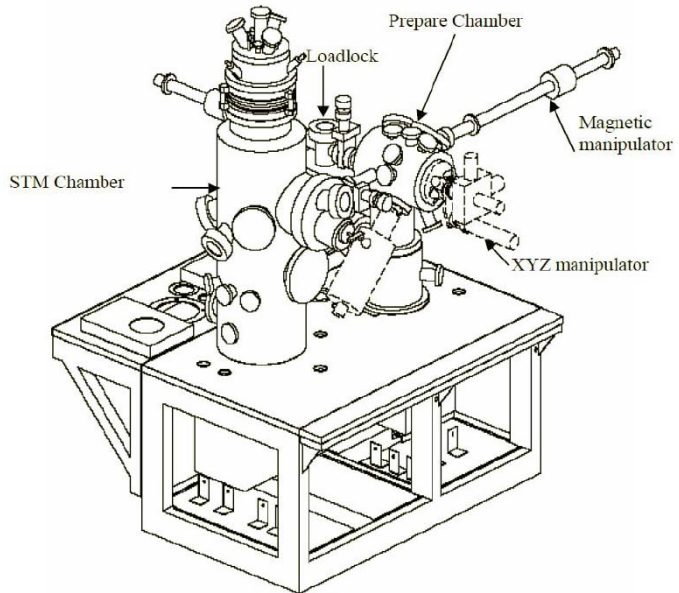


Figure 2-5 – The UHV chambers of the Omicron LT-STM.

3 Spin-Polarized STM

3.1 Motivation

Traditionally, magnetization measurements on materials have been restricted to spatially averaged techniques, such Kerr rotation microscopy, x-ray magnetic circular dichroism (XMCD), or measurement of macroscopic magnetization curves. While such techniques can often give very precise measurements of the bulk properties of materials, a complete understanding of magnetic and spin related phenomena requires probes that can measure spin and magnetization at smaller length scales. Developing such techniques has grown in importance in recent years due to the shrinking size of magnetic bits used in conventional hard drives and magnetic field sensors, as well as interest in using individual spins as quantum bits in a quantum computer [32]. Understanding magnetic order at the atomic scale is also critical to understanding behavior of many new exotic materials, such as high-T_c superconductors, ferroelectrics and magnetic semiconductors. In response, a range of new techniques have been developed to help understand magnetic properties of materials at the nm and sub-nm lengthscale. Among these methods are magnetic force microscopy (MFM) [33], magnetic resonance force microscopy (MRFM) [34], exchange force microscopy [35], and spin-polarized scanning tunneling spectroscopy (SP-STM) [13, 36]. In this section I describe the details of performing SP-STM, which can measure atomic scale spin information of a wide range of conducting magnetic surfaces, and can also provide the energy-dependent spin information of a material, giving information about the majority and minority bands.

3.2 SP-STM Fundamentals

Early spin-polarized tunneling (or tunneling magneto-resistance, TMR) measurements were first performed by Tedrow and Meservey on ferromagnet-oxide-superconducting junctions [37] and later by Julliere on ferromagnet-oxide-ferromagnet junctions [14]. Since these original experiments, much work has been done to scale down the lengthscale of TMR devices. SP-STM is essentially a scanning TMR device that can probe the spin down to the lengthscale of individual atoms. SP-STM was pioneered by the group of Roland Wiesendanger at the University of Hamburg, and since the initial demonstration, that group has used SP-STM to probe spin vortices [15], anti-ferromagnetic surfaces [17], and exotic spin states found in magnetic thin films [38]. Because SP-STM represents the smallest possible lengthscale for a TMR device, the physics can be explained in a similar manner to TMR devices.

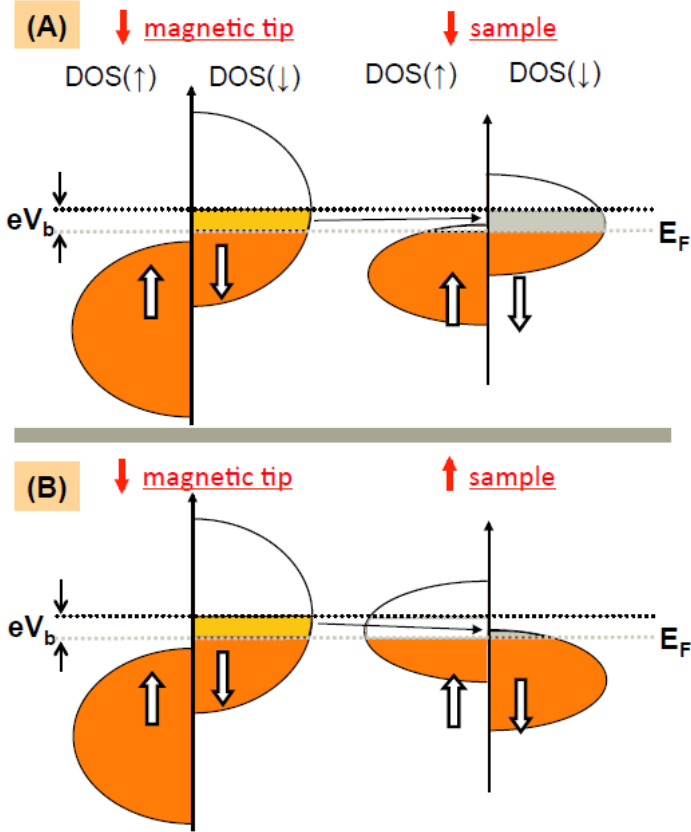


Figure 3-1 - Spin-polarized tunneling between a magnetic tip and sample oriented in the same (A) and opposite (B) directions.

The basics of spin-polarized tunneling between two magnetic materials is shown in Figure 3-1. Here I show the two different configurations for tunneling into a magnetic surface from a magnetic tip with a fixed spin. Note that for the tip and the sample shown here it is the *minority* bands that make up most of the states near the Fermi energy, and thus, at low tunneling bias, it is the minority carriers that determine the spin polarization of the tunneling current. For this reason, we describe the spin of the tip or sample to point in the direction of the minority carrier. In the case shown in Figure 3-1, the tip contains no \uparrow (majority) carriers at the Fermi energy and hence, up to a certain applied voltage, the current from the tip is spin \downarrow . The sample, on the other hand, contains a small number of majority carriers at the Fermi energy. When a bias (V_b) is applied between the sample and tip, \downarrow carriers from the tip can tunnel elastically into \downarrow carriers of the surface, and likewise for \uparrow carriers. Thus, if the both the tip and sample have spin \downarrow , as in Figure 3-1A, the \downarrow carriers from the tip have many available states in the sample to tunnel into. However, if the tip is spin \downarrow and the sample is spin \uparrow , then the \downarrow carriers from the tip have only a small number of possible \downarrow states in the sample to tunnel into. This leads to a decrease in the tunneling current for the latter scenario.

The effect of spin polarized tunneling from an STM tip is that when the STM tip is moved on top of a magnetic structure whose spin is oriented in the same direction as the SP-STM tip, there is an increase in the conductivity, and vice versa for an oppositely oriented surface. This change in conductivity can be seen as an apparent change in topographic height of some feature on the surface, as was done originally in Ref. [13].

Alternatively, by probing the dI/dV signal of the two oppositely oriented features, the changes in conductivity can be directly compared as a function of tunneling bias. This relationship can be understood by modifying Eq. (23) in Section 2.1.2 to include spin as follows:

$$\frac{dI}{dV}(V_b) \propto \sum_{\sigma=\uparrow,\downarrow} LDOS_{tip}(E_F, \sigma) \cdot LDOS_{sample}(eV_b, \sigma) \quad (1)$$

If we assume, as in Figure 3-1, that $LDOS_{tip}(E_F, \uparrow) = 0$ and that, for a \downarrow sample $LDOS_{sample}(eV_b, \downarrow) \gg LDOS_{sample}(eV_b, \uparrow)$, then this equation shows that the dI/dV signal will be enhanced when a \downarrow tip probes the dI/dV signal at V_b of a \downarrow sample, as compared to a \uparrow sample. If one were to then measure a sample that contains regions with spins oriented \uparrow and \downarrow , as shown in Figure 3-2, then if the $dI/dV(V_b)$ signal were measured as a function of position, the \downarrow regions will appear “higher” than the \uparrow regions. It is this concept that allows SP-STM to map, with Å-scale resolution, the orientation of the spins of a material.

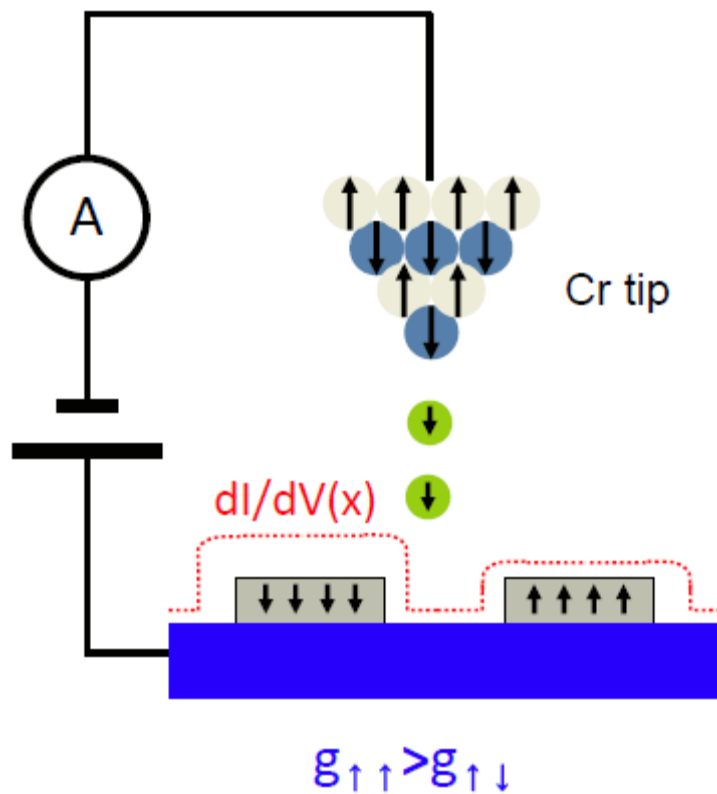


Figure 3-2 – Schematic showing position-dependent spin-polarized tunneling between SP-STM tip and magnetic sample.

3.3 Preparation of SP-STM Tip

The essential phase of performing SP-STM is to somehow obtain a STM tip with a fixed spin at the end. Initially, this was achieved by using bulk magnetic materials, such as CrO₂ as the tip material [13]. This technique, however, has problems with consistency due to the exposure of the often reactive material to air, and, also, such tips often produce large stray fields that could influence the magnetic surface being probed. Another method of obtaining spin-polarized STM tips include poking a standard tungsten STM tip into a magnetic surface and picking up a small magnetic cluster on the end [39], or even picking an individual magnetic atom from the surface [40]. Typically, however, most SP-STM tips are obtained by epitaxial growth of a thin magnetic crystal on the surface of an electrochemically etched W tip [36, 41]. Such tips generally have a low stray field, and behave in a consistent manner spectroscopically. An additional advantage is that, for STM equipped with a large magnetic field, the spin direction of such tips can be flipped due to the soft magnetic properties of a thin magnetic film.

The type of tip used in my experiments was obtained by growing a thin (~40 monolayer) Cr film epitaxially on an annealed W tip. This type of tip was first developed by the Wiesendanger group [17]. The advantage of these tips is that, due to the anti-ferromagnetic ordering of the Cr layer, the tip has very low stray field, with the tunneling occurring from a single Cr atom with a fixed spin polarization, as shown in Figure 3-2. An additional advantage of these tips is that you can choose whether to have an in-plane or out-of-plane spin polarization by controlling the thickness of the Cr film. Typically, 30-50 mL leads to an out-of-plane spin, while ~120 mL leads to an in-plane spin [17]. For the experiments shown here, the measurements were performed with tips that had an out-of-plane spin polarization. Typically, the preparation procedure for these tips involve three main steps: (1) etching and annealing a W-tip, (2) evaporating a Cr film onto the W-tip and (3) calibrating the SP-STM tip on a magnetic sample. Below I describe these three steps in detail.

3.3.1 Etching and annealing W tip

In order to obtain a clean and sturdy W tip to grow our Cr film on, we first electrochemically etch a polycrystalline W wire (0.375 mm; 99.95% purity; *Alfa Asear*) using a meniscus method. The basic setup is shown in Figure 3-3A. A cathode metal sheet is bent into cylinder and placed inside a 20ml beaker. An NaOH solution of 5.0N concentration is poured into the beaker until it is level with the top of the cathode cylinder. The W wire is lowered into the beaker until it touches the surface of the solution, and then it is lowered 1mm further. A computer controlled voltage supply is used to apply 3.8 V to the tip, and the current is monitored with a current meter hooked up to the computer. Initially, the current is typically 30mA, and it slowly drops as the tip is etched and less W surface area is exposed. After the current gets to below 8mA, the computer looks for a sudden change of more than 10% in the current, which indicates that the lower portion of the wire has fallen from the upper portion, forming an apex. When this condition is met, the computer immediately shuts off the applied voltage. Once the

tip is removed it is washed in distilled water. Typical SEM images of a W tip etched this way are shown in Figure 3-3B,C. For a good tip, a 50 nm radius of curvature can be achieved.

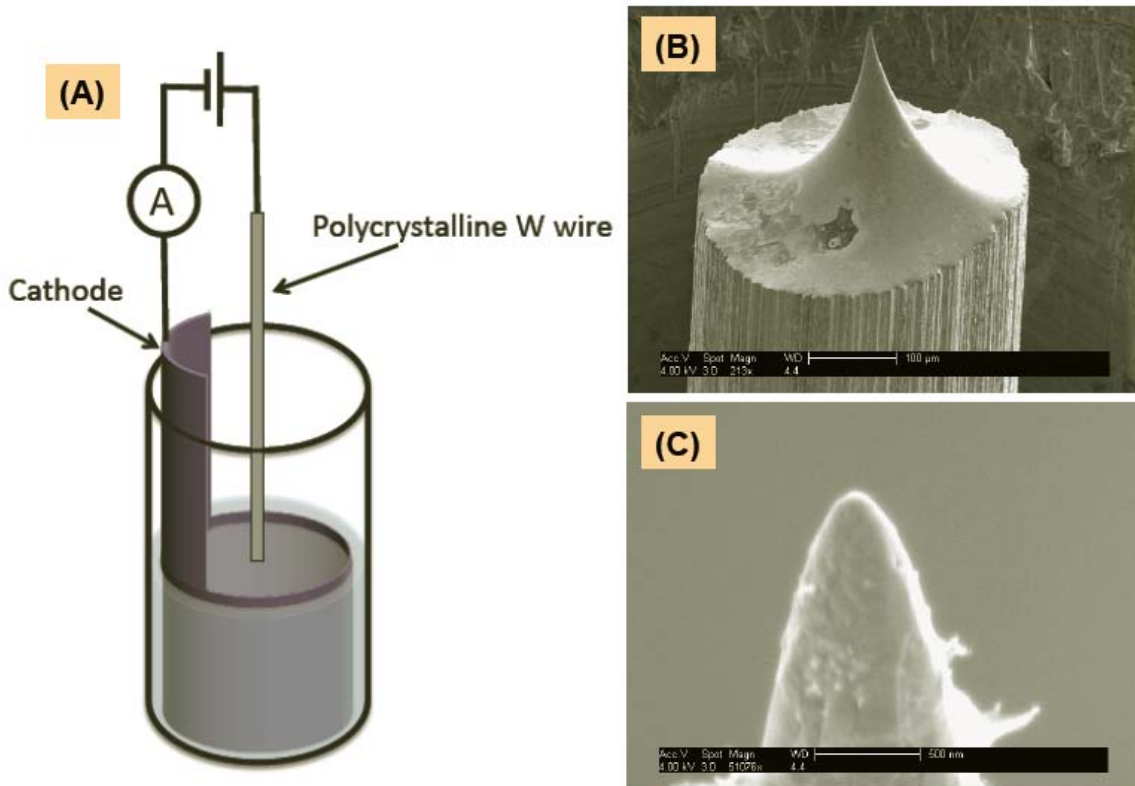


Figure 3-3 – (A) Schematic showing electrochemical etching setup for W-tip using NaOH (5.0 N). **(B,C)** SEM images of freshly etched W tip using this method. Scale bars are 100 μm for (B) and 500 nm for (C).

After the tip has been etched, it is mounted in an Omicron tip holder and transferred to the loadlock of the preparation chamber. After pumping on the loadlock for ~2 hrs the tip is transferred into the preparation chamber, and custom manipulators are used move the tip from the Omicron tip carrier to a custom wire holder mounted on a standard Omicron sample plate, which is placed onto the xyz manipulator of the preparation chamber. The tip is then positioned in front of the sputter gun and sputtered at 500V, 10-20 μA for 30min. This sputtering procedure should always be performed prior to the annealing procedure, for both newly etched tips being introduced to the vacuum, and for previously prepared SP-STM tips that are being reused.

The tip is then manipulated so that it is brought close to an enclosed hairpin filament (Kimball Physics, part # ES-020) that has been mounted vertically down from the top of the preparation chamber (like a stalactite), as shown in Figure 3-4A. This filament rests inside a grounded tantalum shield with a 2-3mm aperture centered on the end of the hairpin filament. This shield and the hairpin-shape of the filament are to ensure that only the very apex of the STM tip is heated, with the bulk of the electron emission coming from the part of the filament closest to the STM tip, and with the shield blocking much of the would-be emission current destined for the sides of the tip. This is

necessary because the annealing procedure needs to actually melt the polycrystalline W STM tip so that clean crystalline domains are formed for the Cr layer to grow off of. Without these precautions, it is easy to melt the entire W wire. Typically, the apex of the filament is recessed 1 mm from the center of the shield aperture. The xyz-manipulator is used to position the tip in the center of the shield aperture, and +2 kV is applied between the tip and the grounded filament. A computer program is used to apply 2 second pulse of current through the filament while monitoring the pressure in the prep chamber and the emission current hitting the STM tip. A camera is positioned so that the operator can watch the tip anneal while the filament is on. The annealing procedure is done slowly, with the operator increasing the current through the filament a little higher with each pulse applied to the tip. The goal is the heat the tip white hot, typically with it glowing for a couple seconds after the filament is turned off. For the filaments used in this experiment, the starting current was usually 2.0 Amps, which typically produced no emission current, and it is increased slowly (in 0.01 amp increments once you start to see emission current) while making sure that the pressure does not increase about 1×10^8 torr during the current pulse. A high pressure spike will cause a high voltage arc between the tip and filament, which will immediately melt the tip. Typically, the tip will begin to glow white hot when the emission current reaches 4 - 5 mA, which for our filaments and geometry, required 2.6 amps applied through the filament.

Figure 3-4B,C show SEM images of a electrochemically etched W tip after the annealing procedure. Typically, W crystalline domains can be seen on the tip, and the apex is more rounded, clean and smoother than before the annealing.

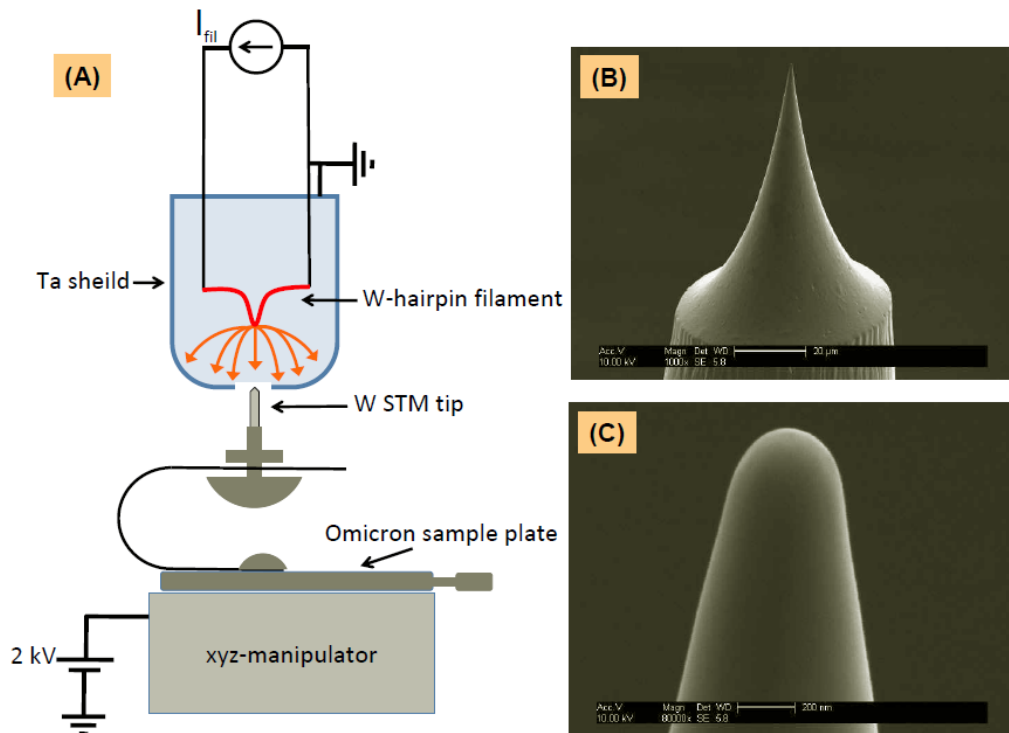


Figure 3-4 – (A) Schematic showing annealing procedure for W tip. **(B,C)** SEM images of annealed W tip (after passing through air). Scale bars are 20μm (B) and 200nm (C).

3.3.2 Cr film growth on annealed tip

The next step is grow a Cr layer on the apex of the annealed W tip. This step requires a Cr evaporator that has been calibrated to evaporate ~1mL per minute. This calibration must be done before the tip is brought into the preparation chamber and annealed. The Cr evaporator is an e-beam evaporator with a filament placed close to a molybdenum crucible containing high purity Cr chunks (note: Cr rods, although high purity, contained trapped gases that lead to dirty film growth). In order to calibrate the evaporator, Cr is evaporated onto a clean Au(111) surface at room temperature, as shown in Figure 3-5. For our evaporators, 1 mL per minute Cr evaporation typically occurs at 19.0 mA emission current @ 2kV. This calibration typically has to be repeated after 4 SP-STM tips have been prepared.

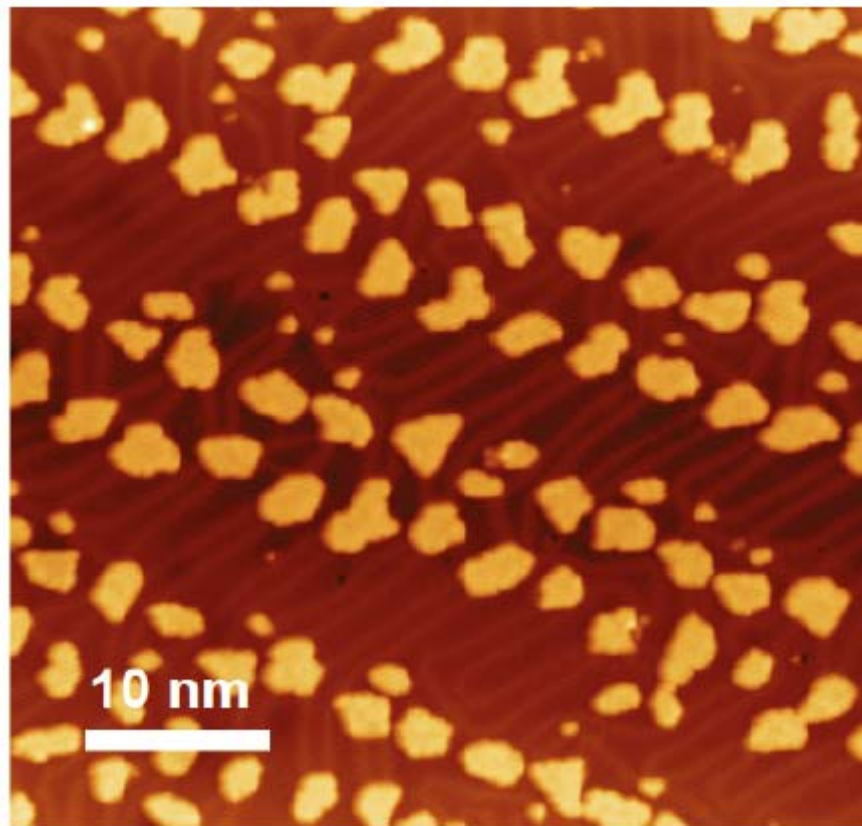


Figure 3-5 – STM topograph after of Au(111) surface after 20 sec Cr deposition to calibrate Cr evaporator. Coverage here represents a deposition rate of 0.7 mL/min.

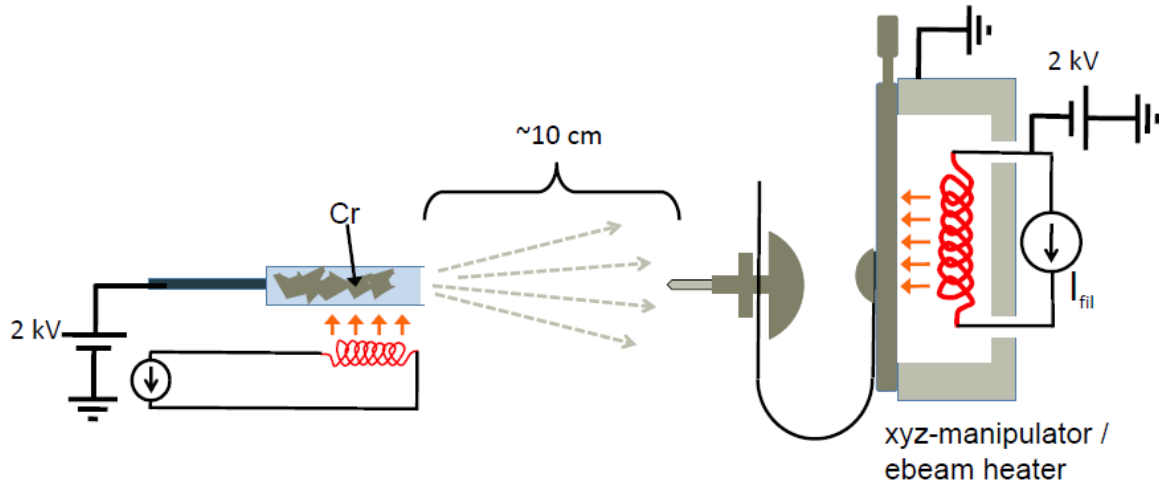


Figure 3-6 – Schematic showing Cr evaporation procedure onto annealing W tip.

After the W tip has been annealed, it is placed on the e-beam heater on the xyz-manipulator and is pointed directly at the Cr evaporator at the same distance the Au(111) was when the evaporator was calibrated ($\sim 10\text{cm}$), as shown in Figure 3-6. The tip is then heated to 220°C and – with the evaporator shutter CLOSED – the evaporator is brought to the evaporation condition for $\sim 1\text{ mL}$ of Cr per minute. The shutter is left closed for 5 min so that the evaporator can outgas. The shutter is opened after this outgassing phase, and the evaporation should occur for $\sim 40\text{ min}$, or enough time to grow between $40\text{-}50\text{ mL}$ of Cr on the STM tip. After the evaporation has finished the tip is quickly transferred to the STM chamber and moved to the piezo tube inside the cryostat. Figure 3-7A shows an SEM image of a Cr coated W tip that has been transferred through air after the evaporation procedure; Figure 3-7B shows a cartoon of the expected configuration of the tip. Note that for a Cr coated tip, it is expected that the electronic states near the Fermi level are composed primarily of *minority carriers* [42].

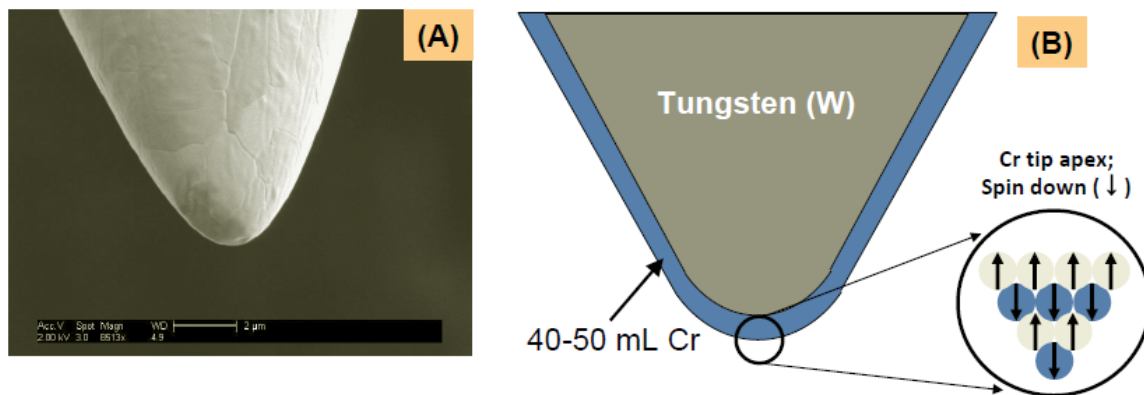


Figure 3-7 – (A) SEM image showing W tip after 40-50 mL of Cr has been evaporated onto it. Scale bar = 2um. (B) Schematic showing expected SP-STM tip configuration after Cr coverage.

3.3.3 Checking for spin polarization

3.3.3.1 Co islands on Cu(111) – non SP characterization

After transferring the SP-STM tip to the UHV chamber, a magnetic sample needs to be prepared. For our work we used 2 monolayer high triangular Co islands grown on a Cu(111) surface. These islands are known to have an out-of-plane spin polarization, and they have been well characterized magnetically and structurally by the Wiesendanger group and others [43-45]. In order to grow these islands, a Cu(111) crystal is sputtered (500 V, 5-10uA, 5min) and annealed (400° C, 5 min) twice, and then left to cool down to room temperature. It is critical that the Cu(111) crystal is not above room temperature prior to the Co deposition, as a warm crystal will lead to an alloying effect between the Co and Cu(111) that will prevent pristine Co nano-island growth.

After the Cu(111) crystal has been cooled to room temperature, it is placed in front of a Co evaporator that has been calibrated to evaporate approximately half 0.5 mL per minute. In the experiment described here the evaporator was an e-beam type evaporator composed of W filament near a 2mm diameter Co rod (Alfa Asear, 99.99+%). For our geometry, the correct evaporation rate typically occurred at 2kV and 6.5 mA emission current. Prior to evaporation, the evaporator is held at these conditions for 3 min with the shutter closed to allow outgassing of impurities. The shutter is then opened for 30 sec and the Co is deposited onto the Cu(111) surface. After the evaporation is complete, the Co evaporator is turned off and the Co/Cu(111) sample is moved *as quickly as possible* to the STM chamber and into the cryostat to be cooled. It is critical that the sample be cooled as soon as possible to prevent intermixing and alloying between the Co islands and the Cu(111) surface. Such intermixing will destroy the magnetic character of the islands.

Figure 3-8A shows a typical topographic image of a Co/Cu(111) sample grown as described. The Co forms 2mL thick triangular islands that are either lattice matched to the underlying fcc Cu(111) lattice, or are faulted and misaligned with the lattice. These two configurations can be distinguished from one another by the orientation of the triangles on the surface [44]. These configurations also lead to slight differences in their electronic structure, as can be seen in the *non-SP* dI/dV spectroscopy of the two types of islands in Figure 3-8B. The large peak close to -0.3 eV is known to arise from a *minority* surface state of the Co islands, with $d_{3z^2-r^2}$ [44, 45]. It is apparent that there is a slight shift in energy in this peak between the two types of islands. The implications of this shift is that when performing spin-polarized measurements, it is critical that only islands oriented in the same direction are compared to one another, or else one might mistake differences due to structure as differences due to spin-polarization.

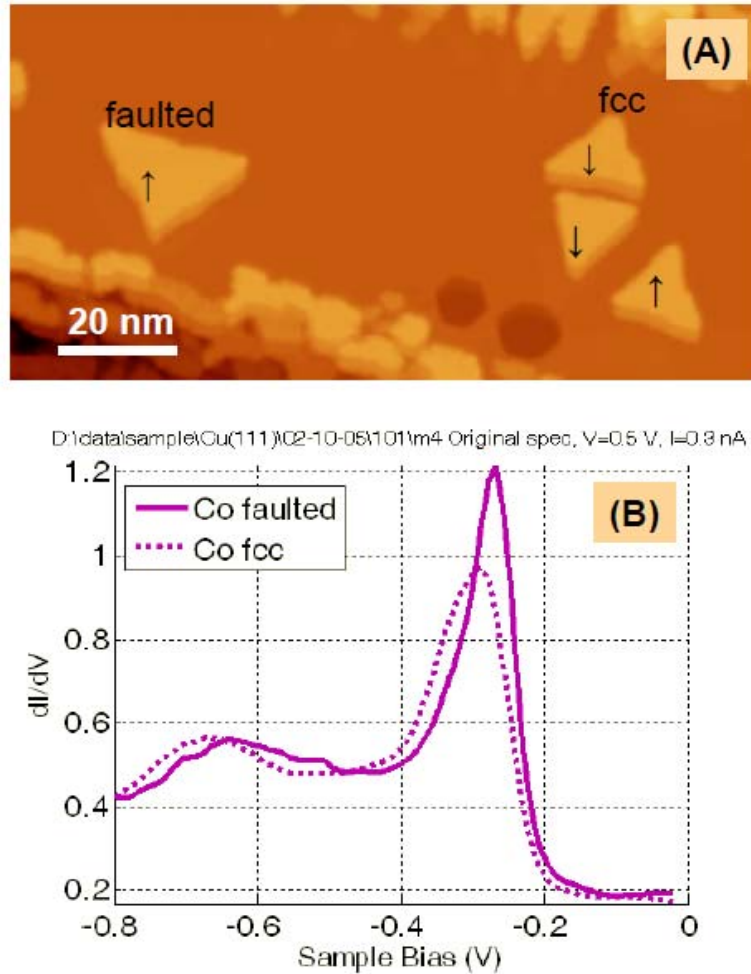


Figure 3-8 – (A) STM topograph of 2 mL thick triangular Co islands grown on Cu(111). The Co islands grow in two different crystallographic directions. **(B)** dI/dV spectra taken from islands growing in fcc and faulted configurations.

3.3.3.2 Spin-polarized dI/dV – normalization and contrast

Figure 3-9 shows the dI/dV spectroscopy of the islands in Figure 3-8A obtained with an out-of-plane spin-polarized STM tip. As can be seen, the spectroscopy on these islands displays four types of behavior corresponding to \uparrow fcc, \uparrow faulted, \downarrow fcc, and \downarrow faulted. As can be seen in this figure, the dI/dV signal for \uparrow islands has obvious differences than \downarrow islands. For example, the minority state at -0.3 V produces a much stronger signal for \downarrow islands than \uparrow islands, and this signal intensity difference flips around -0.475 V, with the \uparrow islands now showing a stronger conductivity than the \downarrow islands at -0.525 V, presumably due to the presence of a *majority* state.

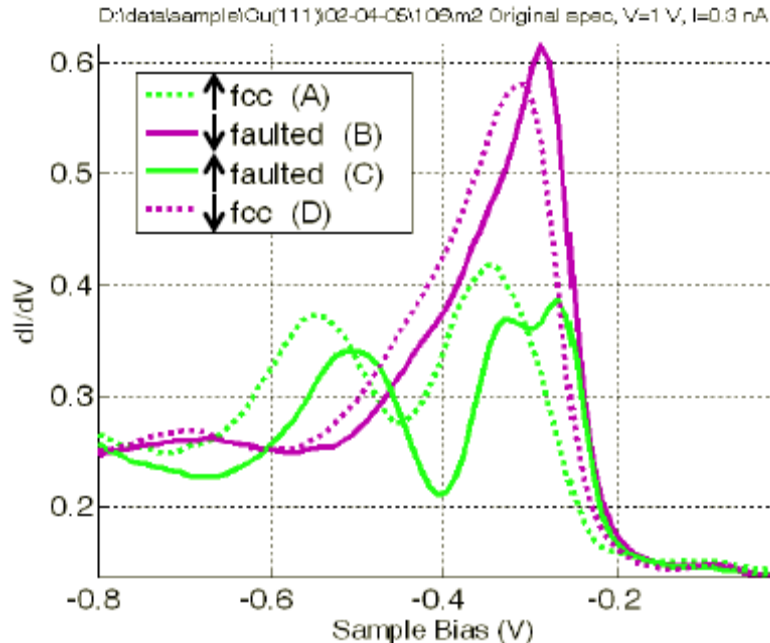


Figure 3-9 – Spin-polarized dI/dV spectra taken on four different possible island configurations (consider spin \uparrow or \downarrow and fcc or faulted island growth).

In order to accurately compare spectra taken from islands with different spin polarization, however, a normalization scheme is needed. The necessity and reasoning behind this normalization scheme is shown in Figure 3-10. Figure 3-10A shows the DOS for two fictitious islands with different electronic structure. Island 1 contains two DOS peaks at energies above -0.5 eV, while Island 2 contains one DOS feature of equal magnitude. If the STM tip is brought on top of each island with an applied sample bias of -0.5 V and at the same fixed current, then the dI/dV spectra will look as shown in Figure 3-10B. Note that the DOS feature of Island 2 looks twice as large as the DOS features of Island 1. This is due to an “STS sum rule” which requires that the integral of the dI/dV signal be equal to the setpoint current. Thus, even though Island 1 should be more conductive than Island 2, the STM tip is pulled further from the surface when on top of Island 1 in order to maintain the same current, and thus the overall intensity of all the features measured in the dI/dV curve are diminished compared to Island 2. If the spectra had been taken at the same STM tip height, the initial current for the dI/dV curve on Island 1 would have been twice the initial current than on Island 2.

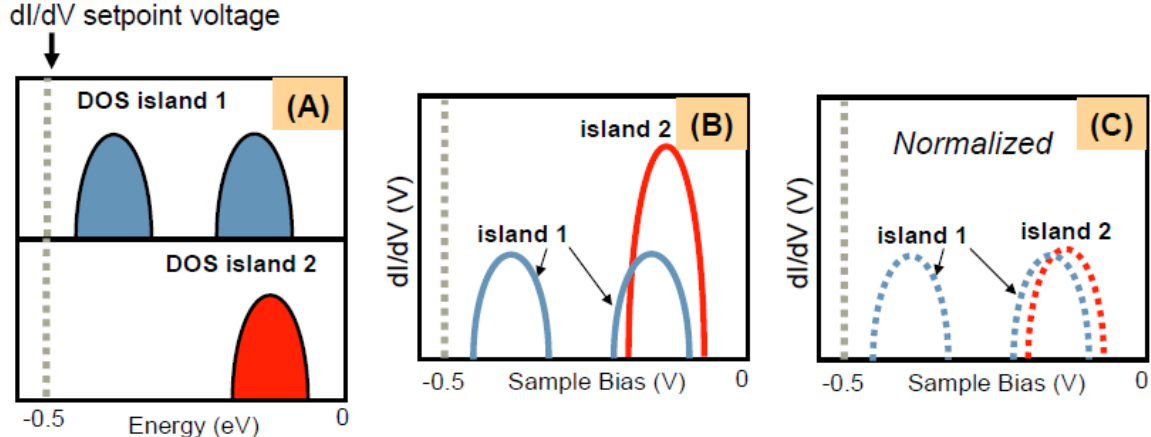


Figure 3-10 – dI/dV normalization procedure. (A) DOS of two different islands on a sample. (B) dI/dV curves obtained on both islands is setpoint voltage is -0.5V . (C) Curves normalized to account for STM sum rule.

In order to account for this effect, a normalization scheme is used with the aim of comparing the dI/dV spectra at each energy assuming the total current is equal *at that energy*. This normalization scheme is especially useful for predicting the contrast observed in a dI/dV map taken at a certain energy and at a fixed current [22, 31]. The scheme is as follows: if you have taken n dI/dV spectra from different places on a surface, then the normalized $(dI/dV)^*$ spectra is given by:

$$\left(\frac{dI}{dV} \right)_i^* = \left(\frac{dI}{dV} \right)_i \frac{I_1(V)}{I_i(V)} \quad \text{where } i = 1, 2, 3, \dots n. \quad (2)$$

Here $I_1(V)$ is the I-V curve from the first spectra obtained, and $I_i(V)$ is the I-V curve for subsequent spectra. Hence, the dI/dV signal for each spectra at a given voltage is scaled by a factor such that all dI/dV curves can be compared as if the current were the same at that particular voltage. This roughly mimicks the conditions of a dI/dV map, where the current is fixed at a given setpoint voltage, and the dI/dV signal is measured spatially [31].

Figure 3-11A,B compares spectra of \uparrow faulted and \downarrow faulted Co islands before and after the normalization procedure. As can be seen, there are differences in the expected spin contrast once the curves are normalized. For example, at $V_b \sim -0.35\text{V}$ it appears that the \downarrow island would have a large dI/dV signal than the \uparrow island, in the original spectra. However, once normalized it is apparent that there is in fact no spin contrast at this energy.

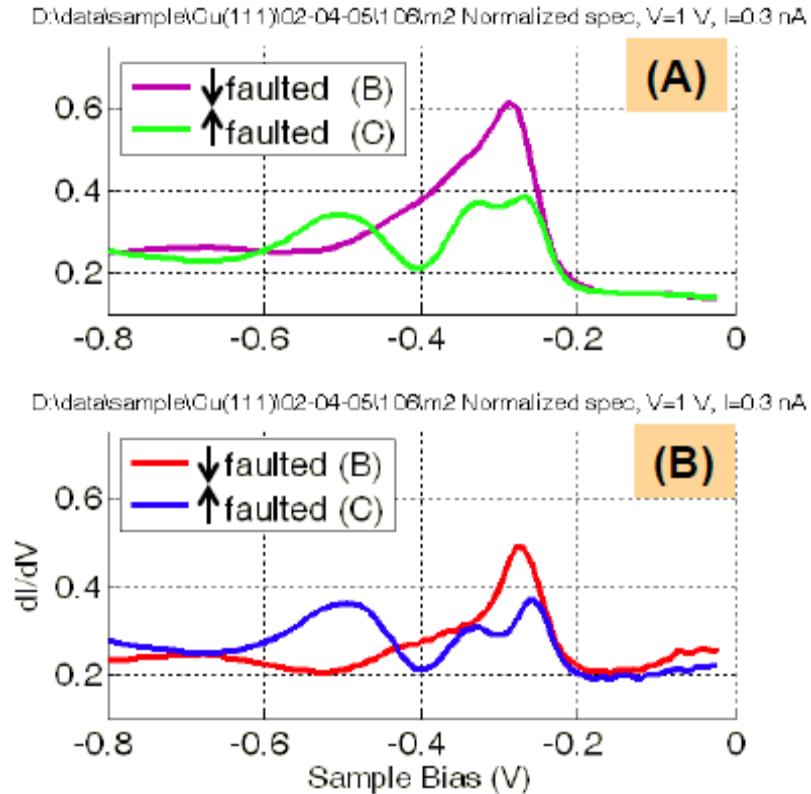


Figure 3-11 – SP dI/dV spectroscopy of \uparrow and \downarrow Co islands before (A) and after (B) normalization procedure.

Figure 3-12A shows the normalized spectra of \uparrow fcc, \uparrow faulted, \downarrow fcc, and \downarrow faulted islands. As is apparent from these spectra, there is a maximum in the spin contrast at $V_b \sim -0.55V$, with the \uparrow fcc and \uparrow faulted islands showing a signal nearly twice as strong as the \downarrow fcc and \downarrow faulted islands. A dI/dV map at -0.55 V is shown in Figure 3-12B. This figure clearly shows an increased intensity in the dI/dV signal for the \uparrow islands compared to the \downarrow islands, regardless of island orientation. When a dI/dV map is taken at -0.26 V, as shown in Figure 3-12C, the picture is slightly different. Here, for the fcc islands, the \downarrow island has an increased intensity compared to the \uparrow island, while for the faulted islands the \uparrow and \downarrow islands have similar dI/dV intensities. This behavior is expected given the normalized spectra shown in Figure 3-12A.

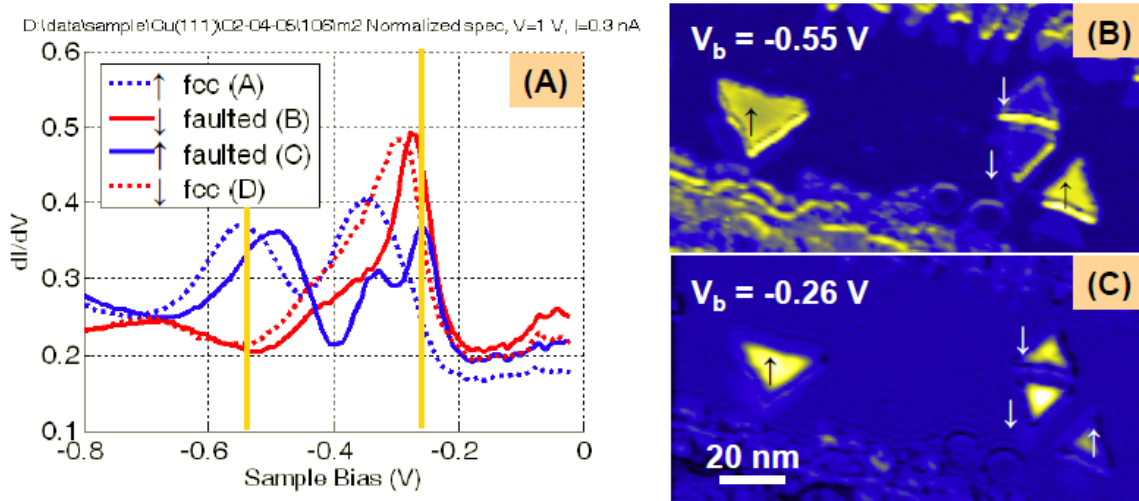


Figure 3-12 – (A) Normalized SP dI/dV spectra of Co islands in four different configurations. (B) dI/dV map of islands obtained for $V_b = -0.55$ V. (C) dI/dV map obtained for $V_b = -0.26$ V.

3.3.3.3 Poking and Pulsing SP-tip - obtaining good contrast

Often after landing on the Co/Cu(111) sample with a freshly prepared Cr coated W STM tip, there will appear to be no spin contrast in the dI/dV signal of different Co islands. At other times the dI/dV signal or the topography will show artifacts due to an anomalously shaped tip apex. In order to fix these problems, the SP-STM tip can be poked softly and pulsed with low voltages, such that the Cr coating in the apex is not lost, but that the tip is modified randomly until a desired configuration is achieved. The parameters we found for poking at pulsing the tip on the Co/Cu(111) sample were to **poke the tip 3-4 Å into the Co islands and pulse the tip 3-5 V**. These were the parameters typically used when the initial tunneling parameters were $V_b = -0.5V$, $I = 0.3nA$. **Note that neither of these processes should leave any noticeable mark on the surface.** Typically, if a blob or bump of material is left on the surface, the tip is likely to be contaminated and will not show any spin polarization afterwards. Such a tip will subsequently need to be sputtered, annealed, and evaporated onto again.

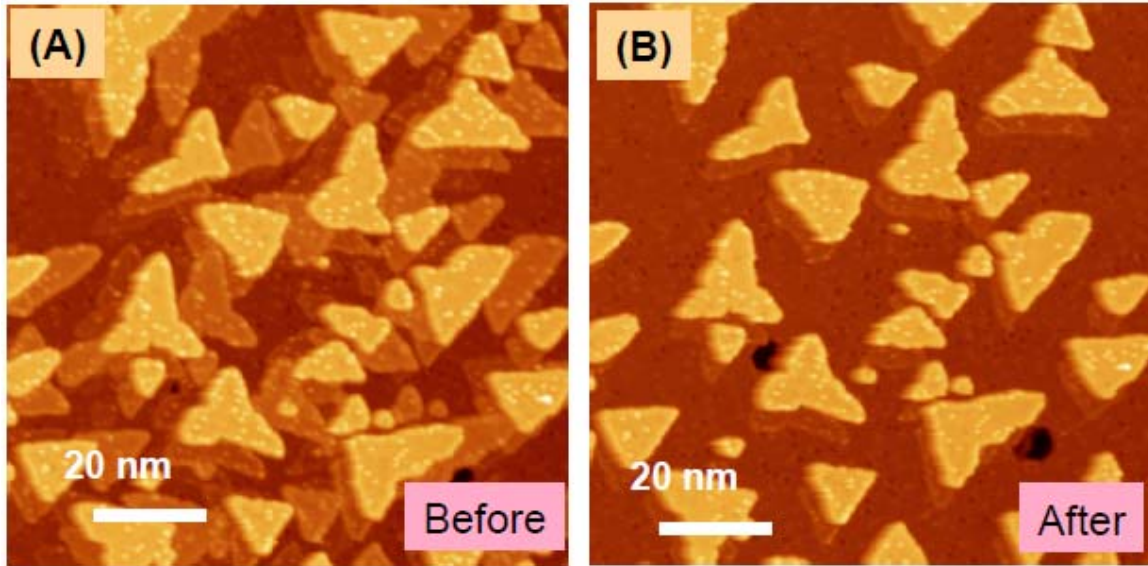


Figure 3-13 – SP-STM tip before (A) and after (B) a 3-4 Å poke onto one of the Co islands, removing the double tip but, hopefully, preserving the spin polarization of the tip. The small bumps on the surface are Fe and Cr adatoms.

Figure 3-13A shows a topographic image of a Co/Cu(111) sample after initially landing on a sample with a freshly Cr coated tip. This tip clearly has a double tip and is unsuitable for measurement. Figure 3-13B shows the same tip after a 3-4 Å poke into one of the Co islands. Similarly, Figure 3-14A shows a spin polarized spectra taken on two islands with opposite spin polarization after landing on a sample with a new SP tip. Although it is clear that this tip shows spin contrast, the spectroscopy is anomalous, with the spin contrast and some energies opposite the typical scenario. Figure 3-14B shows the spectra taken from the same oppositely spin-polarized islands after either a 3-4 Å poke or 3-5 V pulse is applied to the tip. Here the tip is still spin-polarized and shows a more typical spectra. This possibility that different SP-STM tips can display the same spin contrast at some energies while showing opposite spin contrast at other energies highlights the necessity of using caution when interpreting SP-STM data, especially when there is no internal magnetic field that can be applied so that the absolute spin direction can be known.

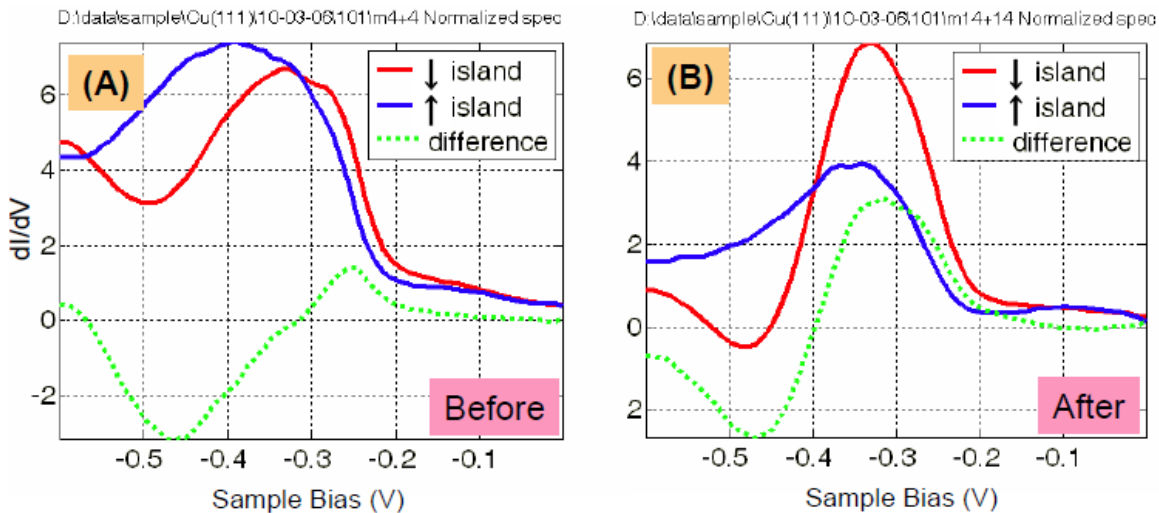


Figure 3-14 – Normalized spin-polarized dI/dV spectra taken before (A) and after (B) either a 3-4 Å poke or 3-5 V voltage pulse applied to the SP-STM tip. Spectra were obtained from the same islands before and after the tip modification. Note the reverse in spin contrast observed for $V_b = -0.35V$.

3.4 SP-STM Measurement of Cr and Fe Adatoms on Co islands

In recent years, much progress has been made in understanding the atomic scale nature of magnetic interactions through atomically-resolved spin- SP-STM measurements of magnetic thin films and individual magnetic atoms [17, 36, 38, 40, 46]. STM has also been used to probe the Kondo effect [47], where the spin of a single magnetic atom couples to the conduction electrons, and spin-flips, which can be observed via inelastic tunneling through single magnetic atoms [12, 48]. Unlike those two techniques, however, SP-STM requires the spin of the magnetic atom being probed to be fixed on the time-scale of a tunneling measurement. While it is easy to fix the spins of individual atoms inside of a ferromagnetic or antiferromagnetic crystal, isolated atoms tend to have a low magnetic anisotropy energy (MAE) due to environmental interactions. Recent XMCD [49] and inelastic spin-flip measurements [12] have shown that individual adatoms on surfaces can have MAE's ranging from less than 1meV/atom to 9meV/atom. That should be sufficient to fix the spins at 4.2K, yet those techniques were unable to resolve the spin-polarization state of individual magnetic adatoms.

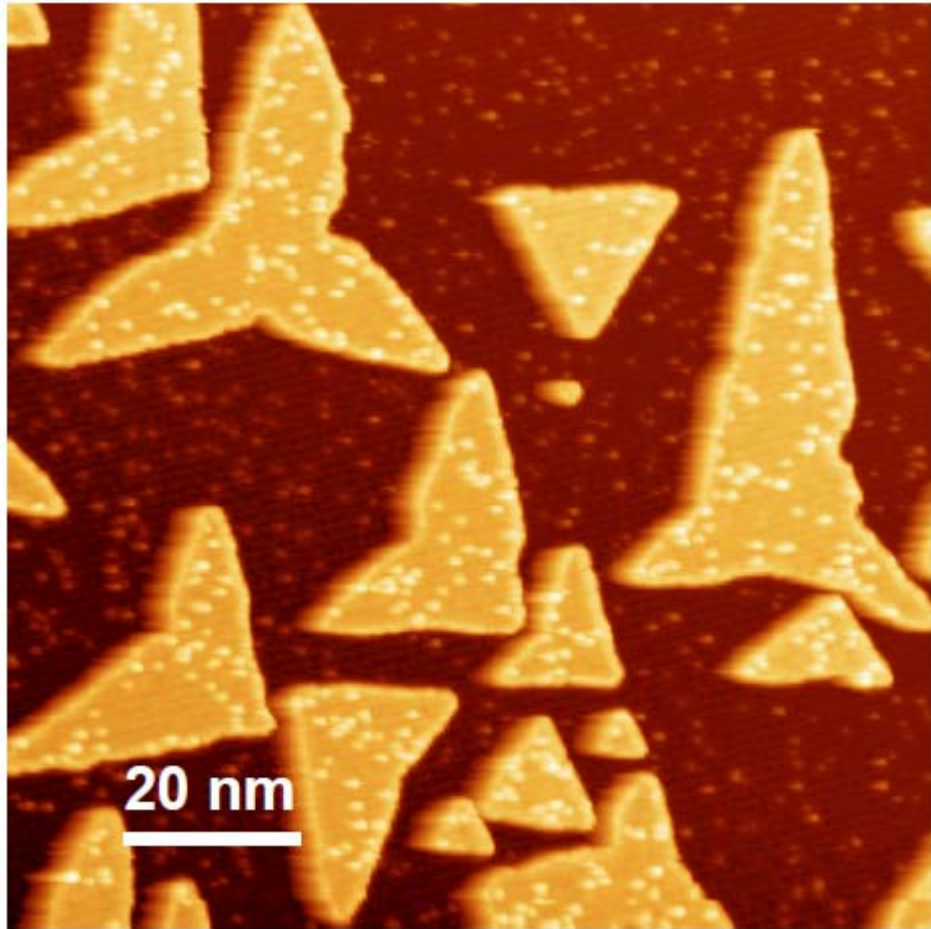


Figure 3-15 – STM topograph of Co island grown on Cu(111) with Fe and Cr adatoms evaporated on the the surface while the sample is kept cold (~10K). Scan parameters: $V_b = -0.05$ V, $I = 2\text{pA}$.

In this section I discuss the measurement of the spin-polarization state of individual Fe and Cr adatoms on a metal surface. In order to fix the adatom spin (i.e., to keep it from fluctuating in time), the adatoms were deposited onto the ferromagnetic (FM) Co nanoislands, thereby coupling the single-atom spin to the island magnetization state through an exchange interaction. Fe and Cr atoms were deposited by e-beam evaporators inside the STM chamber while the Co/Cu(111) sample was kept in the cryostat; the sample was at ~10K during the evaporation. The SP-STM tip was retracted completely during the evaporation process. High purity, 2mm diameter Fe (Goodfellow, 99.99+%) and Cr (ESPI, 99.99%) rods were used as the evaporation source, and the rate was kept low such that only 0.002 mL coverage of each material was attained. For the Cr this occurred at 2 kV and 6.3 mA emission current, and for the Fe this occurred at 2 kV and 7.7 mA emission current. Figure 3-15 shows a representative 100nm x 100nm topographic image after both the Cr and Fe adatoms have been evaporated onto the Co/Cu(111) sample. Note that Cr and Fe adatoms can be distinguished from one another by observing height differences (Cr atoms protrude 0.07 nm from the island surface while the Fe atoms protrude 0.04 nm) and from the presence of a spectroscopic feature in the Cr dI/dV signal at -0.125 V.

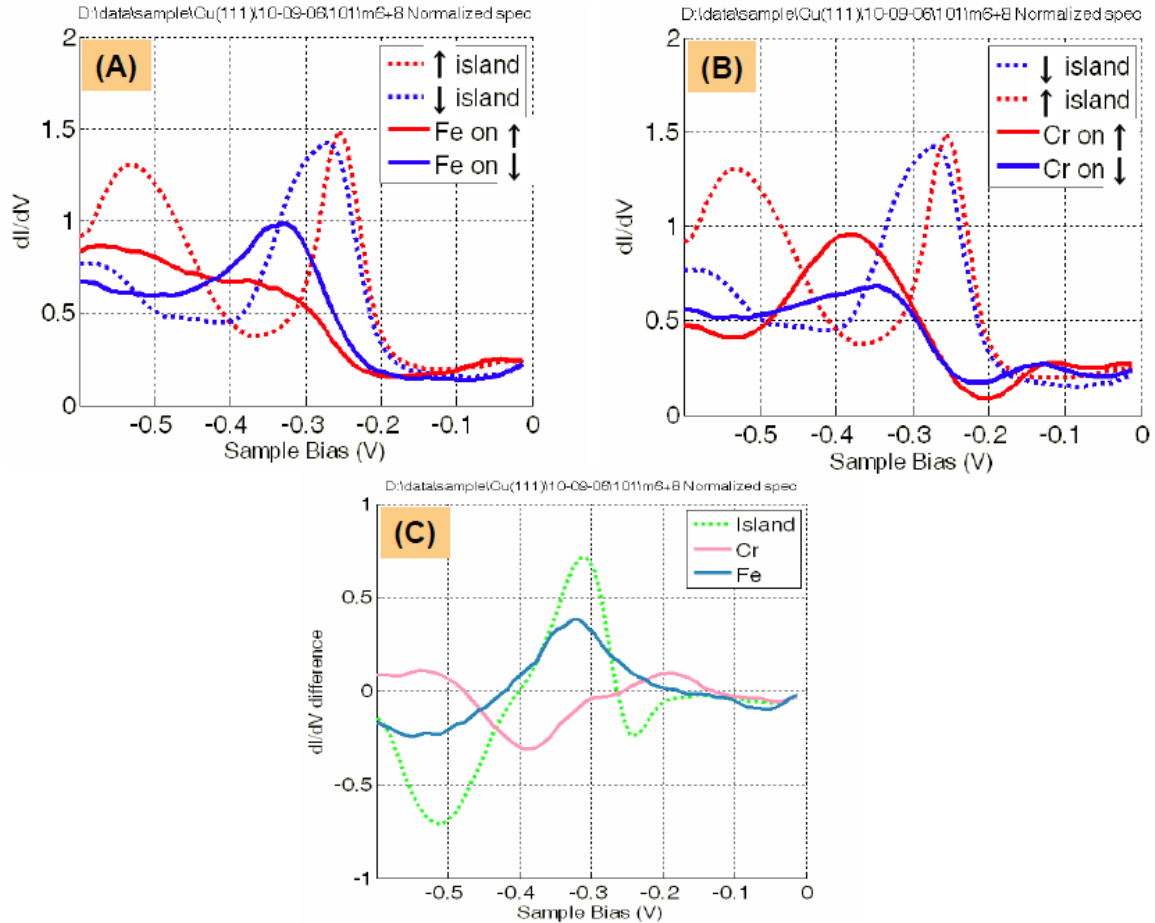


Figure 3-16 – Normalized SP dI/dV spectroscopy taken on (A) Fe adatoms resting on \uparrow and \downarrow Co islands and (B) Cr adatoms resting on the same \uparrow and \downarrow islands. (C) Difference in SP dI/dV signal for spectra obtained from \uparrow and \downarrow islands and their accompanying adatoms.

Figure 3-16A,B shows normalized dI/dV spectra taken with a spin-polarized STM tip from individual Fe and Cr adatoms on cobalt nanoislands. Also plotted in Figure 3-16A,B are the SP-STS spectra of the individual islands that the adatoms were sitting on, these two islands were oriented in the same crystallographic direction in order to avoid the structure-induced contrast described earlier. As can be seen, the two islands display opposite spin polarization, and the adatoms resting on these islands also display different SP electronic structure depending on which island they are sitting on. I here define the \downarrow island as the island with a higher dI/dV intensity at -0.3 V (a *minority* surface state). In order to compare the SP-contrast between the Cr and Fe adatoms, Figure 3-16C plots the difference between spin-polarized dI/dV spectra taken on \uparrow and \downarrow islands for the Cr, Fe, and cobalt islands. This figure clearly shows that while the spin contrast of the Fe adatom roughly follows the behavior of the Co island, the Cr adatom seems to have an opposite behavior. For example, at -0.365 V, the \downarrow island and the Fe adatoms on that island show a stronger dI/dV signal than the \uparrow island and its Fe adatoms, but the Cr adatoms on the \uparrow island show a stronger dI/dV signal than those on the \downarrow islands. Such behavior, where the Fe spin contrast follows that of the islands while the Cr spin contrast is opposite, seems to be true over a large energy range, from -0.26 V to -0.6 V (there is

some ambiguity around -0.425 V, where the contrast flips). Thus, we can ascertain that over that energy window, the spins of the Fe adatoms point in the same direction as the Co island (i.e. they are ferromagnetically (FM) coupled) while the spins on the Cr adatom are aligned opposite those of the island (i.e. they are anti-ferromagnetically (AFM) coupled. It should be mentioned, that SP-STS spectra of Fe and Cr adatoms on the bare Cu(111) substrate showed no spin contrast. Also, as a control, spectra were taken with a non-SP tip of Cr and Fe adatoms sitting on many Co islands (to ensure that some will be \uparrow and \downarrow), and no discernable contrast could be observed (see Figure 3-17).

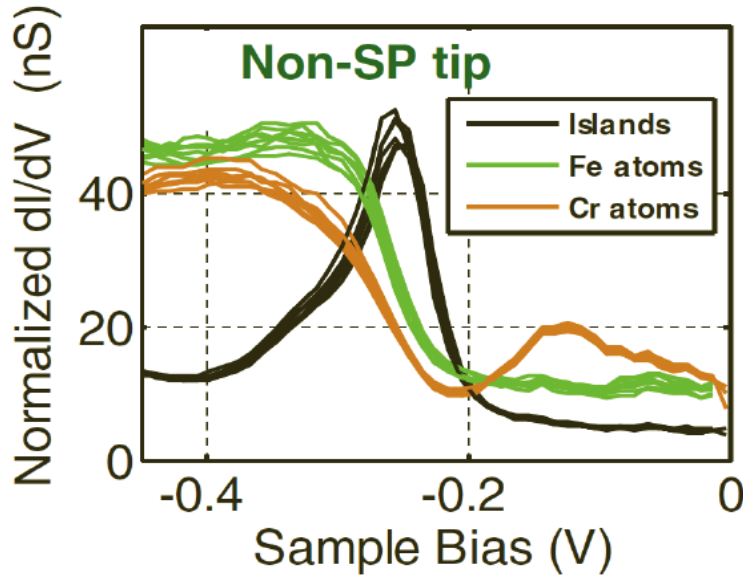


Figure 3-17 – Non-SP dI/dV spectra obtained from several Fe and Cr adatoms on many Co islands with the same crystallographic directions.

This reversed SP behavior of individual Fe and Cr adatoms can be clearly seen in spatially-resolved SP dI/dV maps. Figure 3-18A,B shows a topographic image and a color-scaled SP dI/dV map obtained for $V_b = -0.365$ V on two oppositely spin polarized Co islands with Cr and Fe adatoms on top. According to the dI/dV spectra shown in Figure 3-16, at this energy the \downarrow island should have a stronger dI/dV signal than the \uparrow island. The spin contrast between adatoms sitting on the two oppositely polarized islands is seen in linecuts through Fe and Cr atoms shown in Figure 3-18 C,D,E. Fe atoms sitting on the \downarrow island exhibit a larger dI/dV signal than Fe atoms on the \uparrow island, while Cr atoms on the \downarrow island show a smaller dI/dV signal than Cr atoms on the \uparrow island. This further confirms the ferromagnetic nature of the Fe-adatom/Co-island spin coupling and the anti-ferromagnetic nature of the Cr-adatom/Co-island spin coupling.

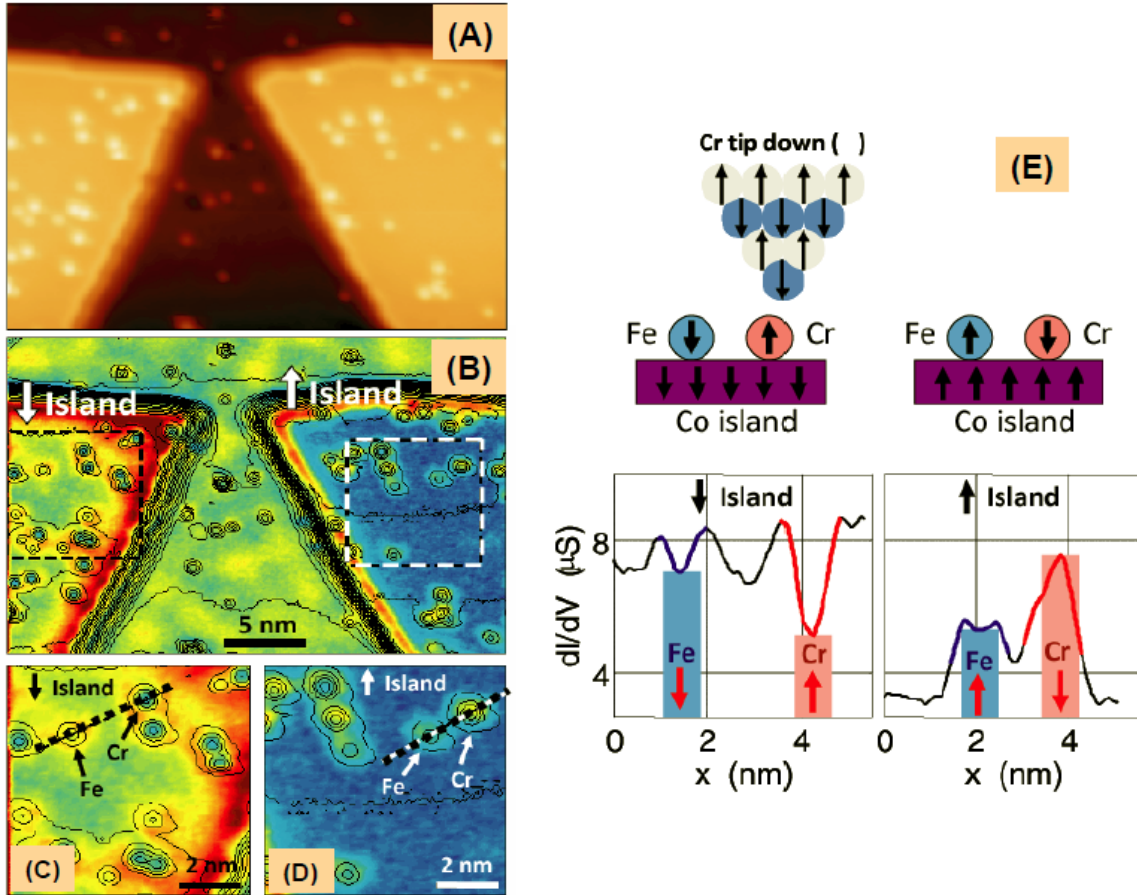


Figure 3-18 –(A) 30x20 nm topograph of two identically oriented Co islands with opposite spin-polarization and with Cr and Fe adatoms co-absorbed on top. (B) SP dI/dV map obtained simultaneously with topograph and $V_b = -0.365$. (C,D) Zoom in of outlined regions drawn in (B) showing details of Cr and Fe SP- dI/dV intensity. (E) SP- dI/dV profiles of linecuts shown in (C,D) of Fe and Cr adatoms on oppositely polarized islands, along with cartoon showing expected spin configurations.

In order to confirm our FM/AFM spin-coupling interpretation of our data we collaborated with Prof. Erwin (Naval Research Laboratory) and his group performed ab-initio spin-polarized density-functional theory calculations for Fe and Cr adatoms on a Co substrate. These calculations were performed within the generalized-gradient approximation with projector-augmented wavefunctions [50] to determine the spin coupling energies of Fe and Cr adatoms to a ferromagnetic 2-ML film of Co on Cu(111). Adsorption binding energies were calculated with adatom spin held both parallel and antiparallel to the magnetization direction of the Co film. In each case full relaxation was carried out for the adatom (at different surface binding sites) and the topmost three atomic layers (using 3x3 supercells and 2x2 sampling of the surface Brillouin zone). The calculated spin moments of Fe and Cr adatoms are 3.5 and 5.2 m_B, respectively, roughly within 10% of the gas-phase values. The resulting energies, shown in Figure 3-19, confirm that Fe adatoms prefer ferromagnetic alignment to the Co film whereas Cr adatoms prefer antiferromagnetic alignment. Within an effective Heisenberg spin Hamiltonian the energy difference between spin-parallel (FM) and spin antiparallel (AFM) alignments is equal to twice the exchange coupling energy, J, between an adatom

spin and the Co film spins. This gives $J = -0.5$ eV for Fe adatoms and $J = 0.25$ eV for Cr adatoms, favoring FM and AFM adatom spin alignment with the cobalt film magnetization respectively. These high exchange energies explain how we are able to observe adatom SP despite our environmental temperature of 4.8 K.

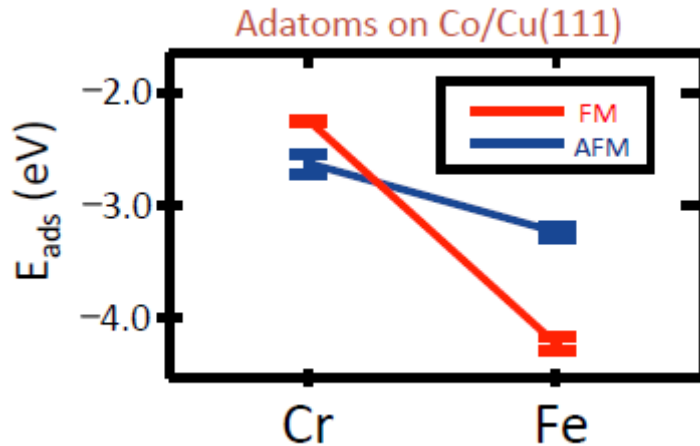


Figure 3-19 – Respective anti-ferromagnetic and ferromagnetic coupling energies for Cr and Fe adatoms on Co islands.

3.5 **SP-STM Measurement of Cu and Fe Adatoms on Co islands**

In order to compare the spin behavior in non-magnetic and magnetic adatoms on the Co islands, we also repeated the experiment by co-depositing Cu adatoms along with Fe adatoms onto the Co/Cu(111) surface, and we probed them with SP-STM. The Fe and Cu adatoms could be distinguished from each other based on their relative heights - the Cu atoms appeared “taller” than the Fe adatoms when measured at $V_b = -0.05$ V. Figure 3-20 A,B shows the normalized dI/dV SP-spectra taken with a SP STM tip on Co islands showing opposite spin polarization (but the same crystallographic orientation). Figure 3-20 C plots the normalized dI/dV difference between spectra taken on the \uparrow and \downarrow islands. As can be seen in this figure, both the Fe and Cu adatoms show the same spin contrast over all energy ranges, indicating that they are both ferromagnetically coupled to the underlying Co island. Although this may seem strange due to the fact that Cu is intrinsically non-magnetic, calculations have shown the Cu adatoms on Co/Cu(111) islands should undergo some *s-d* hybridization [51], possibly spin polarizing the Cu adatoms. This experiment provides strong evidence for such an effect.

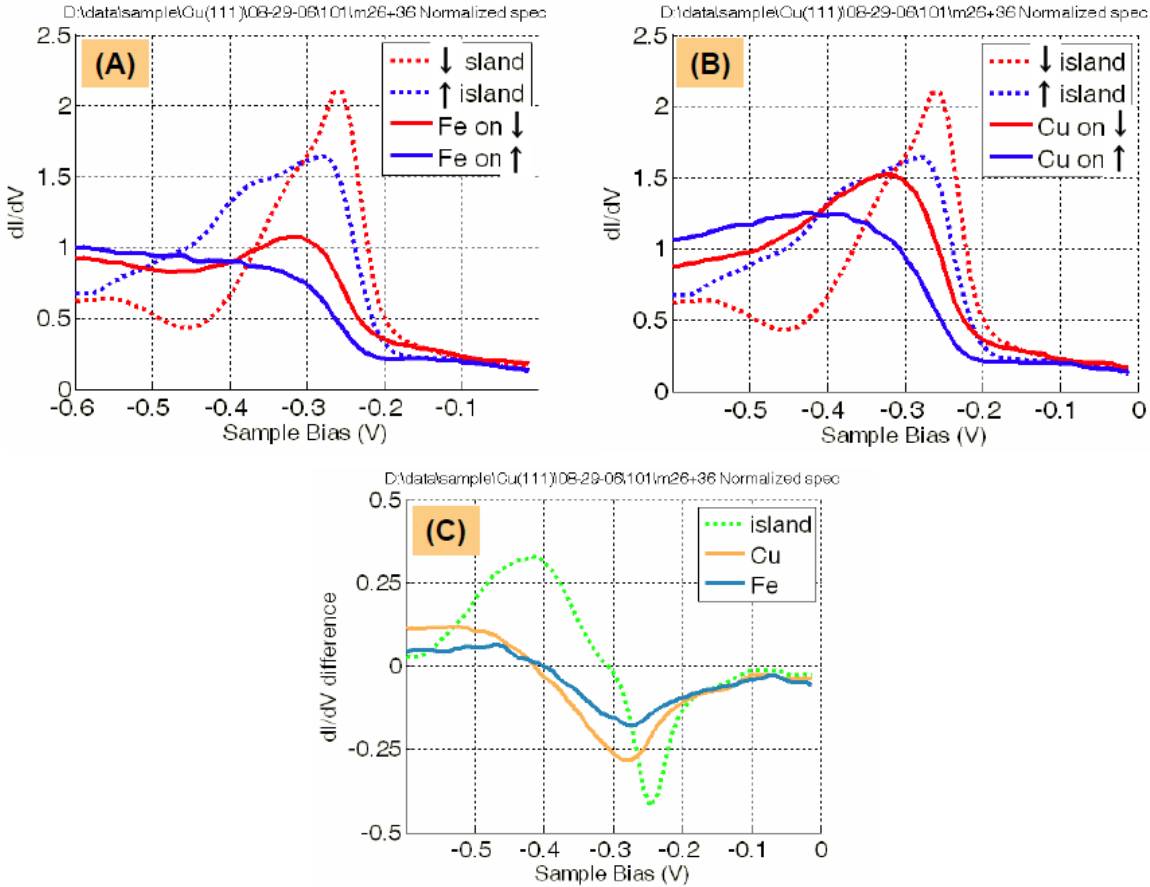


Figure 3-20 - Normalized SP dI/dV spectroscopy taken on (A) Fe adatoms resting on \uparrow and \downarrow Co islands and (B) Cu adatoms resting on the same \uparrow and \downarrow islands. (C) Difference in SP dI/dV signal for spectra obtained from \uparrow and \downarrow islands and their accompanying adatoms.

3.6 Conclusions

The ability to measure the spin-polarization state of individual adatoms opens new possibilities for characterizing magnetic coupling properties at the atomic scale. Together with the capability of STM-based atomic manipulation [52] this is a promising technique for probing the magnetic properties of nanostructures constructed from (and interacting with) individual adatoms, molecules, and impurities. The ability to perform SP-STM in general will allow for the study of exotic – but possibly localized – magnetic effect in graphene, High-T_c superconductors, ferroelectrics and topological insulators.

It is important to note, however, that one must be very careful when interpreting SP-STM data, especially with STMs that are not equipped with large magnetic fields that can be used to flip the magnetizations of samples and thus allow the experimenter to be certain that an observed effect is related to the spin polarization of the sample. This is exemplified by comparing the normalized SP dI/dV spectra taken on the Co islands in Figure 3-12, 14, 16 and 20. Although all these spectra show roughly the same shaped dI/dV curves, the spin contrast can be the same at some energies and completely opposite at other energies. Some of the error was corrected upon performing the normalization scheme, yet even after normalization this problem persists, as seen in those figures which

show normalized dI/dV spectra. This is partially due to subtle island size effects which were unknown to us when these experiments were performed [53], but it is probably mostly due to the unknown spin structure of the SP-STM tip. Although the dI/dV spectra of the non-SP Cu(111) surface can always be measured to assure that there are no spectroscopic anomalies in the DOS of the tip, the spin-polarized DOS is still unknown. This made it impossible to compare Fe, Cr and Cu adatoms measured on Co/Cu(111) islands with different SP-STM tips, and thus the measurements had to be performed simultaneously. All SP-STM experiments should thus be performed with these issues in mind.

4 STM on Graphene

4.1 Motivation

Graphene is a single layer of carbon atoms arranged in a honeycomb lattice. A single sheet of graphene is the building block of bulk graphite; however, in graphite the sheets are not stacked directly on top of one another, and thus the electronic structure of the two materials is different. Unlike graphite, the low energy quasiparticles in graphene are strictly two-dimensional and behave as if they have no mass [54]. Thus, it was an important breakthrough when – in 2004 – a single sheet of graphene was first isolated from bulk graphite [55]. Almost immediately results followed that showed that, indeed, the charge carriers in graphene behaved like “massless Dirac fermions”, displaying an anomalously spaced integer quantum hall effect [20], and showing Klein tunneling phenomena [56]. Furthermore, graphene has proven itself to be a versatile and chemically stable material that can be patterned and cut with conventional lithography techniques [57, 58], and that can be used as a substrate for creating new materials [59-61]. Thus, there is much interest in using graphene as a building block of new electronic devices, possibly filling the role of silicon in many areas [58].

From the perspective of a STM experimentalist, however, graphene is more than a material with a unique electronic structure; it is the first gate-tunable surface accessible to surface probes, and it is the first isolated two-dimensional electron gas that can be studied with STM. These two properties make it possible to perform experiments on graphene with STM that have not been possible before, such as continuously tuning – and simultaneously probing – the electronic structure of absorbed atoms and molecules [26]. It is therefore highly likely that graphene will be used as a common STM substrate for many future experiments aimed at understanding a range of phenomena, from single molecule chemistry to the fractional quantum hall effect.

However, the same properties that make graphene an attractive substrate for surface probes also create unique challenges for STM. Specifically, with graphene the STM tip becomes a highly invasive probe, whose effects must be accounted for in order to accurately interpret the STM data. Furthermore, the very physics of tunneling from a bulk metal STM tip into the 2D graphene surface is different than the standard tunneling case, and this has a strong effect on the STS tunneling spectrum.

This section describes numerous STM and STS experiments performed on the both bare graphene surfaces and graphene with absorbed adatoms. Throughout this section I describe in detail the steps required in order to perform the experiments, as well as how to properly account for the aforementioned effects in order to accurately understand the meaning of the data.

4.2 Graphene basics

4.2.1 Band-structure

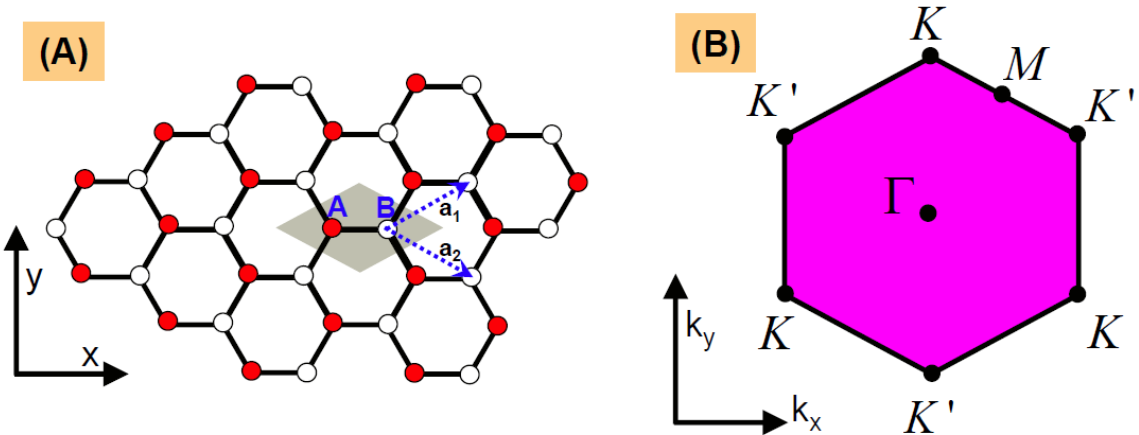


Figure 4-1 – (A) Atomic structure of graphene. (B) First Brillouin zone of reciprocal lattice of graphene.

Figure 4-1A shows a ball and stick model of a graphene sheet. The individual carbon atoms are arranged in a honeycomb lattice and held together with strong in-plane sp^2 bonds, with a nearest neighbor spacing of $a_0 = 1.4\text{\AA}$. The primitive unit cell (shown as the shaded diamond) encompasses two non-equivalent carbon atoms, A and B. The unit lattice vectors, \mathbf{a}_1 and \mathbf{a}_2 , can be written in (x,y) Cartesian coordinates as:

$$\mathbf{a}_1 = a_0 \left(\frac{3}{2}, \frac{\sqrt{3}}{2} \right) \quad \mathbf{a}_2 = a_0 \left(\frac{3}{2}, -\frac{\sqrt{3}}{2} \right) \quad (1)$$

The first Brillion zone of the reciprocal lattice is shown in Figure 4-1B. It is another hexagonal lattice rotated 30° relative to the real space lattice. There are four high symmetry points K, K', M and Γ , with the K and K' points being distinct from one another. The unit vectors of the reciprocal space are given by:

$$\mathbf{b}_1 = \left(\frac{2\pi}{3a_0}, \frac{2\pi}{\sqrt{3}a_0} \right) \quad \mathbf{b}_2 = \left(\frac{2\pi}{3a_0}, -\frac{2\pi}{\sqrt{3}a_0} \right) \quad (2)$$

The low energy electronic band-structure of graphene can be calculated by considering only the out-of-plane $2p_z$ orbitals of each carbon atom in the lattice [54, 62]. These orbitals form π and π^* bands that touch at the K and K'-points of the first Brillion zone. The calculation of these bands can most easily be done using a first nearest neighbor tight-binding approximation [62]. To do this, we first write the Bloch wavefunction of the $2p_z$ states as:

$$\psi(r) = \sum_R e^{ik \cdot R} (c_A \varphi_A(r-R) + c_B \varphi_B(r-R+r_0)) \quad (3)$$

where R is the set of all lattice vectors, r_0 is the 1.4Å long vector connecting the A to the B atom in the same unit cell, φ_A and φ_B are the $2p_z$ orbitals on the A and B atoms, and c_A and c_B are constants that represent the complex probability amplitude of an electron being on the A or B atoms, respectively. It follows that $|c_A|^2 + |c_B|^2 = 1$. To solve for the bands, we use the time-independent form of Schrodinger's equation, $E|\psi(r)\rangle = H|\psi(r)\rangle$, and project onto the states $\varphi_A(r)$ and $\varphi_B(r)$, obtaining two equations:

$$\langle \varphi_A(r) | E | \psi(r) \rangle = \langle \varphi_A(r) | H | \psi(r) \rangle \quad \text{and} \quad \langle \varphi_B(r) | E | \psi(r) \rangle = \langle \varphi_B(r) | H | \psi(r) \rangle \quad (4)$$

In order to expand and simplify these equations, we enact the nearest-neighbor approximation and define the following values:

$$\varepsilon_0 = \langle \varphi_{A(B)}(r) | H | \varphi_{A(B)}(r) \rangle \quad (5)$$

This is the on-site energy of the carbon $2p_z$ orbital. Since we are neglecting next nearest neighbors it follows that $\langle \varphi_{A(B)}(r) | H | \varphi_{A(B)}(r+R) \rangle = 0$ for $R \neq 0$. We also have:

$$\gamma_0 = \langle \varphi_A(r) | H | \varphi_B(r-r_0+R_{1,2,3}') \rangle \quad \text{for } R_{1,2,3}' = 0, a_0(-\frac{3}{2}, \frac{\sqrt{3}}{2}) \text{ and } a_0(-\frac{3}{2}, -\frac{\sqrt{3}}{2}) \quad (6A)$$

or

$$\gamma_0 = \langle \varphi_B(r) | H | \varphi_A(r+r_0+R_{1,2,3}'') \rangle \quad \text{for } R_{1,2,3}'' = 0, a_0(\frac{3}{2}, \frac{\sqrt{3}}{2}) \text{ and } a_0(\frac{3}{2}, -\frac{\sqrt{3}}{2}) \quad (6B)$$

γ_0 is the nearest neighbor hopping term, and is typically experimentally determined to be 2.9eV [62]. We set the next nearest neighbor hopping term to zero, e.g. $\gamma_0 = \langle \varphi_B(r) | H | \varphi_A(r+r_0+R) \rangle = 0$ for $R \neq R_{1,2,3}''$. We also set the direct overlap between neighboring $2p_z$ orbitals to be zero, e.g. $\langle \varphi_A(r) | \varphi_B(r-r_0) \rangle = 0$.

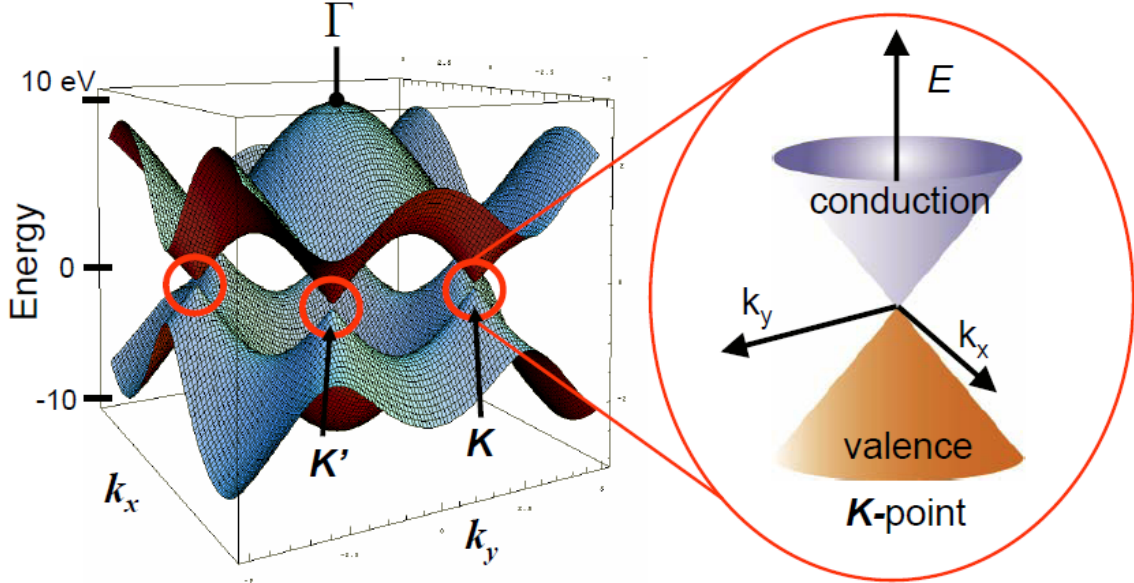


Figure 4-2 – π -bands of graphene obtained from simple tight-binding model. (Adapted from [63])

With these approximations and by taking $\varepsilon_0 \rightarrow 0$ as the reference energy, Eqns. (4) become:

$$c_A E = c_A \varepsilon_0 + \gamma_0 c_B (1 + e^{ik \cdot R'_2} + e^{ik \cdot R'_3}) = \gamma_0 (1 + e^{ik_x \frac{3}{2} a_0 (2 \cos(k_y \frac{\sqrt{3}}{2} a_0))}) \quad (7A)$$

and

$$c_B E = c_B \varepsilon_0 + \gamma_0 c_A (1 + e^{ik \cdot R''_2} + e^{ik \cdot R''_3}) = \gamma_0 (1 + e^{-ik_x \frac{3}{2} a_0 (2 \cos(k_y \frac{\sqrt{3}}{2} a_0))}) \quad (7B)$$

These equations can be solved for E as a function of (k_x, k_y) , giving:

$$E(k) = \pm \gamma_0 \sqrt{1 + 4 \cos(k_x \frac{3}{2} a_0) \cos(k_y \frac{\sqrt{3}}{2} a_0) + 4 \cos^2(k_y \frac{\sqrt{3}}{2} a_0)} \quad (8)$$

Figure 4-2 shows $E(k)$ plotted in reciprocal space. As can be seen in this figure, the Fermi level is at the K and K' points, where the valence and conduction bands touch. In order to study the low energy states at these high symmetry points, we expand Eqns. (7) and (8) about $K = 0k_x + \frac{4\pi}{3\sqrt{3}}k_y$. Substituting $\kappa_x = k_x$ and $\kappa_y = k_y - \frac{4\pi}{3\sqrt{3}}$ we can use $e^{\pm ik_x \frac{3}{2} a_0 (2 \cos(k_y \frac{\sqrt{3}}{2} a_0))} \rightarrow \frac{3}{2} a_0 (-\kappa_y \pm i\kappa_x)$ and rewrite Eqns. (7) in a matrix form to get:

$$\frac{3}{2} \gamma_0 a_0 \begin{pmatrix} 0 & -\kappa_y - i\kappa_x \\ -\kappa_y + i\kappa_x & 0 \end{pmatrix} \begin{pmatrix} c_A \\ c_B \end{pmatrix} = E \begin{pmatrix} c_A \\ c_B \end{pmatrix} \quad (9)$$

The solution to this equation is:

$$E = \pm \frac{3}{2} \gamma_0 a_0 |\kappa| = \hbar v_f |\kappa| \quad (10)$$

Where $|\kappa|$ is the length of the k -vector measured from the K -point and $v_f = \frac{\frac{3}{2} \gamma_0 a_0}{\hbar}$ is the Fermi velocity of the graphene, which is typically measured to be $1.1 \times 10^6 \text{ m/s}$ [55, 64]. Eqn. 10 shows that the quasiparticle dispersion relation near the Fermi level is linear, giving the quasiparticles an effective mass of zero. Thus, the quasiparticle bandstructure near the Fermi level of graphene appears as two cones – one for the valence and conduction bands each – that touch their points at the K and K' points, as shown in Figure 4-2. The point where they touch is referred to as the “Dirac point”. The dispersion relation is isotropic in the (k_x, k_y) plane about the K (or K') point, and this holds up to $\pm 1 \text{ eV}$, where $|\kappa|$ in the K - M direction is $\sim 15\%$ longer than $|\kappa|$ in the K - Γ direction [65], a difference due to the “trigonal warping effect” [62]. It is important to note that this low energy, isotropic, linear dispersion result holds even when next nearest neighbors are taken into account, or when the calculation is performed using *ab initio* techniques [66].

The charge density of the graphene surface can change either by doping with impurities [67] or by application of an external electrostatic gate [55]. The position of the Fermi level (relative to the Dirac point) shifts as the charge density of the graphene surface changes. This relation can be calculated by considering a linear dispersion and a 2D material, and given by:

$$\Delta E = \hbar v_f \pi \sqrt{n} \quad (11)$$

Typically, the charge density can be varied by $\pm 3 \times 10^{12} \text{ cm}^{-2}$ by application of an electrostatic backgate, leading to shifts in the Dirac point energy by $\pm 400 \text{ meV}$. The density of states (DOS) of graphene can be obtained from differentiation of Eq. (11) and is given by:

$$DOS(E) = \frac{\partial n}{\partial E} = \frac{2E}{\hbar^2 v_f^2 \pi^2} \quad (12)$$

Here E is the energy away from the Dirac point. Thus, graphene displays a linear density of states that increase away from the Dirac point, where the density of states of zero. This density of states is shown in Figure 4-3 for the neutral, electron doped and hole doped cases. As can be seen, the Dirac point can be moved above and below the Fermi level.

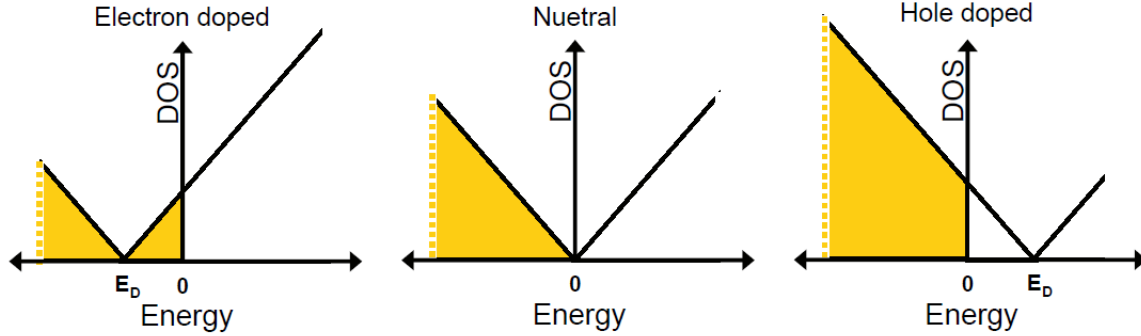


Figure 4-3 – Density of states of monolayer graphene under different doping conditions.

4.2.1.1 Psuedospin

The eigenvectors of Eqn. 9 are given by:

$$\begin{pmatrix} c_A \\ c_B \end{pmatrix} = e^{i\kappa \cdot r} \begin{pmatrix} \pm ie^{-i\frac{\theta}{2}} \\ e^{i\frac{\theta}{2}} \end{pmatrix} \quad (13)$$

where θ is the angle between the κ vector and the k_x - axis. The $e^{i\kappa \cdot r}$ part of this eigenstate is simply a plane wave, but the second part is a vector whose top and bottom components represent the relative phases of the probability amplitude for the electron to be on the A and B atoms of the lattice, respectively. This vector changes depending on the direction of the crystal momentum, $\vec{\kappa}$, and is referred to as the “pseudospin” of the quasiparticle. In the most important case, we find that the value of the pseudospin for a certain $\vec{\kappa}$ is orthogonal to the pseudospin accompanying the state $-\vec{\kappa}$. For example, if $\vec{\kappa}$ is along the k_x direction then $\theta=0$ and the pseudospin is $\begin{pmatrix} i \\ 1 \end{pmatrix}$, while if $\vec{\kappa}$ is along the $-k_x$ direction then $\theta=\pi$ and the pseudospin is $\begin{pmatrix} 1 \\ i \end{pmatrix}$. These two vectors are orthogonal, and thus the overlap between the $-\vec{\kappa}$ and $\vec{\kappa}$ states is zero. This effect leads to a number of interesting effects in graphene that have analogies with relativistic particles, such as Klein tunneling [68]. To a first order approximation, it also leads to a reduction in the backscattering of the graphene quasiparticles, although backscattering can still be directly observed in STM, as will be shown in later sections of this thesis.

4.2.1.2 σ – bands

In addition to the π -bands in graphene, σ -bands are formed due to the in-plane sp_2 hybridized orbitals. Figure 4-4 shows the full band structure of graphene including both π and σ -bands [62]. As can be seen in this figure, at the Γ -point the σ -bands have an energy much lower energy than the π -bands. Typically, at the Γ -point the σ -bands are at

an energy minimum which is calculated and measured to be at $\pm 4\text{eV}$ [69], meanwhile, the π -bands are at an energy maximum, which is typically expected to be $\sim \pm 10\text{eV}$ [62]. For most transport experiments, the σ -bands have little significance due to their distance from the Fermi level, however, it will be shown later in this thesis that the σ -bands play an important role for tunneling experiments in graphene.

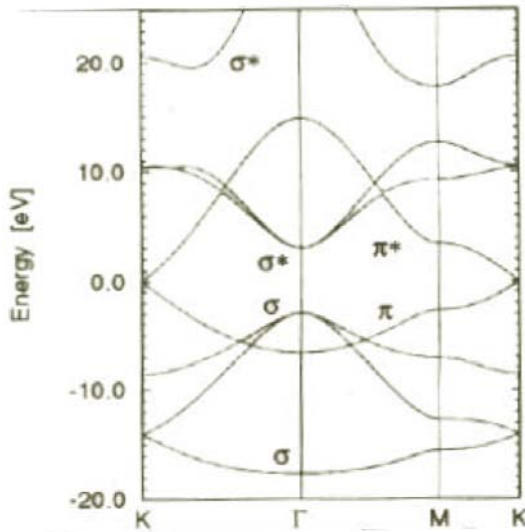


Figure 4-4 – Complete electronic band structure of graphene showing both π and σ -bands. (Adapted from [62])

4.3 Graphene synthesis and sample mounting/annealing

4.3.1 Overview

It has been known since at least the early 1990's that it was possible to grow graphene epitaxially, both by thermodecomposition of hydrocarbon gases on metallic surfaces[70], and by annealing SiC(0001) crystals [71]. These systems, however, result in graphene layers that are coupled to highly conductive and complex surfaces which destroy many of the interesting intrinsic properties of graphene, and make it difficult to produce a useful graphene device. Thus, it is widely acknowledged that the first true isolation of graphene was by Novoselov and Geim in 2004 [55] by mechanical exfoliation onto a SiO_2 surface. This technique resulted in $\sim 10\text{-}100\mu\text{m}$ monolayer graphene flakes resting on insulating surfaces that could be individually contacted using standard lithography techniques. The carrier density of these flakes could also be changed continuously via application of a gate voltage, thus providing a two dimensional electron gas that could be probed in a similar manner as AlGaAs/GaAs 2degs, but with a different bandstructure.

Since the initial isolation of graphene, new ways of synthesizing graphene have been discovered, and graphene produced using the old methods has been re-explored. The most popular way now to produce graphene is via chemical vapor deposition (CVD) onto a hot copper surface, and subsequent etching of the copper to leave behind a

monolayer graphene sheet [72]. This can result in huge flakes (~ 1 cm) that can be placed onto any desired surface and in general makes experiments much easier.

In this section I describe how to produce and characterize graphene flakes using both the exfoliation and CVD on Cu method.

4.3.2 Mechanical exfoliation (“peeling”) of monolayer graphene

Mechanical exfoliation, or “peeling”, of graphene flakes should be performed in a room with low humidity. For our experiments we kept a dehumidifier running in the room at all times. The supplies needed for mechanical exfoliation are:

- Kish graphite (Covalent Materials Corporation, AP70 PV). HOPG and natural graphite tend to not work as well.
- Scotch Tape – (3M, “Satin Finish GiftWrap Tape” works best. The thin clear stuff is no good.)
- p-doped Si wafers with 285 nm SiO_2 grown on top
- An optical microscope.

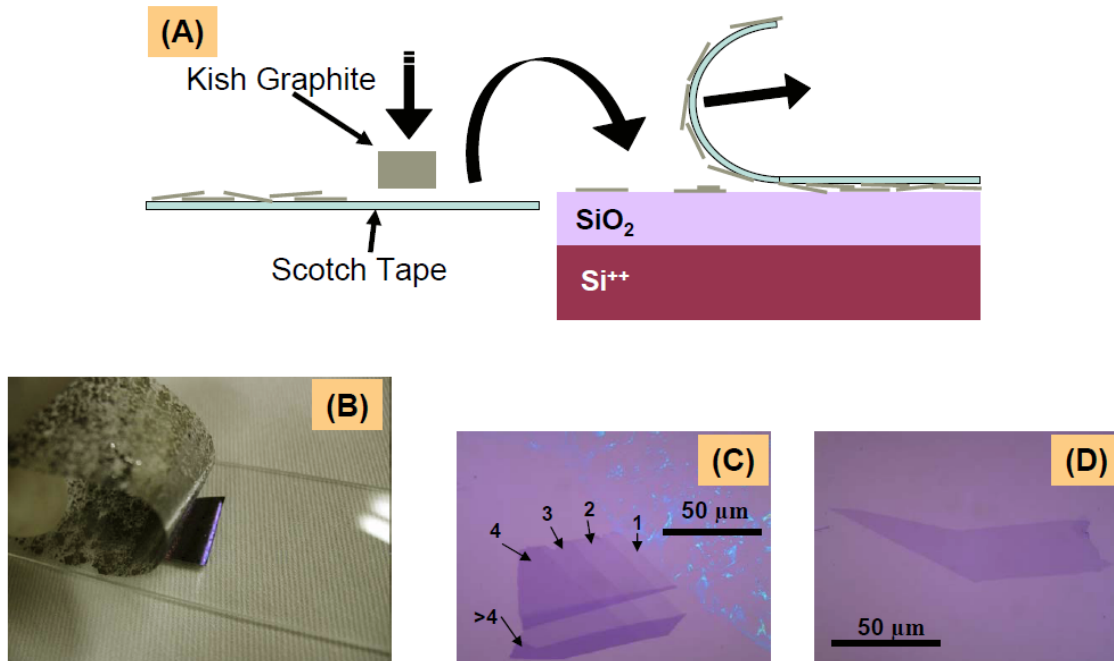


Figure 4-5 - (A) Cartoon showing Scotch tape method of obtaining monolayer graphene flakes. (B) Photograph of exfoliation procedure. (C) Optical microscope image of exfoliated flake containing 1,2,3,4 and >4 layers of graphene. (D) Image of a monolayer exfoliated flake.

The first step is to take a small piece of Kish graphite with a tweezers and to press it many times onto a 4-8” piece of Scotch tape. The graphite should leave behind several large pieces on the tape. Step two is to “Rorschach” the tape by folding it over again and again, such that the graphite gets duplicated onto the tape with each fold. Repeat this until the tape is mostly covered with graphite. Step three is to press the tape onto the oxide side of a $\sim 1 \times 1 \text{ cm}^2$ square of the Si wafer. Press hard using your thumb onto the

back side of the tape, rolling your thumb back and forth for 2-3 minutes. Then for another 2-3 minutes rub the back of the tape lightly using a plastic tweezers. Do not push with the tweezers, but let their own weight rest on the tape while moving them back and forth. Step 4 is to peel off the tape. This should be done slowly (over ~2min) and at a very light angle, such that the tape is kept as flat as possible and is more being vertically lifted off rather than peeled off. Figure 4-5A,B shows a schematic and photograph of the process. Note that the tape should ideally be peeled off the flake at less of an angle than shown in these two figures.

Step 5 is to place the Si wafer under an optical microscope and to search for monolayer flakes. This can be done using either a 5x, 20x or 60x objective. It generally requires some training by the eye to distinguish a single layer flake from a 2-3 layer flake. Figure 4-5C shows a piece of graphite on a SiO_2/Si wafer containing regions with 1, 2, 3, 4, and >4 regions of graphene. Pieces such as this can be used to help calibrate the eye to distinguishing monolayer pieces from multiple layer pieces. Such an image can also be processed using a computer program, and a straightforward program can be written to help distinguish monolayer from multiple layers. Figure 4-5D shows a large, isolated monolayer flake.

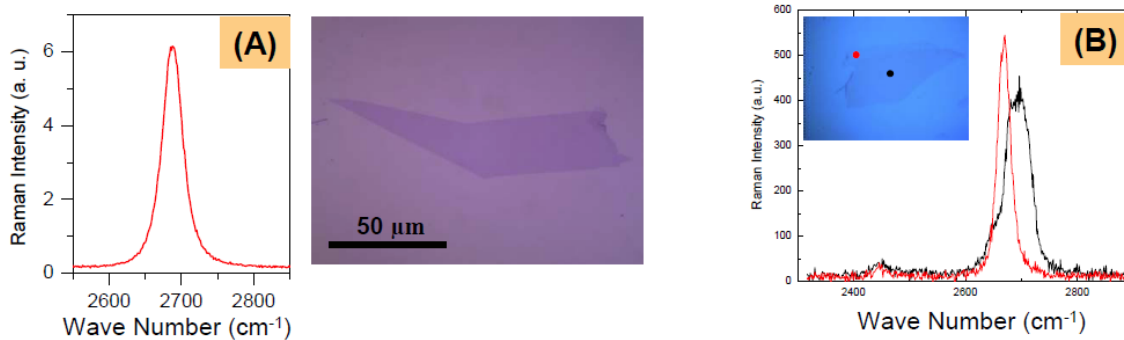


Figure 4-6 – (A) Raman spectra obtained from monolayer graphene flake on SiO_2 , along optical microscope image of flake. **(B)** Raman spectra obtained from an exfoliated flake containing monolayer (red line, red dot) and bilayer (black line, black dot) regions.

In order to ensure that the flake is truly only one layer thick, Raman spectroscopy can be performed on the flake. It has been well established by Ferrari [73] that the G' peak of graphene/graphite systems at $\sim 2700\text{cm}^{-1}$ is sensitive to the number of layers present. For a monolayer, this peak should appear as a single sharp Lorentzian, while for two or more layers multiple peaks are present. The position of the peak maximum also shifts to higher energies as more layers are added. Figure 4-6A shows the G' peak for an isolated monolayer graphene sheet. Figure 4-6B shows the G' peak for a bilayer flake (black) as well as for a small portion of the flake that is monolayer (red). It is obvious that the G' peak from the single layer is a single Lorentzian, while the G' peak for the bilayer region is more complicated.

4.3.3 Graphene production by CVD on Cu foils

The method used to produce graphene from CVD on Cu foils is largely that pioneered by Li *et al.* [72]. This technique was reproduced in our group by Lorenzo Maserati and Yang Wang. Figure 4-7 details all the steps involved in the process.

The first step (Figure 4-7A) is to cut $\sim 1 \times 1$ cm² squares out of high purity 25um thick Cu foil (*Alfa Asear*, #13382). These squares are then put into a tube furnace (in a sealed glass or quartz tube) so they are standing vertically. The tube is first flushed with 1 atm H₂ gas and then evacuated with a rough pump. The flow rate of the H₂ is then set to 2 sccm and the pressure should drop to ~ 50 mTorr. The temperature of the furnace should then be taken to 1000° C and left there for 30min. After that, 35 sccm of CH₄ is introduced and is kept at that level for 30 min. Finally, both the H₂ and CH₄ gases are turned off and the furnace is left to cool. This process causes graphene to grow on both sides of the Cu foil.

The second step (Figure 4-7B) is to place and dry PDMS on graphene on one side of the Cu foil. First the PDMS is mixed in a 1:20 (cross brand : dimethylsiloxane) ratio. The two chemicals are stirred for 10 minutes and then placed in a vacuum for 20 minutes to remove bubbles from PDMS. The Cu films are flattened by pressing them between two slides and then 1-2 drops of the PDMS is placed on the Cu film (it should cover the film.) The PDMS is then hardened by placing the Cu film on a hot plate and covered at 70° C overnight (~14 hrs.)

The third step (Figure 4-7C) is to etch away the Cu foil so we are left with only the monolayer graphene on the PDMS. First, the Cu film with PDMS on top is placed in a 40% FeCl solution for 3 to 4 minutes in order to etch off the graphene on the opposite side of the Cu foil. The Cu/graphene/PDMS is then washed in DI water twice. The Cu/graphene/PDMS is then introduced to a 0.1M (NH₄)₂S₂O₈ solution to etch away the copper. It is left here until the Cu is totally removed. The graphene/PDMS is then washed in DI water 3 times and then left in DI water at 70° C for 45 – 60 min (not longer).

The final step is shown in Figure 4-7D. Here the graphene/PDMS is removed from the DI water and dried with N₂ gas. It is then pressed hard against a SiO₂/Si wafer and then gently removed, leaving the graphene on the SiO₂. An alternative method for the transfer is to use the SiO₂/Si wafer to remove the graphene/PDMS from the DI water, so that the sample is flat on the wafer as it is being removed. The sample/wafer is then heated for 10 min on a hotplate at 70° and the PDMS is then removed, leaving the graphene on the SiO₂. When viewed in an optical microscope the SiO₂/Si wafer will show large regions covered with monolayer graphene, as shown in Figure 4-7E along with a gold contact pad and a wire bonding wire.

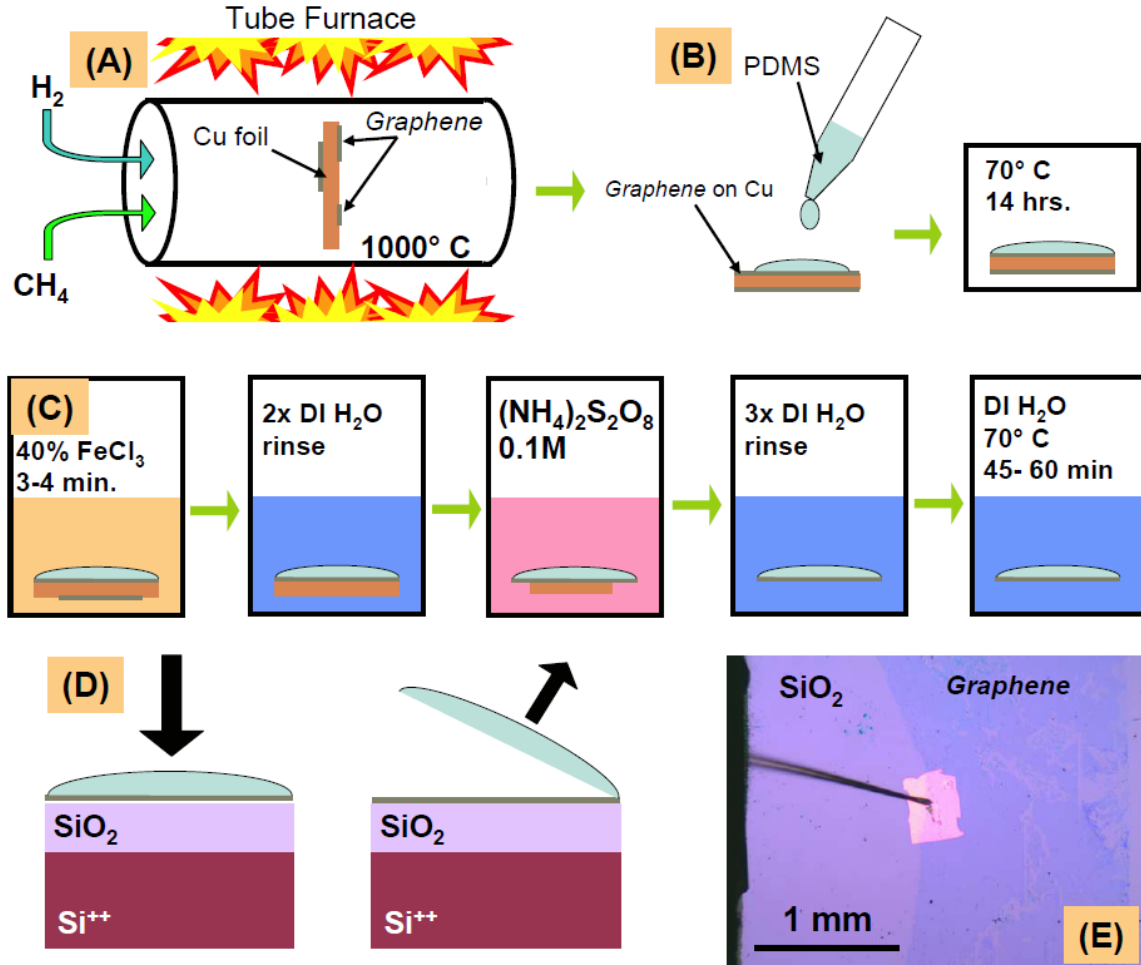


Figure 4-7 – (A-D) Cartoon showing steps necessary to prepare CVD graphene samples and stamp them onto SiO_2 . (E) Optical microscope image showing large CVD flake contacted with Ti/Au contact pad.

4.3.4 Sample mounting and UHV annealing

After monolayer graphene has been placed on the SiO_2 wafer and verified as truly monolayer, it is ready to be prepared for the Omicron STM. The first step is to evaporate Ti/Au contact pads onto the graphene. To do this we evaporate metals through photolithographed masks etched in silicon nitride membranes. The masks are aligned using micromanipulators under the optical microscope such that the contact will be touching near a desirable region of the graphene flake, but not covering it. We first evaporate 10 nm of Ti at 3\AA/sec and then cover it with 20-30nm of Au also evaporated at 3\AA/sec . Evaporating only Au straight onto the graphene will lead to large Au clusters forming all across the graphene surface.

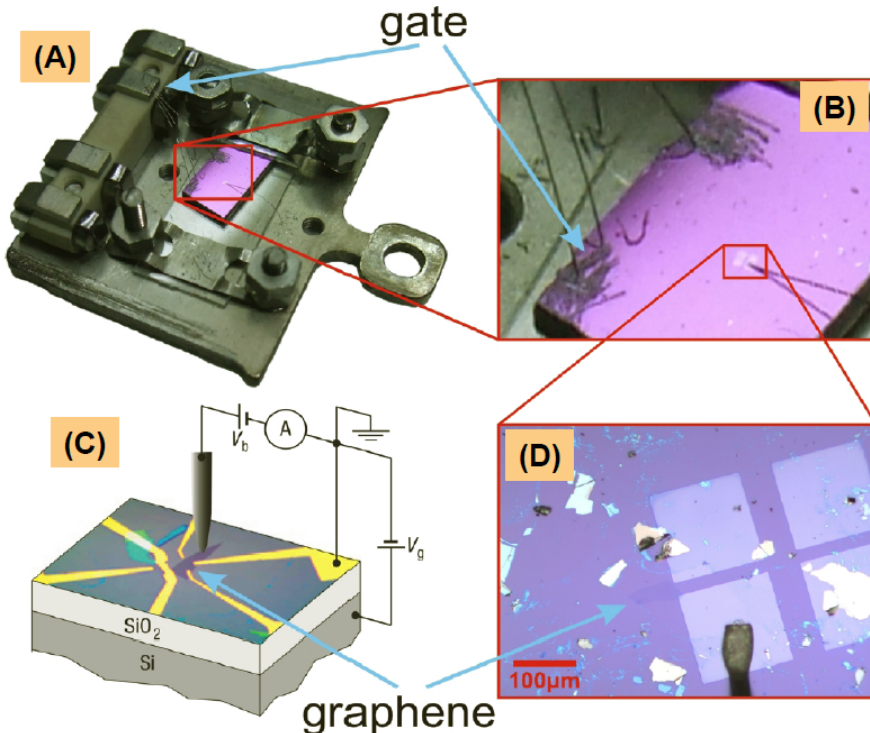


Figure 4-8 – (A) Omicron sample plate with graphene/SiO₂/Si sample mounted between two sapphire pieces and wirebonded from the gate to the Si and from the Ti/Au pad to the grounded sample plate. **(B)** Zoomed in image showing Ti/Au contact pads with Al wirebonding wire. As well as Al wires contacting gate. **(C)** Schematic of setup. **(D)** Optical microscope image of graphene flake contacted by Ti/Au contact pad. (Adapted from [74])

After the contact pads have been evaporated, the SiO₂/Si wafer is cleaved such that it fits onto the Omicron sample plate, as shown in Figure 4-8A. A piece of sapphire is placed below that Si wafer to isolate it from the sample plate, which is grounded in the STM. Another small piece of sapphire is placed on top of the silicon wafer to isolate it from the metal clamp. A corner of the SiO₂ layer is then scraped off using a diamond scribe so that the underlying Si is exposed and can be contacted as a gate. The contact pad touching the graphene is then wire bonded to the sample plate so that the graphene will be grounded. The scraped corner of the wafer is likewise bonded to one of the contact pads on the Omicron sample plate, where the gate voltage will be applied. The final sample and schematic inside the STM is shown in Figure 4-8.

Prior to placing the graphene inside the STM, it is annealed under UHV conditions at 250° C – 400° C overnight. This removes (or stabilizes) loosely bounded impurities on graphene surface due to sample fabrication and exposure to air.

Figure 4-9A shows the configuration of the sample once placed inside the STM. A long distance microscope lens (Infinity K2/SC CF-1) looks at the sample at a 30° angle while light is shone onto the sample from the opposite side. Note that because of this geometry, one must ensure than none of the wirebonding wires cross over the sample when looked at from the sides, else the camera will not be able to see the sample or the shadow of the wire will be covering the sample. Consideration must also be taken to ensure that the STM tip holder does not hit the wire bonding wires. Figure 4-9B shows two images from the long distance microscope lens of an STM tip (and its reflection)

approaching a graphene sample. Note that it is impossible to actually see the graphene flake in these images so the contact pads are used as a guide to accurately land on the sample. The resolution of the long distance lens is ~10-20 um when viewing the sample inside the STM.

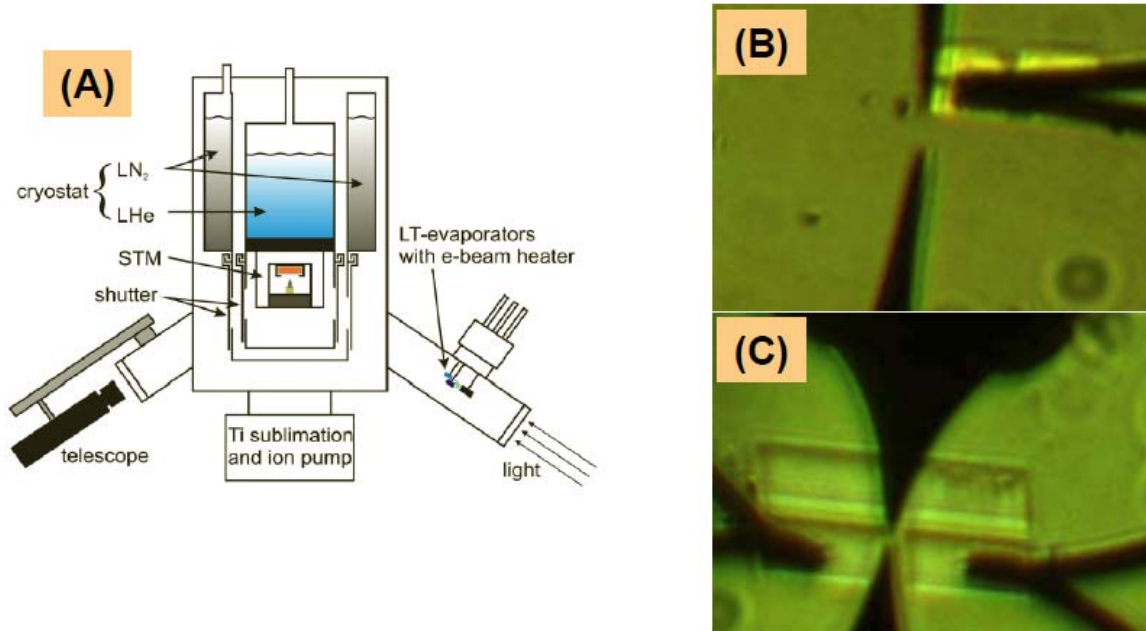


Figure 4.9 – (A) Schematic of experimental setup used to approach a graphene flake in Omicron LT-STM (Adapted from [74]). **(B,C)** Image from the telescope of STM tip approaching a graphene flake. Both real and reflection of STM tip are shown. Yellow square are Ti/Au contact pads. The graphene cannot be seen.

4.4 STM measurements on graphene

4.4.1 Outline

STM has been used to probe many two dimensional electron systems prior to graphene. For example, metallic surface states such as those on a Cu(111) surface have been imaged extensively [75], and even modified via surface modification with the STM tip [5]. Additionally, semiconductor surface states have been analyzed extensively with STM [4], and recently 2DEGs have been formed on an InAs(110) by introducing surface dopants [76-78]. In the case of the InAs(110) 2DEGs, Landau levels could even be observed in high magnetic fields [78]. STM measurements on graphene, however, are distinct from those measurements in two important ways. First and most importantly, the electronic properties of those systems could not be tuned via application of an external gate voltage as can be done in graphene. That capability not only allows us to understand the properties of graphene in a much more detailed manner, but also allows us to use graphene as a substrate for other charge density dependent measurements in the STM. Second, previously studied 2D systems did not reflect the macroscopic properties of the materials being probed, such as the total bulk conductivity or the total dielectric function. In graphene, however, the STM can directly access the electronic states involved in

transport experiments, and it can observe the potential landscape that the charge carriers see. Thus, STM experiments can help understand what limits mobility in graphene devices, and how impurities can change the behavior of such devices.

This section describes in detail several experiments performed on graphene with STM. It first explains two large effects that must be considered in a graphene STM experiments – band bending and strong inelastic tunneling. It also describes the effects of impurities on graphene, and shows how the quasiparticle lifetime in graphene can effect the STM signal.

4.4.2 STM-Graphene challenges

4.4.2.1 Quantum Capacitance and Tip-induced band bending

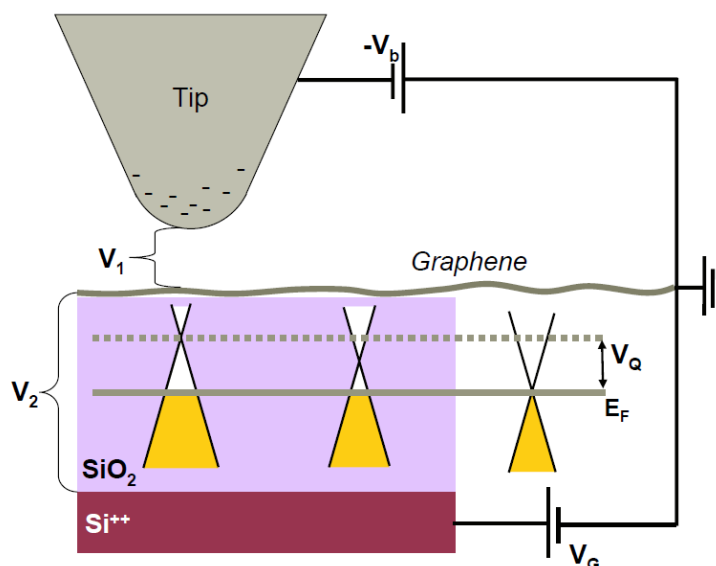


Figure 4-10 – Cartoon detailing how the STM tip gates the graphene in its immediate vicinity, inducing a voltage drop (V_Q) within the grounded graphene sheet.

When a voltage bias is applied between a STM tip and a surface a strong electric field is produced between the two due to their close proximity ($\sim 5\text{-}10\text{\AA}$). For a conventional metallic surface, this electric field has little effect due to the huge carrier density of the metal, which screens the field very efficiently. On semiconductor surfaces, however, the STM tip can shift the bands significantly [3], in some cases even producing quantum dots under the tip [76]. In the case of graphene, there is a similar problem, however the standard 3D Poisson solutions that describe screening in other systems [3, 76] no longer apply to the 2D graphene surface. Additionally, the back-gate that is used to vary the charge density in the graphene no longer behaves in the same manner when the STM tip is near the surface. To solve these problems, we adopt a quantum capacitance model used to describe back- and top-gated AlGaAs/GaAs 2DEGs [79].

A schematic of the problem is shown in Figure 4-10. Here an STM tip is positioned close to a backgated graphene sheet that is grounded and charge neutral far

away from the gate and the tip. There is a geometric capacitance between the graphene and the tip, as well as between the graphene and the back-gate. Thus, when a bias, V_b , is applied to the tip or a bias, V_G , is applied to the backgate, there is a charge accumulation on all surfaces. In the case of the graphene, which has a very low density of states, this charge accumulation shifts the position of the Dirac point away from the Fermi level. This shift means that although the graphene is grounded, the electrostatic potential in the graphene is not zero (only the *electrochemical* potential is zero, i.e. $V_{\text{graphene}} + \mu_{\text{graphene}} = 0$). Thus, there is a voltage drop *within* the graphene sheet between the portion of the sheet under the tip and the portion of the sheet away from both the tip and the gate, we call this V_Q . Kirchoff's voltage law says then that the voltage drop between the tip-graphene and gate-graphene are *not* simply V_b and V_G , respectively. Instead, we call them V_1 and V_2 . We then obtain two relations: $V_1 + V_Q + V_b = 0$, and $V_2 + V_Q + V_G = 0$. By combining these equations along with Eq. (11) and the standard geometric capacitance equations we can solve for V_Q . Note that because V_Q is related to the charge density (σ_Q) of the graphene sheet, we call the relation σ_Q/V_Q the quantum capacitance of the graphene. Note that Eq. (11) gives this relation (with $n = \sigma_Q$), and shows that for graphene the quantum capacitance is a variable quantity, that depends on the value of σ_Q .

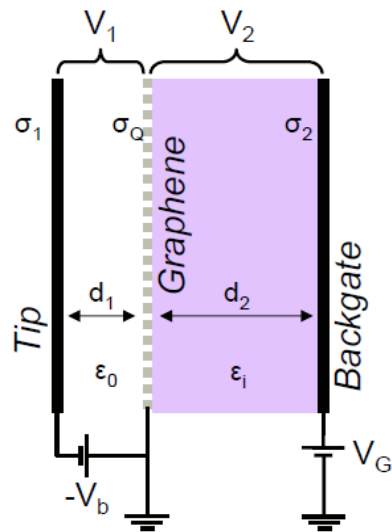


Figure 4-11 – Schematic showing the tip-sample-backgate geometry used in calculating the quantum capacitance.

We now seek to perform this calculation more formally, using a method similar to that developed by S. Luryi [79]. In this approach – as shown in Figure 4-11 - the tip is modeled as a flat parallel plate located a distance d_1 above the graphene, and the graphene is separated from a metal backgate by a dielectric with thickness d_2 and dielectric constant ϵ_i . The tip and backgate can be biased separately with bias voltages $-V_b$ and V_G , respectively. As the applied voltages are varied, the charge densities on the tip, graphene and backgate (σ_1 , σ_Q , and σ_2 , respectively) change in order to screen the applied fields. A change in σ_Q induces a change in the local chemical potential, μ , of the graphene. The graphene, however, is grounded so its total electrochemical potential is zero (i.e. $e\varphi_Q + \mu\text{-shift} = 0$, where φ_Q is the electrostatic potential of the graphene sheet).

The final equilibrium state is determined by first imposing a charge neutrality condition ($\sigma_1 + \sigma_2 = \sigma_Q$) and then minimizing the total energy of the system:

$$E_{tot} = \frac{d_1 \sigma_1^2}{\epsilon_0} + \frac{d_2 \sigma_2^2}{\epsilon_i} + \frac{4}{3} \hbar v_f \sqrt{\pi} \left(\frac{1}{e} \right)^{\frac{3}{2}} \frac{\sigma_Q^2}{\sqrt{|\sigma_Q|}} \quad (14)$$

where e is the charge of an electron, v_f is the Fermi velocity of the graphene and \hbar is Planck's constant. The solution to the minimal energy condition then leads to a relation between the electrostatic potentials of the tip, graphene, and backgate:

$$\varphi_{tip} = -\frac{d_1 \epsilon_i}{d_2 \epsilon_0} \varphi_{Gate} + \left(1 + \frac{d_1 \epsilon_i}{d_2 \epsilon_0} \right) \varphi_Q + \frac{d_1 e^3}{\epsilon_0 (\hbar v_f)^2 \pi} \varphi_Q |\varphi_Q| \quad (15)$$

where $e\varphi_{tip} = -eV_b + \Delta\Phi_{tip-graphene}$ represents the electrostatic potential difference between the PtIr tip and the graphene sample, including the applied bias, V_b , and the workfunction differences between the two materials, $\Delta\Phi_{tip-graphene}$ (Note: $\Phi_{PtIr} = \sim 5.2$ eV [80] and $\Phi_{graphene} = \sim 4.6$ eV [81]). Likewise, φ_{Gate} includes the applied gate bias, V_G , and the workfunction differences between the Si backgate ($\Phi_{Si} \sim 4.5$ eV) and the graphene. However, because the workfunction difference between the Si and the graphene (~ 0.1 V) is much smaller than the applied gate biases (~ 30 V) we can approximate that $\varphi_{Gate} \sim V_G$.

By using Eq. (15), we can approximate how much the graphene bands shift (i.e. the local μ -shift = $-e\varphi_Q$) for a given applied bias, V_b . Figure 4-12A shows the μ -shift vs. V_b for three different gate biases. (In this figure I plot the μ -shift due only to the STM tip; V_G shifts μ by a constant amount for each curve, and is subtracted from the plotted results.) Note that even at $V_b = 0$ there is a significant μ -shift due solely to the work function difference between the STM tip and the graphene. The steep portion of each curve indicates when the Dirac point is being pushed across the Fermi energy. From these plots we can extract the V_b necessary to obtain a desired change in the chemical potential ($\Delta\mu$) relative to μ -shift at $V_b = 0$, as shown in Table 1. As can be seen, the V_b necessary for a given $\Delta\mu$ is highly dependent on the applied backgate voltage. A similar dependence can be found as we vary the work function of the STM tip, as shown in Figure 4-12B. This effect introduces some uncertainty in our μ -shift estimates since the actual work function of the tip is dependent on its precise shape [82] and is expected to vary from tip to tip.

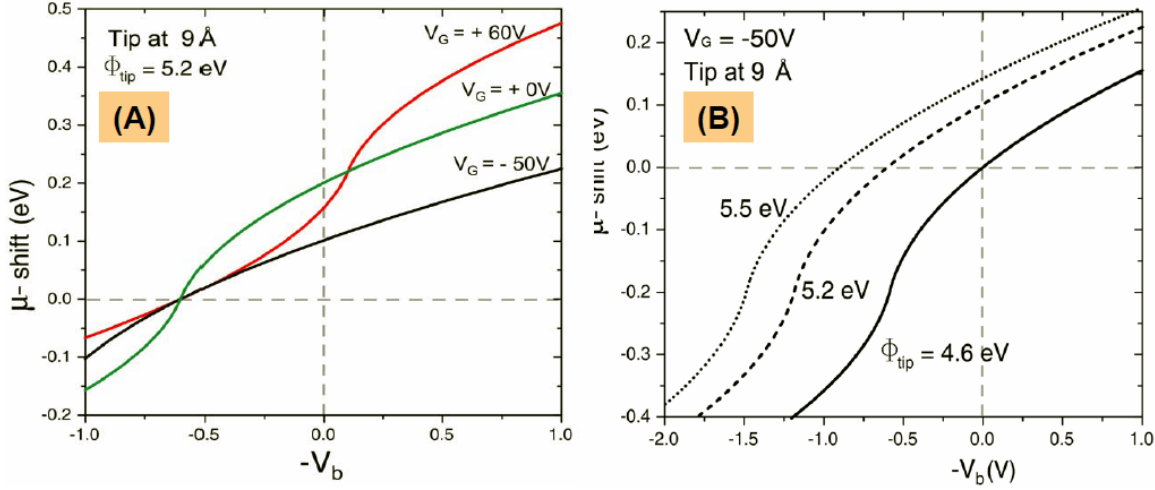


Figure 4-12 – Calculated shift in graphene chemical potential (or band energy) as a function of tip bias for (A) three differently gated graphene surfaces and, (B) three different tip workfunctions.

	$\Delta\mu = -50 \text{ meV}$	$\Delta\mu = +50 \text{ meV}$
$V_G = +60 \text{ V}$	$V_b = -100 \text{ mV}$	$V_b = 80 \text{ mV}$
$V_G = 0 \text{ V}$	$V_b = -226 \text{ mV}$	$V_b = 250 \text{ mV}$
$V_G = -50 \text{ V}$	$V_b = -324 \text{ mV}$	$V_b = 366 \text{ mV}$

Table 1 – This table shows the necessary sample biases needed to shift the bands by $\pm 50 \text{ meV}$ under different gating conditions. The different work functions between PtIr and Graphene were considered here.

Note that this behavior also affects the energy at which a spectroscopic feature (such as the Dirac point or an atomic resonance) in the graphene will be measured. For example, if a spectroscopic feature is measured at $V_b = 44 \text{ meV}$ then the actual energy, E_A , of the feature (relative to a fixed graphene bandstructure) would be expected to be somewhat lower, since:

$$eV_{meas} = E_A + \mu\text{-shift} \quad (16)$$

where V_{meas} is the measured bias at which the feature is seen. This effect is diagrammed in Figure 4-13 for a graphene sheet that is charge neutral when $V_b = 0$. When V_b is changed the tip is *not* probing states that are V_b above the Dirac point. Instead the STM is tunneling into states that are V_1 above the Dirac point. In terms of Eq. (16) $V_{meas} = V_b$ and $E_A = eV_1$.

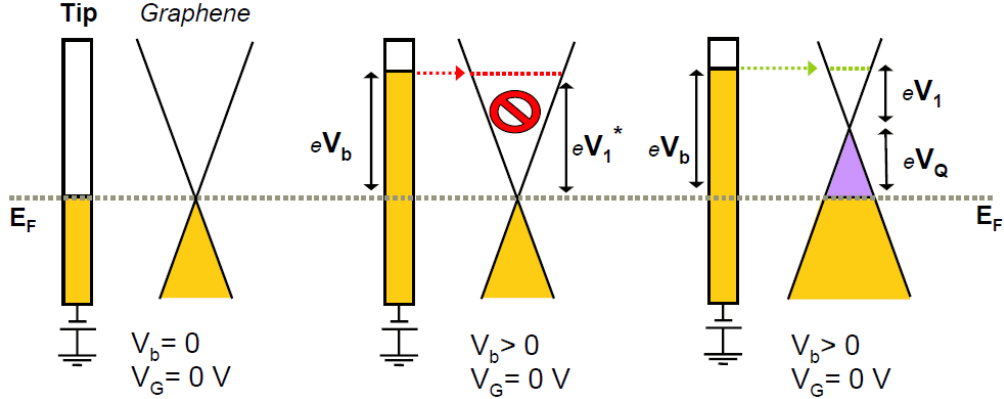


Figure 4-13 – Schematic demonstrating how applying a bias to the tip shifts the graphene bands and thus alters what states in the graphene are probed with STS. The center diagram shows the tunneling scenario with no tip-induced band bending; the right diagram show how the bands realign when tip-induced band bending is taken into account.

Eq. (15) also shows that the band-bending is sensitive to the STM tip height, d_1 . For example, Figure 4-14 shows the μ -shift as a function of V_b for an STM tip 9 Å and 5 Å above the graphene surface. In this plot we see that the band-bending effect is stronger for an STM tip closer to the surface, and that for $V_b = 0$ there is a change in μ due to a non-zero $\Delta\Phi_{\text{tip-graphene}}$ and due to V_G .

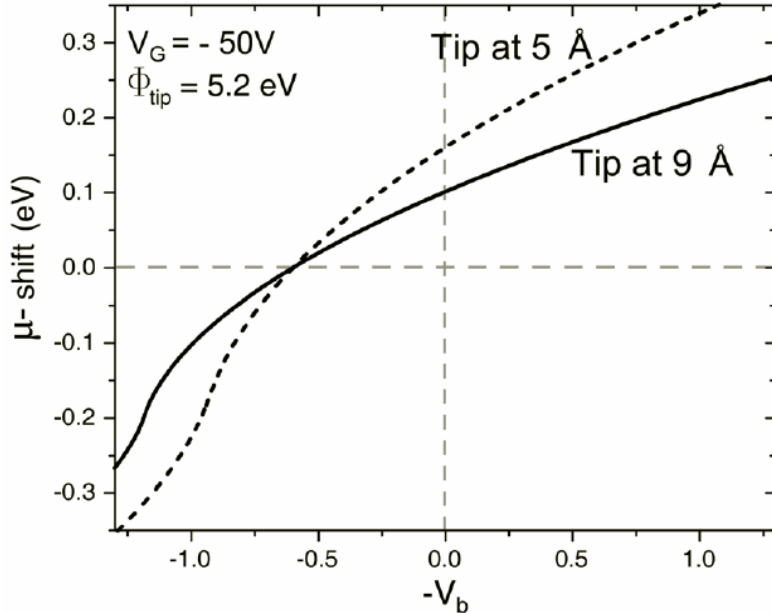


Figure 4-14 – Shift if chemical potential of graphene as a function of applied tip bias at two different STM tip heights.

As a final note, notice that Eq. (15) shows that the presence of the STM tip effects how the graphene responds to V_G . Thus, the simple geometric capacitor model that predicts a linear relationship between the charge density (n or σ_Q) and V_G [55] cannot be applied in this case.

These quantum capacitance effects are significant, with V_Q generally varying from 5-40% of V_b under typical tunneling and gating conditions. These effects display themselves constantly when performing STM on graphene they will be discussed throughout the rest of this thesis as a means of accurately discussing and interpreting the STM data.

4.4.2.2 Tip Calibration

Prior to performing any measurements on a graphene/graphite surface, it is necessary that the STM tip be properly calibrated both spectroscopically and topographically. The necessity of proper calibration is highlighted by numerous reports of artifacts in STM data taken from graphitic surfaces [83, 84]. A common cause of these artifacts is tip contamination due to delamination of graphene sheets from graphite surfaces, as well as impurities that prefer adhering to the STM tip over the inert graphene/graphite. Indeed, SEM images from STM tips that had scanned HOPG samples have shown graphite fibers growing from the apex of the STM tip [84], and hybrid TEM-STM experiments show individual graphene sheets jumping from the surface to the STM tip when small voltages are applied [85]. Thus proper tip calibration is imperative for accurate measurements on graphene or graphite. Nevertheless, the current literature has still not reached a consensus concerning what the proper tunneling dI/dV spectra of a graphene or graphite surface should look like, with at least 12 distinct published spectra [86-89].

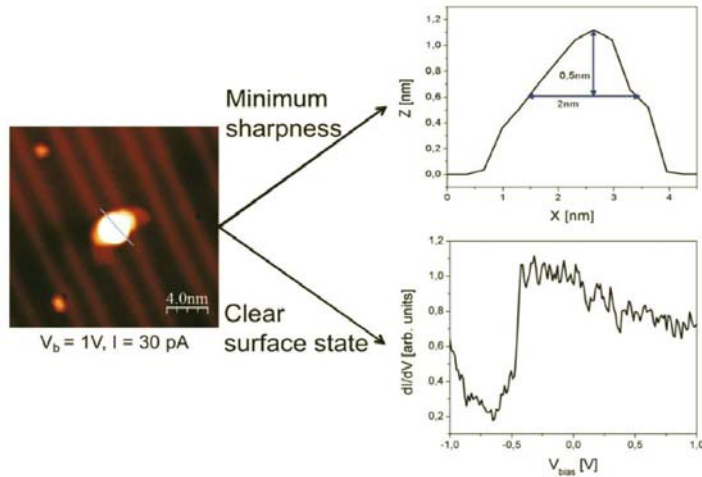


Figure 4-15 – A calibrated STM tip on Au(111) showing the necessary aspect ratio at the apex as well as clearly showing the step in its dI/dV spectrum due to the Au(111) surface state. (Adapted from [74])

In the experiments described here, the STM tip was always calibrated on a clean Au(111) or Cu(111) surface prior to the experiments, and after the experiment when necessary to confirm a result. The calibration consists of two tests as shown in Figure 4-15. First, when a dI/dV spectra is taken on the Au(111) (or Cu(111)) surface it must show a flat step in the conductivity at around $V_b = -0.45$ V due to the presence of the Au(111) surface state [75, 90]. This ensures that the tip is free of spectroscopic anomalies. Second, the tip must have a minimum sharpness of at least 2 nm wide by 0.5 nm high, which can be observed by measuring the topography of some sharp feature on

the surface. This second requirement is necessary for scanning graphene on SiO_2 because, as will be shown, the roughness of the SiO_2 induces ripples in the graphene surface that are 0.5 nm deep and 4-8 nm wide, and thus the tip must be sufficiently sharp to access the bottoms of these trenches without hitting the sides. Typically, the tip is modified on the $\text{Au}(111)$ surface by 10V voltage pulses for a completely unsuitable tip, or by 6 \AA pokes into the $\text{Au}(111)$ for a tip that is close to satisfying these two conditions.

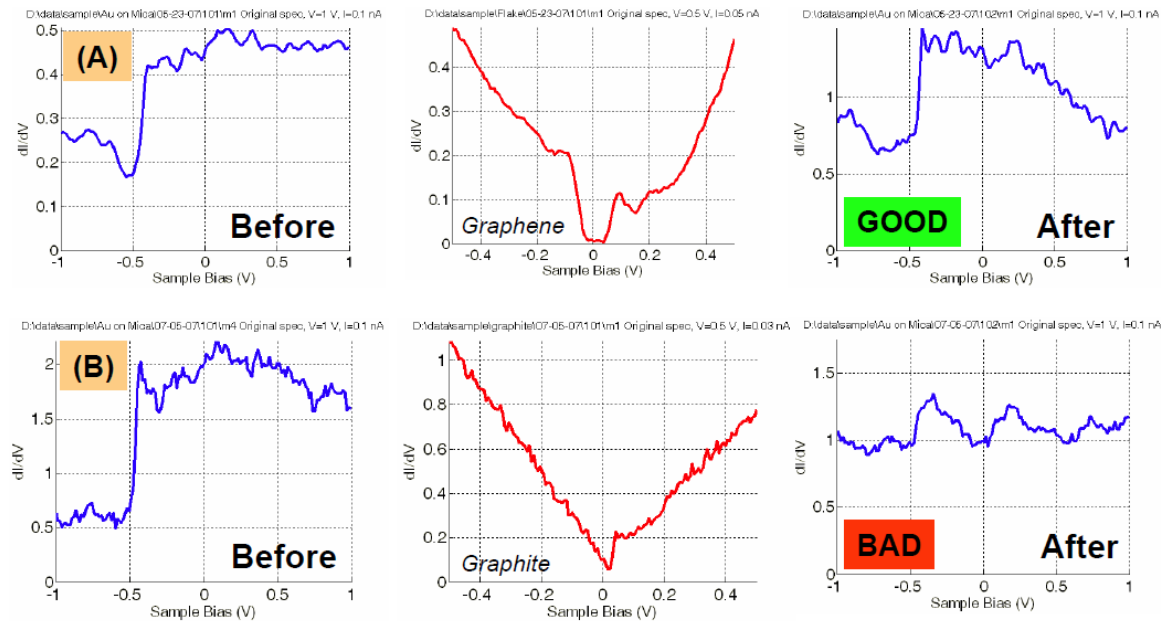


Figure 4-16 – Spectroscopic tip calibration procedure for STS measurements on graphitic surfaces showing first dI/dV curves taken on $\text{Au}(111)$ before measuring graphene/graphite, second dI/dV curves obtained from graphene/graphite, and third dI/dV curves obtained on $\text{Au}(111)$ after probing graphene/graphite. (A) Shows a tip that passed the test on graphene. (B) Shows a tip that failed the test on Graphite.

Figure 4-16A,B shows two spectroscopic calibrations before and after measuring a graphene and graphite surface. In both cases the spectroscopy on the $\text{Au}(111)$ surface prior to the measurement shows a flat step around $V_b = -0.45$ V, indicating clean tunneling conditions. When the graphene or graphite is measured, however, two vastly different spectra are obtained, one showing a ~ 130 meV gap at the Fermi energy, and one showing a ‘V’-like spectra with a minimum near the Fermi level. In order to test which is the proper spectra, the tips were checked spectroscopically on the $\text{Au}(111)$ surface after the measurement. It can be seen that the tip that showed the 130 meV gap still displays good spectroscopic properties on the $\text{Au}(111)$ surface, while the tip that showed the ‘V’-like spectra no longer displays the proper spectra when re-tested on $\text{Au}(111)$, indicating contamination.

4.4.3 Gate-dependent STS on graphene – phonon assisted tunneling

After fabricating, mounting, annealing and approaching the graphene flake device with a calibrated STM tip, STS data can be taken from the graphene surface. Figure 4-17A,B shows the STM topography of an exfoliated graphene flake resting on an

SiO_2/Si surface, similar to the device shown in Figure 4-8. Corrugations having lateral dimension of a few nanometers and vertical dimension of $\sim 1.5 \text{ \AA}$ (rms value over a $60 \text{ nm} \times 60 \text{ nm}$ area) are observed, likely due to roughness in the underlying SiO_2 surface and/or intrinsic ripples of the graphene sheet [91-93]. The graphene honeycomb lattice can be clearly resolved on top of the surface corrugation, as seen more clearly in Figure 4-17B.

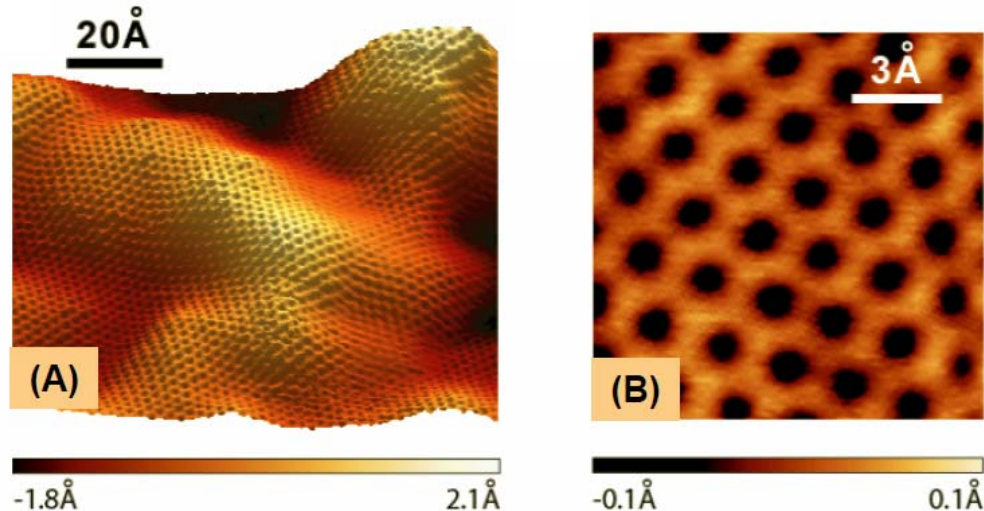


Figure 4-17 – (A) Constant current STM topograph of a monolayer graphene flake on top of 285 nm SiO_2 (-1 V , 50 pA). (B) Zoomed in STM topograph of monolayer graphene showing the honeycomb structure (-0.15 V , 40 pA). (Adapted from [89])

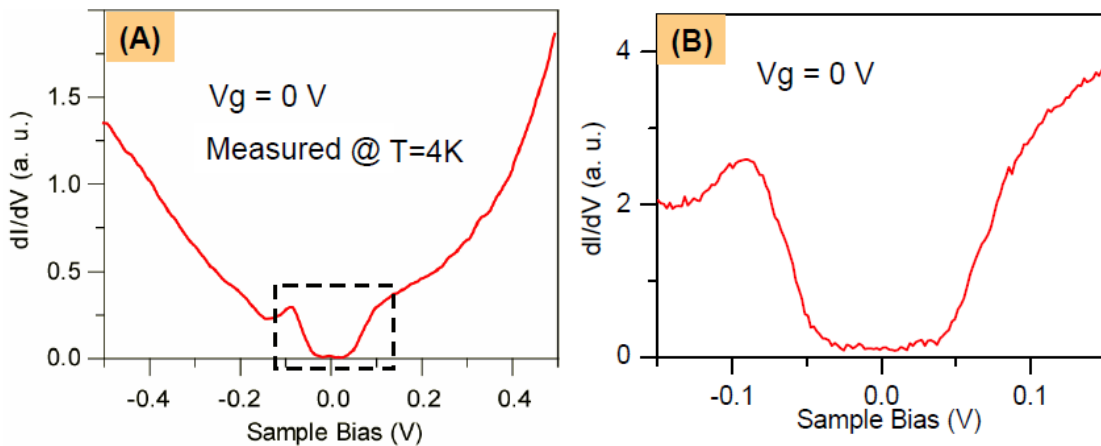


Figure 4-18 – (A) Tunneling dI/dV spectrum obtained from monolayer graphene on 285 nm SiO_2 with $V_G = 0$. (B) High resolution dI/dV spectrum emphasizing central gaplike feature.

In order to explore the electronic structure of the graphene we measured the tunneling dI/dV signal as a function of the applied tip bias. The setpoint parameters for these measurements was $V_b = -0.5 \text{ V}$, $I = 0.1 \text{ nA}$ and $V_G = 0$. Figure 4-18A shows the tunneling dI/dV spectrum for the graphene flake over the range $-0.5 \text{ V} < V_b < +0.5 \text{ V}$. Strikingly, the graphene appears to show a $\sim 130 \text{ meV}$ gap-like feature centered at the Fermi energy, $V_b = 0 \text{ V}$. This is surprising since the tunneling dI/dV spectrum of a system is usually proportional to the DOS of that system, and as shown in Figure 4-3, the DOS of graphene should be linear and ‘V’-like, with a minimum at the Dirac point. We

also notice that outside of the gap, there is a local minimum at an energy, V_D , that is $\sim 135\text{mV}$ below the Fermi energy, making the dI/dV curve asymmetric. In order to investigate the gap-like feature closer, higher resolution dI/dV data are shown in Figure 4-18B. As can be seen in this figure, the dI/dV signal does not completely go to zero inside the gap, and stable tunneling conditions can still be obtained within the gap. Thus, we can conclude that this is not like an insulating or semiconducting gap in the band structure of the graphene. When dI/dV measurements were taken at different places on the graphene surface, the energy of V_D was seen to vary, while the gap position and width remained unchanged.

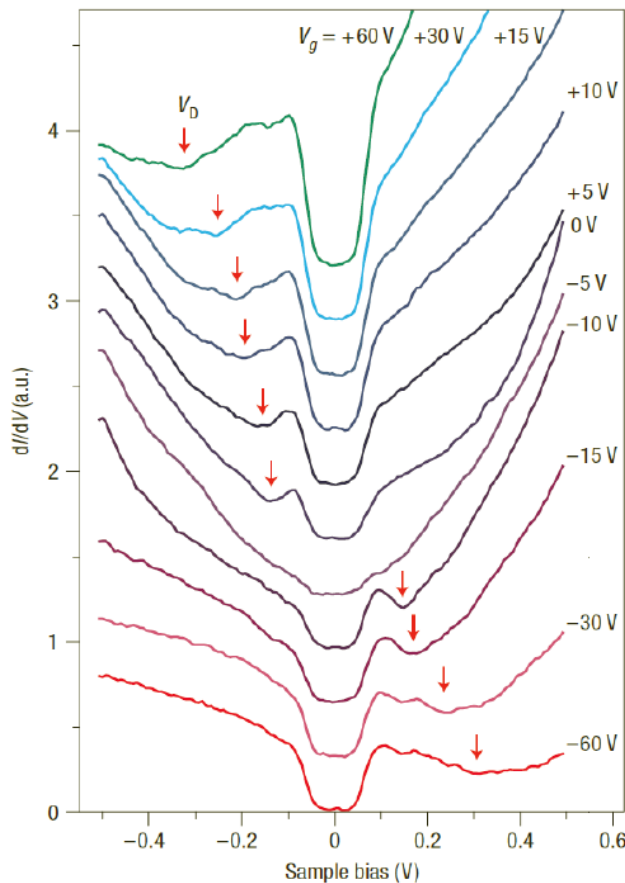


Figure 4-19 – Gate dependent STS dI/dV spectra taken from the same point on a monolayer graphene surface on 285nm of SiO_2 . The red arrow indicates the position of the conductance minima outside of the gap. (Adapted from [89])

In order to investigate this zero-bias feature further, we change the back-gate voltage (V_G) in order to change the charge carrier density of the graphene. This should shift the graphene bands relative to the Fermi level, as described by Eqns. (12) and (15), and the conductance minimum associated with the Dirac point should shift as described by Eq. (11). Figure 4-19 shows the resulting dI/dV signals as V_G is varied from -60 to $+60\text{V}$. As can be seen in this figure, the dI/dV signal does change as V_G is varied, most notably, the position of V_D moves smoothly from below to above the Fermi level. However, the gap remains fixed at $V_b = 0$ with the same width for all applied V_G . Thus, we can say with great certainty that this gap is not directly related to the band structure of the graphene. Note also that this measurement rules out the possibility of the gap being

caused by the formation of a quantum dot under the STM tip [76] since such states should shift with V_G . It also rules out a coulomb-blockade type effect since the band bending and self capacitance under the STM tip is highly gate dependent, as was shown in Section 4.4.2.1.

Another possible explanation for the gap-like feature is that it is somehow related to having a single layer of graphene on the SiO_2 surface. For example, it could be due to phonon coupling with the SiO_2 , or the formation of some exotic state through interaction between the SiO_2 and graphene, or possibly related the two dimensionality of the graphene itself. In order to rule out these sorts of scenarios, we performed tunneling dI/dV spectroscopy measurements on eight different graphitic systems in order to see if changing the thickness, doping, substrate or the specific type of bulk graphite in any way effected this gap. Figure 4-20 shows the dI/dV spectra taken from the different systems with an STM tip calibrated as described in the previous section. The systems are (1) bulk HOPG, (2,3) monolayer and bilayer graphene grown on the Si face of $\text{Si}(0001)$ [60], (4) a many (>20) layer Kish graphite piece on SiO_2 , (5,6) a neutral and heavily doped exfoliated bilayer graphene flake on SiO_2 , (7,8) a neutral and heavily doped exfoliated monolayer graphene flake on SiO_2 . As can be seen in this figure, all the graphitic system clearly show the ~ 130 mV gap centered at the Fermi energy ($V_b = 0$).

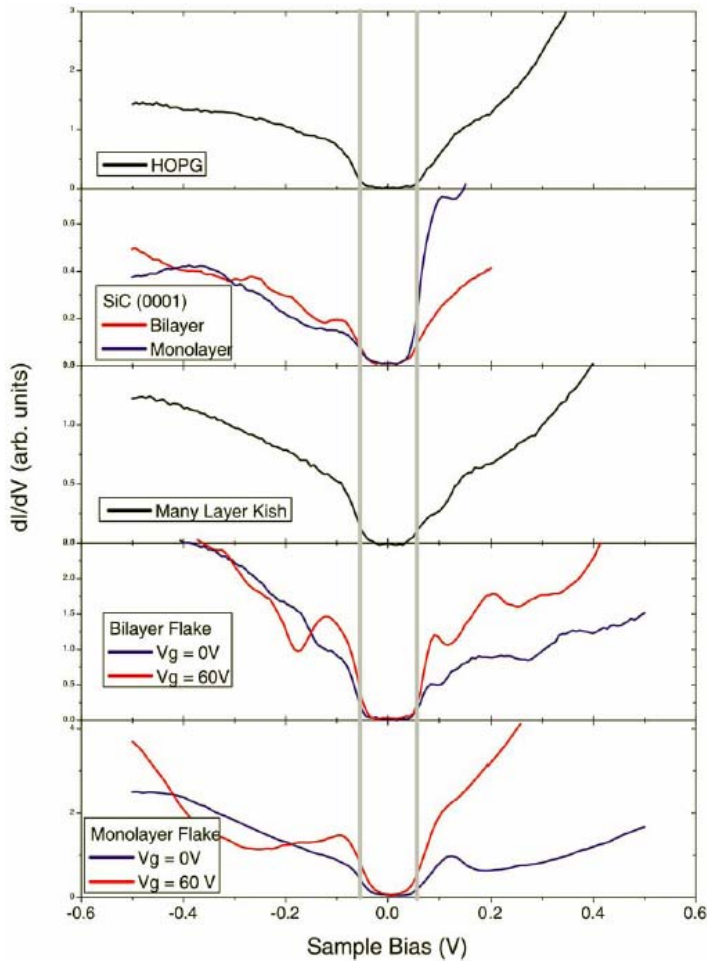


Figure 4-20 – STS dI/dV spectra taken from 8 different types of graphitic surfaces. All show the ~ 130 meV gap centered at the Fermi energy.

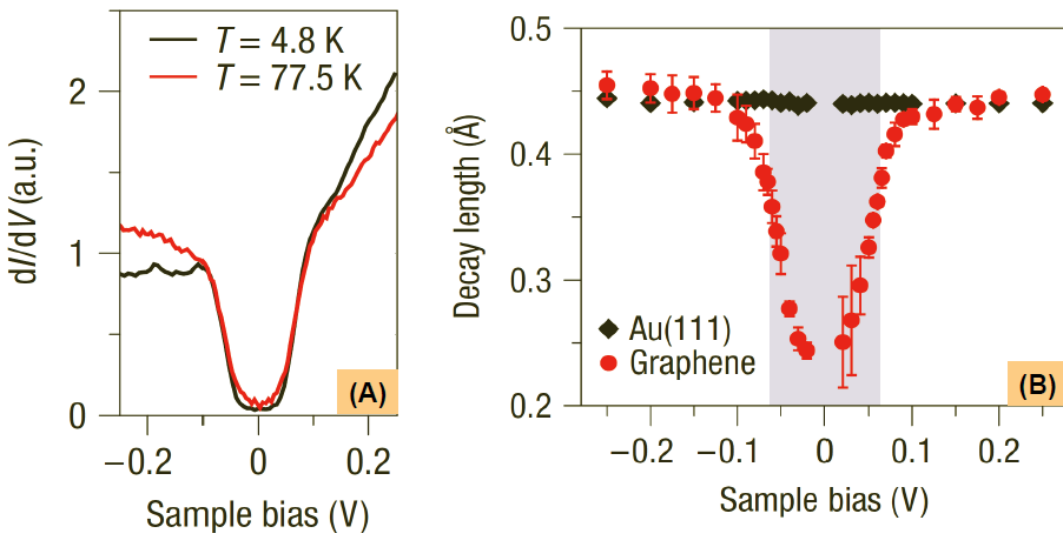


Figure 4-21 – (A) STS dI/dV spectra from a graphene surface at 4.8 K and 77 K, using $V_G = +60\text{V}$. **(B)** The energy-dependent tunneling decay length for graphene and Au(111) extracted from I-Z measurements. (Adapted from [89])

The temperature dependence of the gap-like feature was also measured, as shown in Figure 4-21A for $V_G = +60\text{V}$. As can be seen in this figure, no significant temperature dependence is observed in graphene dI/dV spectra measured at $T = 4.8 \text{ K}$ and $T = 77.5 \text{ K}$.

Finally, the decay length of the tunneling current was probed for energies inside and outside the gap. In order to measure the decay length, the tunneling current was measured as a function of tip-sample separation (z) at constant bias for voltages. When changing the bias, care was taken to ensure that the tip was always starting at the same height above the graphene for all measurements, although this proved to not be necessary. Since the STM tunnel current depends exponentially on z as $I \propto e^{-z/\lambda}$, the inverse of the decay length (λ^{-1}) can be obtained by fitting $\ln(I)$ vs. z measurements with linear fits. It was observed that for small tip heights (large I) there was a nonlinearity in the $\ln(I)$ vs. z curve, possibly due to tip sample interaction. For large z , however, there was the expected linear dependence, which was fit to obtain λ^{-1} and is plotted in Figure 4-21B for different tip biases. As seen in this figure, λ^{-1} rises dramatically for tip-sample biases within the energy gap region, indicating that states at those energies decay must slower (i.e. stick further into the vacuum) than states measured at energies outside the gap region, which decay quickly. For comparison, similar bias-dependent inverse decay measurements were performed for many biases on the Au(111) surface, which are also plotted in Figure 4-21B. As can be seen in the figure, λ^{-1} for graphene is comparable to that observed in the Au(111) for biases outside of the gap, but rises to a value nearly twice as large for biases within the gap.

How can we explain this energy gap feature and the V_G -dependent conductance minima at V_D ? A consistent picture emerges if we consider phonon-mediated inelastic tunneling of electrons into the graphene flake accompanied by a strong suppression of elastic tunneling at E_F . In what follows I first make the case for a general inelastic origin of the central gap feature, and then I discuss how the data can be explained by a novel phonon-based inelastic excitation mechanism.

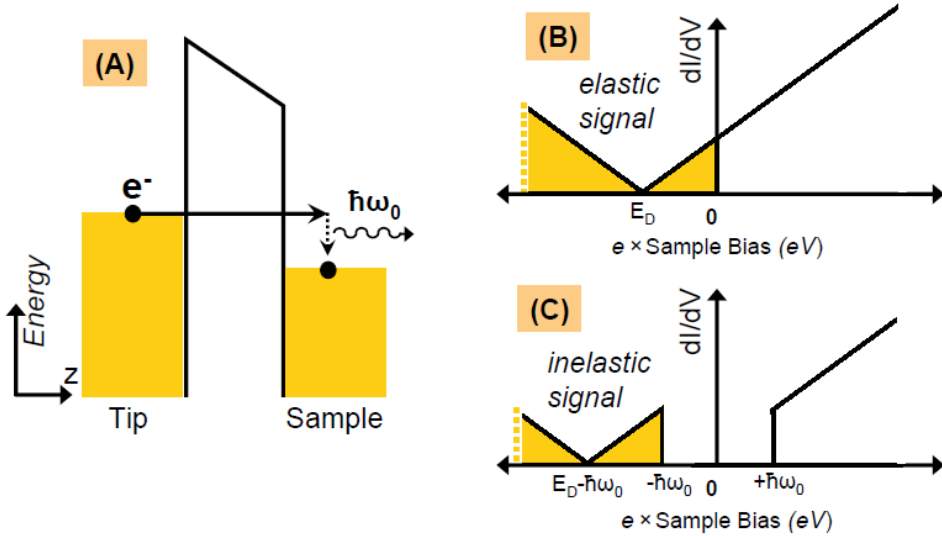


Figure 4-22 – (A) General inelastic tunneling process showing tunneling electron losing energy to some excitation and ending up on some eigenstate of the sample. **(B)** The expected elastic dI/dV tunneling signal of graphene with E_D representing the Dirac point energy. **(C)** The expected inelastic dI/dV tunneling signal of graphene.

STM tunnel current is generally enhanced if the bias voltage is high enough to provide tunneling electrons with enough energy to induce excitations that have some energy $\hbar\omega_0$ [94], as shown in Figure 4-22. In this picture, an electron above the threshold energy has two paths it can take to tunnel into the sample, it can either tunnel straight into the electronic states of the sample (elastic tunneling) or it can tunnel into an excited state of the sample, effectively creating an excitation while entering the sample (inelastic tunneling). In the inelastic case, the tunneling electron loses some of its energy, $\hbar\omega_0$, to the excitation, and thus tunnels into a lower electronic state in the sample. As described earlier, the elastic tunneling conductance simply follows the DOS of the sample, which for graphene is shown in Figure 4-22B. In the inelastic case, however, the tunneling conductance is zero until you are above the threshold energy needed to create the excitation. Once above $\hbar\omega_0$, the tunneling conductance again follows the DOS of the sample, but it appears shifted in energy due to energy lost to the excitation. Thus, the inelastic conductance looks like the DOS of the sample if it had been cut open at the Fermi energy and shifted away from E_F by $\pm\hbar\omega_0$. Figure 4-22C shows how this would look for graphene; there is a gap at E_F with width $2\hbar\omega_0$. If we apply this model to our graphene measurements then we would get that $\hbar\omega_0 = 63 \pm 2$ meV.

Strong evidence for such a dominant inelastic tunneling mechanism in graphene (as opposed to some other gap-inducing mechanism) can be seen in our data by analyzing the gate-voltage dependence of the conductance minimum observed at V_D . If we assume that this minimum arises from inelastic tunneling to the graphene Dirac point (a minimum in the density of states), then its energy location in our data (eV_D) should be offset by $\hbar\omega_0$ from its true energy location, E_D , in the graphene band structure (because each electron loses energy $\hbar\omega_0$ in an inelastic tunneling process):

$$E_D = e |V_D| - \hbar\omega_0 \quad (17)$$

Since V_D depends on gate voltage, this inelastic relation allows us to directly plot E_D versus V_g , as shown in Figure 4-23. Such an identification of the conductance minimum at V_D with the Dirac point energy, E_D , can be checked by fitting this plot with the expected dependence $E_D = \hbar v_F \sqrt{\pi \alpha |V_g - V_0|}$ as prescribed by the graphene linear band structure [95] and using a simple capacitor model. Here v_F is the Fermi velocity of graphene and V_0 is the shift of the Dirac point (in terms of a gate voltage) due to the substrate doping. An excellent fit is obtained with $v_F = 1.10 \pm 0.01 \times 10^6 \text{ ms}^{-1}$ and $V_0 = -4.1 \pm 0.2 \text{ V}$, values that are consistent with previous studies [96, 97]. This unambiguously identifies the observed conductance minimum at V_D as the Dirac point and simultaneously verifies a general inelastic tunneling origin for the central gap feature. Note that if we include the quantum capacitance effects described in Section 4.4.2.1 the fit of the E_D still corresponds well with the position of the Dirac point (using $\Delta\Phi_{\text{tip-graphene}} = -0.05 \text{ eV}$; $d_l = 1 \text{ nm}$).

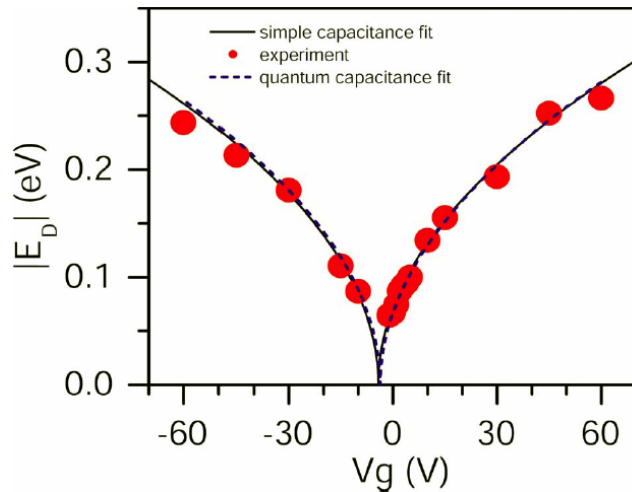


Figure 4-23 – Plot of the absolute value of eV_D vs. applied back-gate voltage. These fitted lines show the expected Dirac point energy using a simple capacitor model as well as taking into account quantum capacitance.

The questions that now arise are: why would the inelastic signal appear so much stronger than the elastic signal, and what specific inelastic excitation are we observing that has $\hbar\omega_0 \approx 63 \text{ meV}$? Typically, the elastic tunneling signal is stronger than the inelastic tunneling signal, since the latter is a second-order process. To understand why the elastic tunneling signal in graphene would appear very weak, recall Section 1.3.3 Eq. (30). This equation shows that for elastic tunneling into Bloch states from an STM tip, the tunneling rate is $\sim \exp[-2(\lambda^2 + k_{||}^2)^{1/2}|z|]$, and thus higher for states with low k -vector, and suppressed for states with high k -vector. For graphene this effect is important

because, as shown in Section 4.2.1, the low energy states of graphene are at the K -point, with a wave vector of 1.7\AA^{-1} . Thus, simple elastic tunnel into graphene is suppressed. Inelastic tunneling, however, does not require the tunneling electron to hop into a ground state of the graphene. A phonon, for example, could mix two eigenstates of the graphene, creating a new state that can be tunneled into inelastically [98]. If this new state had some component with $k = 0 \text{\AA}^{-1}$, then this inelastic tunneling process could be more efficient than the elastic tunneling at $k=1.7\text{\AA}^{-1}$. Figure 4-24 schematically outlines this tunneling mechanism. Here an electron above a threshold energy $\hbar\omega_0$ tunnels into the σ^* -band near the Γ - point ($k=0\text{\AA}^{-1}$) via a virtual transition, before falling into an available K -point state on the π -band by emitting a K' -point phonon (which conserves momentum and energy).

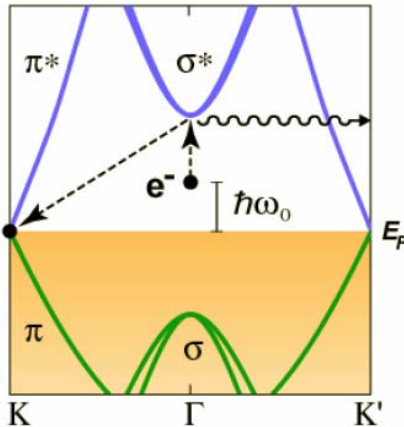


Figure 4-24 – Schematic of inelastic tunneling mechanism for graphene. The tunneling electron goes to the σ -band at the Γ -point via a virtual transition and is scattered back to the Fermi level at the K -point via a K' phonon. (Adapted from [89])

We can now try to figure out what sort of inelastic excitation we are observing, considering it must have $\hbar\omega_0 \approx 63 \text{ meV}$ and a k -vector near the K/K' -point in reciprocal space. Figure 4-25 shows the phonon band structure of graphene. Here we find that there is an out-of-plane phonon mode at the K -point with energy 67meV , and we attribute this phonon to be the source of our inelastic tunneling signal. It is interesting, however, that there are many other K -point phonon modes in the graphene – around 120 and 180 meV – that we do not observe strongly in the tunneling dI/dV signal. The difference is that the 67 meV phonon is an out-of-plane mode, while the higher energy modes are in-plane. Figure 4-26 shows how this difference is important considering how the two modes mix the σ and π -band orbitals. The polarity of the orbitals leads to zero overlap in the case of the in-plane mode, but a finite overlap for the out-of-plane mode.

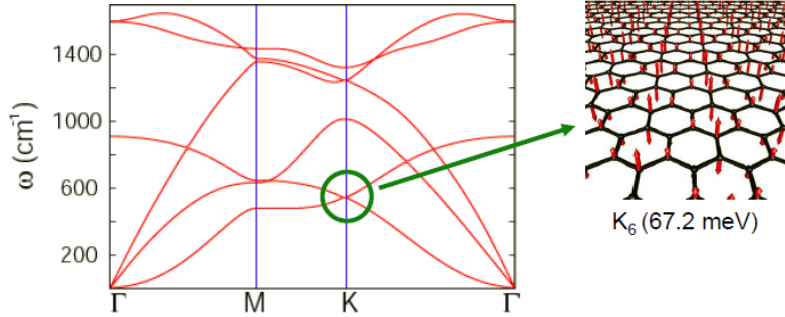


Figure 4-25 – Phonon band structure for graphene showing 3 acoustic and 3 optical branches due to the two atom unit cell. Inset: Out-of-plane K-point phonon at 67 meV (Adapted from [99])

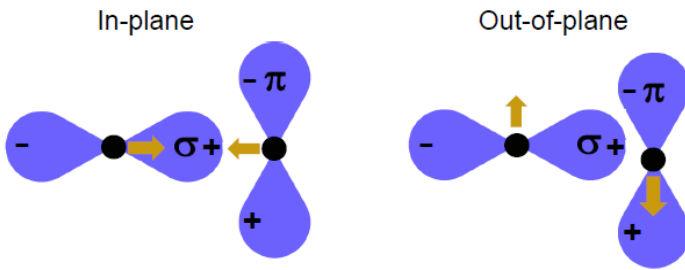


Figure 4-26 – Cartoon showing difference in coupling symmetry between σ -band orbitals and π -band orbitals for in-plane and out-of-plane phonons.

In order to precisely quantify how strong this proposed inelastic tunneling mechanism should be relative to the elastic tunneling, we need to re-evaluate the tunneling Hamiltonian by considering second order processes. In the limit of small tip-sample bias and low temperature, the STM tunneling conductance (Section - 9 -2.1.2, Eq. (23)) can be written as [29]

$$\frac{dI}{dV} = \frac{2\pi e^2}{\hbar} \sum_{\mu\nu} |M_{\mu\nu}|^2 \delta(E_\mu - E_F) \delta(E_\nu - E_F) \quad (18)$$

where $M_{\mu\nu}$ is the tunneling matrix element between initial states $|\mu\rangle$ and final states $|\nu\rangle$. E_μ, E_ν are the energies of the corresponding states and E_F is the Fermi level.

Taking electron-phonon coupling into account, and using a second-quantization formalism, the tunneling Hamiltonian can be written as[100]

$$H_T = \sum_k T_k c_k^+ d_x + \sum_{q,q'} V_{q,q'} c_q^+ c_{q'} (a_{q'-q}^+ + a_{q-q'}) + h.c. \quad (19)$$

where $T_k = Te^{-z/2\lambda}$ with T a constant and $\lambda^{-1} = 2\sqrt{2m\phi/\hbar^2 + k^2}$. c^+ (c) is the sample electron creation (annihilation) operator, d_x is the tip electron annihilation operator, and a^+ (a) is the phonon creation (annihilation) operator. The first term transfers one electron from the tip to the sample and the second term specifies the electron-phonon coupling in graphene.

We first consider the case where electron-phonon coupling does not contribute to the tunneling current, so the tunneling is dominated by the first term in Eq. (19). The initial and final states are $|\mu\rangle = |N_t\rangle |N_s\rangle$ and $|\nu\rangle = |N_t-1\rangle |N_s+1\rangle$,

where N_t and N_s are the number of electrons on tip and sample respectively. The final states have to conserve energy, and so at small bias the electron in the final state is on the Fermi surface, $|N_s+1\rangle = c_{k_F}^+ |N_s\rangle$. Therefore, the tunneling matrix element can be written as

$$M = \sum_k T_k \langle N_s | c_{k_F} c_k^+ | N_s \rangle \langle N_t-1 | d_x | N_t \rangle = T_{k_F} \quad (20)$$

Since k_F is in the close vicinity of the K (or K') point, $k_F/K \rightarrow 1$ and $T_{k_F} \approx T_K$. The tunneling conductance is readily obtained from Eq. (18)

$$\frac{dI}{dV} = \frac{4\pi e^2}{\hbar} T_K^2 \rho_t(E_F) \rho_s(E_F) \quad (21)$$

where ρ_t and ρ_s are tip and sample densities of states respectively. (This is the same result as Section 1.3.2, Eq. [23]).

Next we take into account both terms in Eq. (19) and calculate the matrix element. It is clear that the first order approximation gives the same result as above (Eq. (20)), because the inelastic contribution to the first order is 0. The second order approximation yields the following tunneling matrix (see Ref. [101], for example):

$$M = \sum_m \frac{\langle \nu | H_T | m \rangle \langle m | H_T | \mu \rangle}{E_\mu - E_m} \quad (22)$$

Here the initial states have energy $E_\mu = E_F + \hbar\omega$ with $\hbar\omega$ the phonon energy. The final states are the same as before and the intermediate states are $|m\rangle = c_{k_m}^+ |N_s\rangle$ on the σ^* band, where the electron-phonon coupling is the largest. The energy of the intermediate states is the energy of σ^* band, $E_m = E_{\sigma^*, k_m}$. It can be shown that

$$\langle m | H_T | \mu \rangle = T_{k_m} \quad (23)$$

and

$$\langle \nu | H_T | m \rangle = V_{k_F, k_m} \delta(k_m - k_F - q) \quad (24)$$

Combining Eqs. (5), (6), and (7), we obtain

$$M = \sum_{k_m} \frac{T_{k_m} V_{k_F, k_m}}{E_F - E_{\sigma^*, k_m}} \delta(k_m - k_F - q) \quad (25)$$

Here q is the phonon wavevector and the phonon energy $\hbar\omega$ is neglected in the denominator because $\hbar\omega \ll E_F - E_{\sigma^*, k_m}$. We assume that V_{k_F, k_m} does not strongly depend on wavevector so that we can approximate it with a constant, $V_{k_F, k_m} \sim V_0$. Close inspection of Eq. (25) reveals that the factor $T_{k_m} / (E_F - E_{\sigma^*, k_m})$ falls off rapidly as k_m increases. As an estimate, we approximate it with the function

$$f(k_m) = \begin{cases} \frac{T_0}{E_0} & |k_m| \leq \Theta \\ 0 & |k_m| > \Theta \end{cases} \quad (26)$$

where Θ is the half width at half height of $T_{k_m}/(E_F - E_{\sigma^*, k_m})$ as a function of k_m , and $E_\sigma = E_F - E_{\sigma^*, 0}$ is the energy of the σ^* band at Γ point. We find that $\frac{\Theta}{K} \approx \frac{1}{3}$. The tunneling conductance from Eq. (18) is therefore:

$$\frac{dI}{dV} = \frac{4\pi e^2}{\hbar} \rho_t(E_F) \rho_s(E_F) \sum_q \left(\frac{T_0 V_0}{E_\sigma} \right)^2 \quad (27)$$

where the summation of q runs over shaded area indicated in Figure 4-27, which is 1/7.4 of the total area of the Brillouin zone. Therefore:

$$\frac{dI}{dV} = \frac{4\pi e^2}{\hbar} \rho_t(E_F) \rho_s(E_F) \frac{1}{7.4} \left(\frac{T_0 V_0}{E_\sigma} \right)^2 \quad (28)$$

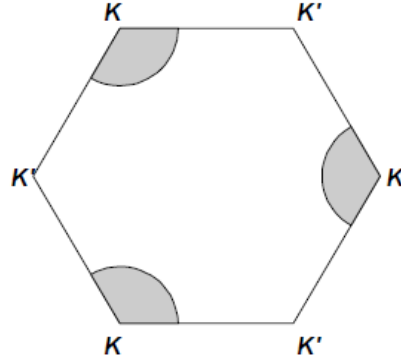


Figure 4-27 - Summation of q . The radius of the circles (Θ) is $\frac{1}{3}K$. The same summation applies symmetrically to K' point.

The ratio of the inelastic tunnel conductance just outside of the energy gap to the elastic tunnel conductance inside of the gap can then be written as

$$\left(\frac{dI}{dV} \right)_{out} / \left(\frac{dI}{dV} \right)_{in} \approx \frac{1}{7.4} \left(\frac{V_0}{E_\sigma} \right)^2 \left(\frac{T_0}{T_K} \right)^2 = \frac{1}{7.4} \left(\frac{V_0}{E_\sigma} \right)^2 \exp[(\lambda_{k/\parallel=0}^{-1} - \lambda_{k/\parallel=K}^{-1})z] \quad (29)$$

Here V_{e-ph} is the effective electron-phonon coupling constant and E_σ is the energy of the intermediate states near the Γ point on the σ^* band ($E_\sigma \sim 4$ eV [102]). If we take the STM tip height as $z \approx 5$ Å (estimated from the tip-sample junction impedance ≈ 2 GΩ) and take $V_0 = 0.5$ eV (a theoretically determined value for the electron-phonon coupling strength [103]) then we obtain $(dI/dV)_{out} / (dI/dV)_{in} \approx 22$, which is of the same order as the measured ratio of 13. This rough agreement lends support to our inelastic model. It should be emphasized, however, that this can only be taken as a rough estimate since

(29) has a strong exponential dependence on the *absolute* tip-height above graphene, z , which cannot be directly measured.

This unique inelastic mechanism is also strongly supported by our observed wavefunction spatial decay rates shown in Figure 4-21B. Within the observed energy gap (i.e. at energies below the inelastic threshold) electrons tunnel directly into graphene states having large crystal momentum parallel to the surface ($k_{\parallel} = K$ or K'). These states tend to decay rapidly into the vacuum region above the surface, since, as described earlier, their evanescent local density of states (LDOS) falls off as $\exp[-2(\lambda^2 + k_{\parallel}^2)^{1/2}|z|]$. Outside the gap, however, electrons tunnel into graphene bands with small crystal momentum ($k_{\parallel} = \Gamma = 0$) that decay much slower into the vacuum. In Figure 4-21B, we measure the decay rates to be $\sim 0.25 \text{ \AA}^{-1}$ inside the gap (elastic signal) and $\sim 0.45 \text{ \AA}^{-1}$ outside the gap (inelastic signal). This agrees well with the expected decays rates of 0.247 \AA^{-1} for $k_{\parallel} = 1.7 \text{ \AA}^{-1}$ (at the K -point), and 0.455 \AA^{-1} for $k_{\parallel} = 0 \text{ \AA}^{-1}$ (at the Γ -point).

Another way that this proposed inelastic tunneling mechanism could be tested would be to see how the signal ratio inside and outside of gap changes with STM tip height. If Eq. (28) is accurate, there should be a noticeable difference. For graphene on SiO_2 , however, the STM tip height could not be varied appreciably because of the tendency of the graphene to hop onto the STM tip when brought close to the surface. Recently, however, other groups have looked for this effect and observed the gap ratio diminishing as the STM tip is brought closer by increasing the tunneling current [104], which is consistent with Eq. (28)

This phonon-mediated inelastic tunnelling process, which involves momentum conserving virtual transitions between 2D electronic bands, is distinctly different from previously studied inelastic tunneling in single molecules [105, 106] or localized spins [107] where momentum is not a well-defined quantity owing to a lack of translational symmetry (phonon-induced inelastic tunneling in single molecules typically leads to conductivity changes of the order of only 1% in contrast to the factor of 10 seen here [106]). This is also different from band-structure-dependent tunneling in silicon [108] because the wave-vector dependence seen here is a result of inelastic excitations that couple the unique electronic band structure and phonon spectrum of graphene. A recent calculation [98] by Wehling *et al.* confirms this general interpretation through density functional theory. They find significant mixing of the graphene σ and π electron bands due to the out-of-plane phonon mode at K/K' , resulting in a strongly enhanced inelastic electron tunnel current.

4.4.4 Observing many-body effects in graphene via tunneling spectroscopy

4.4.4.1 Introduction

The electronic properties of graphene depend strongly on how its charge carriers interact with different many-body excitations, such as plasmons and phonons. Electron-

hole (el-hole) generation, electron-plasmon (el-pl) interactions, and electron-phonon (el-ph) interactions play a strong role in both renormalizing graphene electronic structure and in creating new inelastic excitation tunneling channels [67, 109-112]. Such effects have been examined previously using angle-resolved photoemission spectroscopy (ARPES) [67] and high-resolution electron energy loss spectroscopy [113] for graphene grown on SiC(0001) substrates. These measurements provide evidence that graphene exhibits band renormalization and anomalous lifetime effects related to el-pl and el-ph interactions, but they suffer from complications and alternate interpretations due to the complex and inhomogeneous SiC(0001) substrate [88, 92]. In order to unravel the influence of many-body effects in graphene it is useful to explore graphene monolayers on alternate substrates, such as SiO_2 , which have different substrate interactions and which can be electrically backgated [55] (thereby allowing graphene charge carrier density to be varied continuously). Scanning tunneling spectroscopy (STS) is a powerful technique for exploring many-body effects in such systems due to its subnanometer spatial resolution, its high energy resolution, its capability for measuring both filled and empty state features, and the ease with which it can be integrated with a tunable gate electrode [87, 114-116].

Here I discuss STS measurements revealing the effects of many-body excitations on the electronic properties of backgated monolayer graphene flakes placed on a SiO_2 substrate [24]. Plasmon and phonon effects are both clearly observed and resolved through the use of gate-tunable changes in graphene charge carrier density, n . Two distinct classes of spectroscopic features are observed as n is varied through application of a backgate voltage, V_g . The first type of feature shifts in energy with varying gate voltage, while the second is gate-independent. *Ab initio* calculations indicate that the first type of feature is due to many-body renormalization of the quasiparticle self-energy, while the second type is caused by inelastic tunneling via phonons. Comparison between theory and experiment allows us to directly resolve the influence of plasmon and phonon excitations on quasiparticle lifetimes in graphene.

4.4.4.2 Many-body effects on graphene STS spectra

In the previous section I already described one way in which a many-body effect could be observed in the graphene STS spectrum. There we saw that the tunneling dI/dV signal was dominated by a strong inelastic signal that we associated with a K -point phonon. Closer inspection of the dI/dV curves in Figure 4-19, however, reveals that they contain additional kinks and steps that cannot be associated with the linear graphene band structure. These could be related to the SiO_2 substrate, or due to additional inelastic signals, or they could be associated with el-el and el-ph interactions which renormalize the graphene band structure away from the simple linear dispersion relation. Here we investigate these extra features in more detail by simultaneously measuring the dI/dV and d^2I/dV^2 signal. In order to measure the d^2I/dV^2 signal precisely we lock-in to the second harmonic of the AC tunneling current.

Figure 4-28A shows a typical dI/dV curve obtained with an applied backgate voltage of $V_g = +20\text{V}$ (the electron-doped regime). In order to better resolve the many-body features in this spectra the second derivative of the tunnel current, d^2I/dV^2 , is also displayed. This shows a number of dips in the filled states ($V_b < 0$) and peaks in the empty

states ($V_b > 0$). The dependence of these features on V_g (i.e. on charge carrier density, n) can be seen in Figure 4-28B. Here two distinct types of behavior are seen, one class of features (tracked with solid colored lines) shift in energy with varying V_g while the other (tracked with dashed colored lines) does not.

Features in d^2I/dV^2 associated with many-body interactions have been previously observed in STS spectra on different surfaces [87, 114, 115, 117, 118], but this is the first time that such STS features have been observed as a function of surface charge carrier density. Here we explain the cause of these features in graphene, including why some features show n -dependence and some do not.

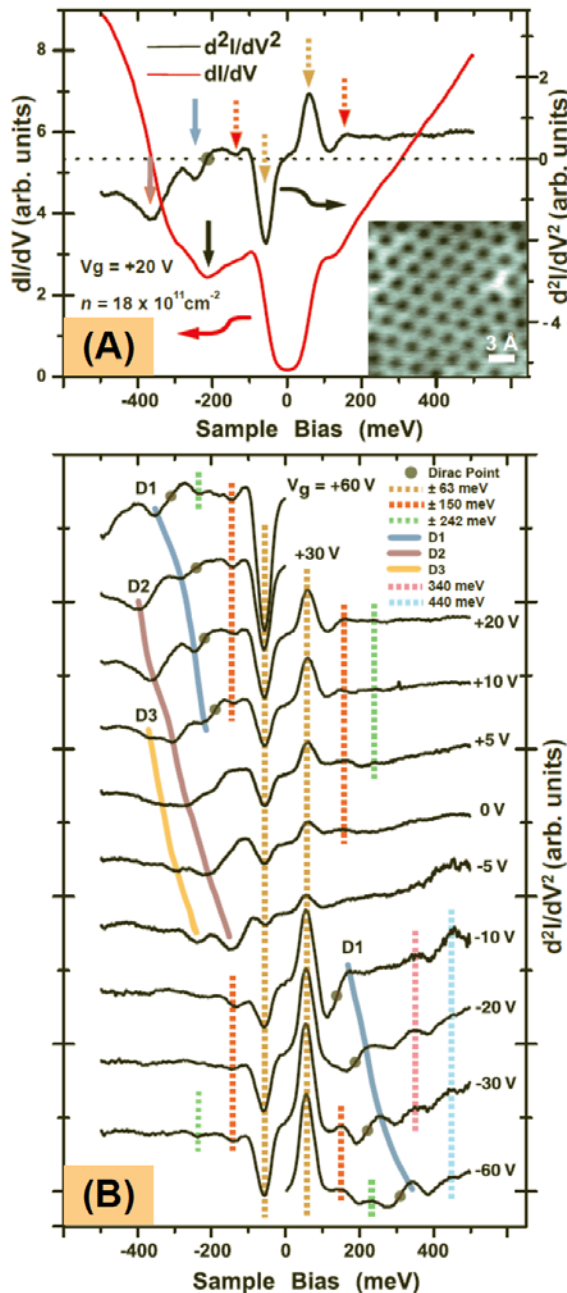


Figure 4-28 – (A) Tunneling dI/dV and d^2I/dV^2 spectra of a monolayer graphene flake on SiO_2 with $V_g = +20\text{V}$, (setpoint parameters: 0.5V, 0.12nA, 4.2 K). Inset shows typical graphene surface where

spectra were obtained. (B) d^2I/dV^2 measurements taken at same point on the graphene surface for different gate voltages (V_g) (junction parameters: ± 0.5 V, 0.12 nA, 4.2 K). Non-carrier-density-dependent features are tracked with dashed colored lines. Carrier-density-dependent features are labeled D1, D2, and D3, and are tracked with solid colored lines.

We first discuss the gate-independent features, which we attribute to phonon-mediated inelastic tunneling. A telltale sign of an inelastic tunneling channel is the presence of anti-symmetric peaks in d^2I/dV^2 on opposite sides of the Fermi energy [116]. Such features can be seen in Figure 4-28B at ± 63 mV, ± 150 mV and ± 242 mV. The 63 mV feature, described in the previous section [89], arises from phonon-mediated inelastic tunneling via a K -point phonon. The new 150 mV feature observed here correlates well in energy with another K -point graphene phonon [119] (as can be seen in Figure 4-25), and so we hypothesize that this feature is also due to a similar inelastic tunneling process.

In order to test this hypothesis we performed a frozen phonon calculation within the framework of density functional theory [120] to determine if the 150 meV K -point graphene phonon could be the cause of this increase in tunnel current. We find that this does indeed occur (i.e., through mixing of the π -bands at the K -point with π and nearly-free electron bands at the Γ -point). Specifically, our results show that for a STM tip $\sim 4\text{\AA}$ above a graphene sheet the inelastic conductance change due to the 150 meV phonon should have a magnitude equivalent to 7% of the inelastic tunneling signal due to the 63 meV phonon. This is consistent with the relative amplitudes of the two features shown in Figure 4-28, thus providing support for an inelastic phonon-based origin of the 150 meV feature. Such an explanation, however, does not easily apply to the 242 meV feature, which has an energy 40 meV higher than the most energetic phonon found in graphene. One possible explanation for this feature is that it arises from multi-phonon processes. It is interesting to compare the spectroscopic features seen here with spectroscopic features seen previously for the surface of bulk graphite. The low-energy feature seen here at 63 meV is similar to features seen in graphite [87, 118, 121], but features with a higher energy magnitude do not compare well.

I now discuss the gate-dependent spectral features (labeled in Figure 4-28B as D1, D2, and D3). Although it is tempting to attribute these to plasmon-assisted inelastic tunneling (since the plasmon energy is dependent on carrier density), this explanation is inconsistent with the fact that they appear only on one side of the Fermi energy for a particular doping. An alternative explanation is that these features arise due to el-pl and el-ph renormalization of the quasiparticle self-energy (i.e., band renormalization effects). Such an explanation would be consistent with recent ARPES experiments [67] and theoretical predictions [109, 110, 112]. To test this idea, we calculated how plasmon and phonon-induced scattering processes influence STM dI/dV spectra, and we compared the results to our experimental data. To do this we used (and expanded upon) a model previously applied to interpret STS spectra of metallic surface states [114].

This model relates the elastic (i.e. renormalized) component of the STM tunneling conductance to the imaginary part of the quasiparticle self-energy ($\text{Im } \Sigma(\varepsilon)$) [114]. In order to derive this relation we first write down the first order tunneling Hamiltonian in a second quantization formalism (just the first term of Eq. (19)):

$$H_T = \sum_k T_k c_k d^\dagger \quad (30)$$

Here T_k is the \mathbf{k} -dependent tunneling matrix element, d^\dagger destroys an electron on the tip, and c_k creates an electron on the sample. Using this Hamiltonian to operate on the ground state of the tip and the sample can give us the tunneling conductance at a particular energy:

$$\frac{dI}{dV}(E) \sim \sum_{n+1, E_{n+1}} \left| \langle \varphi_{n+1} | \sum_k T_k c_k | \varphi_0 \rangle \right|^2 \times \left| \langle \psi_{n-1}^{Tip} | \psi_0^{Tip} \rangle \right|^2 \times \delta(E_{n+1} - E) \quad (31)$$

This can be approximated as:

$$\frac{dI}{dV}(E) \sim \sum_k \sum_{n+1, E_{n+1}} \left| \langle \varphi_{n+1} | T_k c_k | \varphi_0 \rangle \right|^2 \times \delta(E_{n+1} - E) \quad (32)$$

The second summation on the right is, however, simply the spectral function $A(\mathbf{k}, \varepsilon)$ of the sample, so we can rewrite (32) as:

$$\frac{dI}{dV}(E) \sim \sum_k A(k, E) \sim \sum_\varepsilon A(\varepsilon, E) \times DOS(\varepsilon) \quad (33)$$

where the second equality come from approximating the quasiparticle interaction to be independent of \mathbf{k} -direction. From this, we obtain the final expression that we can use to model the STS data:

$$\frac{dI}{dV}_{\text{elastic}}(V) = \frac{C}{\pi} \int \frac{\text{Im} \Sigma(|\mathbf{k}| = \varepsilon / \hbar v_f, \varepsilon)}{(eV - \varepsilon)^2 + \text{Im} \Sigma(|\mathbf{k}| = \varepsilon / \hbar v_f, \varepsilon)^2} DOS(\varepsilon) d\varepsilon \quad (34)$$

Here ε is the graphene quasiparticle energy and $DOS(\varepsilon)$ is the bare graphene density of states, given by $8\pi\varepsilon / \hbar v_f$ (v_f is the Fermi velocity in graphene). C is the bare tunneling matrix element (which includes tip geometry). We assume in the above expression that the spectral density for electronic quasiparticles in graphene, $A(\mathbf{k}, \varepsilon)$, can be approximated by a Lorentzian centered at $\varepsilon = \hbar v_f |\mathbf{k}|$ with a width (FWHM) given by $2 \text{Im} \Sigma(|\mathbf{k}| = \varepsilon / \hbar v_f, \varepsilon)$, and that there is negligible energy dependence in C for the energy range considered. In order to obtain the interacting quasiparticle self-energy, we performed an *ab initio* on-shell calculation for graphene within a GW approximation similar to that in Ref. [110]. Here we model a suspended graphene sheet with appropriate doping and calculate $\text{Im} \Sigma(|\mathbf{k}| = \varepsilon / \hbar v_f, \varepsilon) \equiv \text{Im} \Sigma(\varepsilon)$ along the $K-\Gamma$ direction in reciprocal space (our results are not significantly altered if we use an average of

quasiparticle self energies along the $K-\Gamma$, $K-M$, and $K-K$ directions in reciprocal space). The inset of Figure 4-29A shows the resulting theoretical $\text{Im } \Sigma(\epsilon)$ with separate contributions from el-el interactions (el-hole excitations and plasmons) and el-ph interactions. The green line in Figure 4-29A shows the expected dI/dV signal of an electron-doped graphene sample when no many-body interactions are considered. dI/dV is then simply proportional to the bare (non-interacting) LDOS of graphene, and has a “V” structure that goes to zero at the Dirac point energy (E_D). The blue line in Figure 4-29A shows the theoretical elastic (i.e. renormalized) component of dI/dV when interactions are included through our calculated $\text{Im } \Sigma(\epsilon)$ in Eq.(34). The interacting dI/dV differs from the non-interacting case in two important ways: (1) the dI/dV signal becomes finite at the Dirac point energy and (2) kinks appear in the dI/dV signal that are absent in the bare LDOS for graphene.

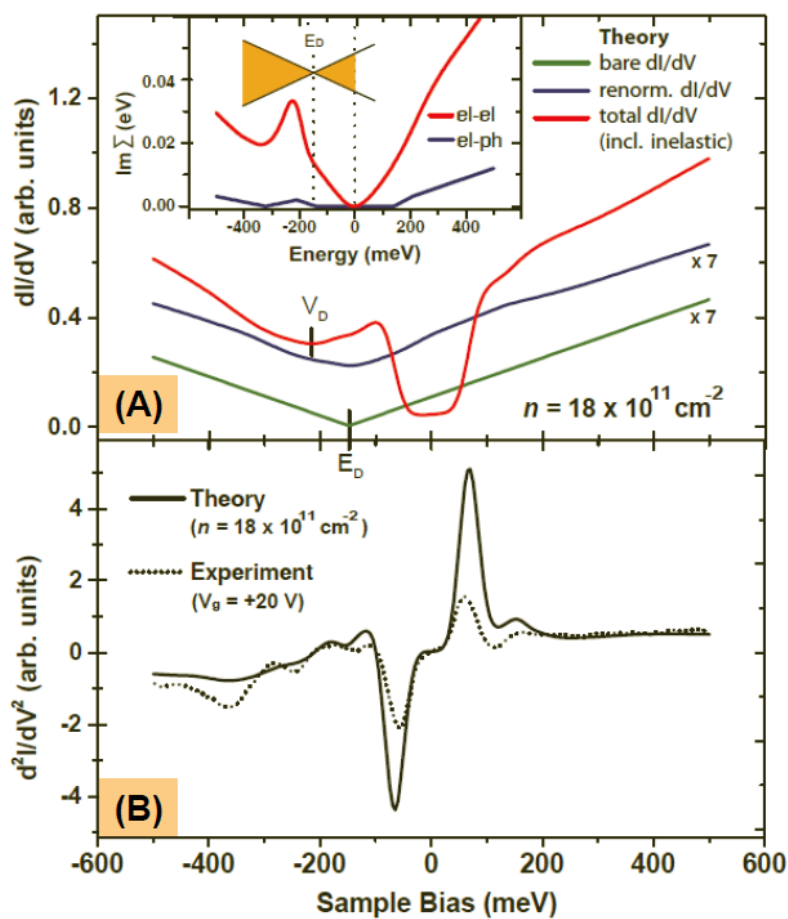


Figure 4-29 - (A) Green line shows theoretical elastic tunneling conductance (dI/dV) of graphene with no many-body interactions present. Blue line shows theoretical elastic component of dI/dV for graphene including many-body interactions. Red line shows total theoretical dI/dV for graphene including both elastic and inelastic tunneling processes. The blue and green curves have been multiplied by a factor of 7 for easier viewing; all three curves share a common origin. Inset: Calculated $\text{Im } \Sigma(\epsilon)$ for graphene quasiparticles along the Γ -K direction due to el-el (red line) and el-ph (blue line) interactions. (B) Solid line shows normalized theoretical d^2I/dV^2 for graphene including both elastic and inelastic processes as in (A). Dotted line shows experimental d^2I/dV^2 measurement of graphene with $V_g = +20\text{V}$ (corresponding to $n = 18 \times 10^{11} \text{ cm}^{-2}$ used in the theoretical calculation).

In order to directly compare the theoretical dI/dV to our experimental results, we must also include inelastic tunneling channels. The effect of inelastic tunneling processes on the tunneling signal is to increase tunnel conductance as follows [122]:

$$\Delta \frac{dI}{dV}_{\text{inelastic}}(V) = \sum_i \frac{\lambda_i}{\sigma_i \sqrt{2\pi}} \left| \int_0^{eV} \frac{dI}{dV}_{\text{elastic}}(eV - \varepsilon) \times e^{-\frac{(\lvert \varepsilon \rvert - \hbar\omega_i)^2}{2\sigma_i^2}} d\varepsilon \right|. \quad (35)$$

Here $\hbar\omega_i$ is the energy of the i^{th} inelastic excitation, σ_i is the energy width of this inelastic feature, and λ_i is the electronic coupling constant to the i^{th} excitation. The net result of inelastic tunneling processes is to add satellites of the elastic signal at voltages $\pm \frac{\hbar\omega_i}{e}$ with respect to E_F [122]. The total dI/dV (shown in red in Figure 4-29A) is simply the sum of the elastic and inelastic components. Over the energy range of our experiment the two most significant inelastic contributions arise from phonon-mediated channels near 63meV and 150meV. For these phonons we use values of λ_i extracted from our frozen phonon calculation described previously [89], while σ_i is determined experimentally to be 17meV for both phonons (σ_i and C [from Eq. (1)] are the only parameters not theoretically determined in this model). Our final theoretical total dI/dV and d^2I/dV^2 curves are shown in Figure 4-29A and B, respectively. For comparison to experiment we have also plotted an experimental d^2I/dV^2 curve with appropriate graphene charge carrier density in Figure 4-29B. The main features seen in the experimental d^2I/dV^2 curve are reproduced in the theoretical curve, although there is some discrepancy in the relative feature magnitudes.

We also compare our experimentally observed d^2I/dV^2 spectra with calculations for many different doping conditions (shown in Figure 4-30). In each case $\text{Im } \Sigma(\varepsilon)$ was calculated as before, and Eqs. (34) and (35) were used to ascertain the resulting d^2I/dV^2 curve. The results of these calculations are shown in Figure 4-30B alongside experimental curves (Figure 4-30A) for corresponding back-gate voltages. Strong qualitative agreement can be seen in the gate dependence of the experimental and theoretical d^2I/dV^2 spectral features.

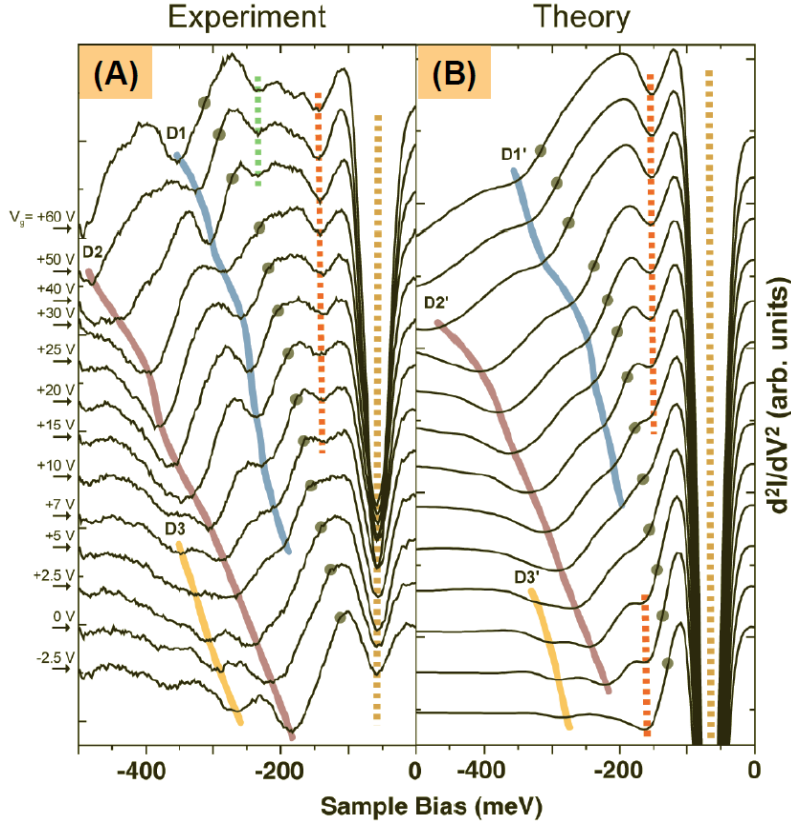


Figure 4-30 - Comparison between (A) experimental and (B) theoretical d^2I/dV^2 vs. sample bias in the filled states of graphene for different gate voltages (V_g) and corresponding electron densities (experimental junction parameters: -0.5 V, 0.12 nA, 4.2 K). Dispersion features D1' and D2' in (B) are known to arise from electron-plasmon interactions, while dispersion feature D3' is known to arise from electron-phonon interactions (dispersion features are tracked with solid colored lines as a guide to the eye). Non-dispersive features in (B) (tracked with dashed colored lines as a guide to the eye) are known to arise from phonon-mediated inelastic tunneling channels. Solid grey dots in (A) mark the position of the Dirac point (V_D) for different gate voltages and in (B) they mark the corresponding electron densities.

Armed with the insights gained through our theoretical modeling, we can now begin to understand the origins of the specific experimental dispersive features displayed in Figure 4-28B and Figure 4-30A. Features D1 and D2 both originate from the anomalous peak in the self-energy of the graphene quasiparticles seen just below E_D in Figure 4-29A inset (red curve). This peak in $\text{Im } \Sigma(\epsilon)$ arises due to plasmons in graphene that strongly scatter holes from below the Dirac point to the upper band, thus drastically reducing the hole lifetime [67, 109, 110, 112]. Feature D3 arises from a minimum in the phonon contribution to the self energy (Figure 4-29A inset, blue curve) in which $\text{Im } \Sigma(\epsilon)$ goes to zero at about 180 meV below the Dirac point. Although phonon related, feature D3 disperses with carrier density because it correlates with the rate that quasiparticles are scattered by phonons to states near the density-dependent Dirac point energy [110].

While the majority of spectral features observed in our data are accounted for within this framework, there are still some mysteries. First, the features observed in our experimental d^2I/dV^2 curves in Figure 4-30A tend to be sharper than the theoretically predicted features in Figure 4-30B. This can be partially explained if graphene

quasiparticles having an overall longer lifetime than calculated in our model. This might arise from structure in the spectral function, $A(\mathbf{k}, \varepsilon)$, not accounted for in our Lorentzian approximation [112]. Second, there are some carrier density independent features that do not correlate with known phonon energies. This includes the previously mentioned non-dispersive feature at $\pm 242\text{meV}$. Perhaps more difficult to explain are the two non-dispersive modes seen at 340meV and 440meV only in the empty states for hole-doped samples. These features do not have anti-symmetric counterparts about E_F and do not obviously correspond to important graphene excitations. The origin of these features is unclear at this time.

4.4.4.3 Conclusion

In conclusion, I have described a number of reproducible many-body features in the d^2I/dV^2 tunneling spectra of graphene [24]. By measuring the carrier density-dependent properties of these features and applying a straightforward theoretical model we are able to distinguish plasmon-related features from phonon-related features, as well as inelastic effects from anomalous lifetime effects.

4.4.5 Charge density fluctuations in Graphene

4.4.5.1 Introduction

In an ideal graphene sheet charge carriers behave as two-dimensional (2D) Dirac fermions governed by the quantum mechanics of massless relativistic particles described in Section 4.2.1 [123, 124]. When placed on an SiO_2 surface, however, the Dirac fermions in graphene are subject to microscopic perturbations that include topographic corrugations and electron density inhomogeneities (i.e. charge puddles). Such perturbations profoundly alter Dirac fermion behavior, with implications for their fundamental physics as well as for future graphene device applications. Topographic corrugations [91, 93], for example, have been suggested as a cause for the suppression of anticipated anti-localization [125]. Electron and hole puddles [97] have similarly been blamed for obscuring universal conductivity in graphene [126]. These issues are part of a puzzle regarding the factors that limit graphene's mobility [127]. In order for graphene to fulfill its promise as a next generation nanodevice substrate it is important to understand the origin of this disorder and the influence it has on Dirac fermions.

In this section I discuss using an STM to spatially map the charge density fluctuations and quasiparticle scattering within a graphene sheet on SiO_2 . By tracking the Dirac point across the graphene surface, it is shown that charge density fluctuations $\sim 4 \times 10^{11} \text{ cm}^{-2}$ occur in the graphene over a lengthscale of 20nm. It is shown that these fluctuations are not caused by topographical corrugations, but rather by charge-donating impurities below the graphene that also backscatter the graphene quasiparticles, inducing standing waves in the graphene. These measurements provide new insight into impurity scattering in graphene and the microscopic mechanisms limiting electronic mobility in graphene devices.

4.4.5.2 Charge puddles and back-scattering in graphene/SiO₂

Figure 4-31A displays the STM topography of a typical 30×30 nm² area of an exfoliated graphene sample on SiO₂. As mentioned in the previous sections, random corrugations with lateral dimension of a few nanometers and a vertical dimension of ~1.5 Å (rms) can be observed, likely due to roughness in the underlying SiO₂ surface and/or intrinsic ripples of the graphene sheet [91, 128]. STM imaging at the atomic scale clearly resolves the graphene honeycomb lattice on top of the broader surface corrugation (inset).

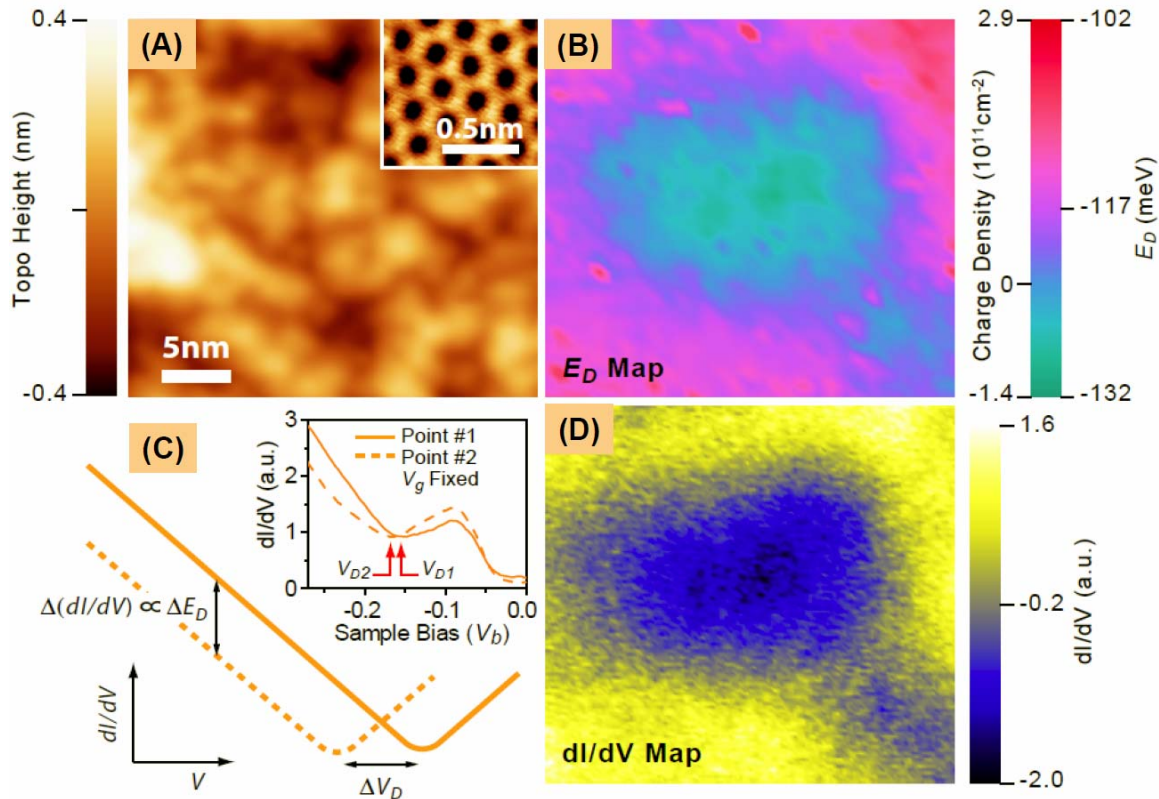


Figure 4-31 - STM topography and charge puddle profile of graphene. (A) STM topograph ($V_b = -0.25$ V, $I = 20\text{pA}$) of a 30×30 nm² patch of graphene resting on a SiO₂ substrate. Inset: Close-up topograph of the graphene honeycomb lattice. (B) Dirac point energy (E_D) map of a single charge puddle lying in the same area shown in (A) ($V_g = 15$ V). This is converted to a local charge density map of graphene (an average background charge density of $0.9 \times 10^{12} \text{ cm}^{-2}$ has been subtracted). (C) Sketch showing how changes in the Dirac point energy (ΔE_D) are proportional to changes in dI/dV signal intensity ($\Delta dI/dV$) at a fixed sample-tip bias. Inset: dI/dV spectra taken at two points separated by 17 nm on a graphene surface. Positional change in Dirac point energy can be seen. (D) Fixed bias dI/dV map over same area as (A) and (B) shows same puddle profile for same V_g .

The inhomogeneous graphene charge density was explored by spatially mapping graphene tunneling spectroscopy features. Graphene tunneling spectra exhibit a dip (local minimum) at a voltage, V_D , outside of the ~126 mV phonon gap feature centered at the Fermi level for slightly doped samples (Figure 4-31C, inset). As discussed in

Section 4.4.3, V_D marks the Dirac point energy, E_D , offset by the energy of a K point phonon mode (~ 63 meV) [89]. Since the Dirac point energy is dependent on the graphene charge density, spatial variation in the measured value of E_D reflects the spatial profile of the charge density fluctuations in graphene (two spectra taken at points separated by 17 nm, for example, are shown in the Figure 4-31C inset). Charge puddles can thus be mapped by measuring the tunnel spectrum at every pixel over a given area and identifying E_D at each point. A Dirac point map, $E_D(x,y)$, can be converted into a charge density map, $n(x,y)$, through the relation given by Eq. (11): $n(x,y) = E_D^2(x,y)/\pi(\hbar v_F)^2$ [129]. Figure 4-31B displays such a map of E_D for the same area shown in Figure 4-31A at an applied gate voltage of $V_g = 15$ V. We clearly resolve 30 meV fluctuations in the Dirac point energy, corresponding to charge density fluctuations of $\sim 4 \times 10^{11} \text{ cm}^{-2}$. A single puddle of electrons having a width of ~ 20 nm can be seen over this area. Integration of $n(x,y)$ over the puddle area yields a total charge inside this puddle of 0.3 ± 0.2 e (the average background charge density has been subtracted).

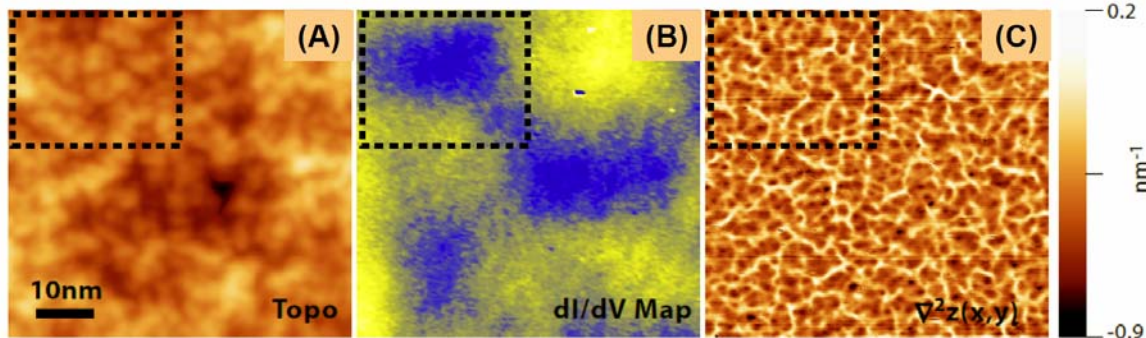


Figure 4-32 - Large area image of graphene topography and charge puddles. (A) $60 \times 60 \text{ nm}^2$ constant current STM topograph of graphene ($V_b = -0.225$ V, $I = 20$ pA). (B) dI/dV map ($V_b = -0.225$ V, $I = 20$ pA, $V_G = 15$ V) taken simultaneously with (A) reveals electron puddles with a characteristic length of ~ 20 nm. (C) Curvature of surface obtained by calculating the Laplacian of the topographic image shown in (A). Upper left dashed boxes indicate the same area shown in Figure 4-31.

Charge puddles can also be probed by spatially mapping the quantity dI/dV for a fixed sample-tip bias held slightly below V_D . This technique significantly reduces data acquisition time and is particularly suited for measuring large graphene areas containing multiple charge puddles. The basis for using this second technique to measure charge puddles is illustrated in Figure 4-31C. In the vicinity of the Dirac point (i.e. V_D) the tunneling conductance, dI/dV , is proportional to the electronic local density of states (LDOS) of graphene [89]. A spatial variation in E_D therefore directly translates into a proportional spatial variation in dI/dV at a fixed bias. dI/dV maps taken at a fixed bias close to V_D can thus produce a map of E_D , up to a multiplicative factor. This is demonstrated by the fixed-bias ($V_b = -0.25$ V) dI/dV map in Figure 4-31D which shows the same charge puddle obtained from direct E_D mapping (Figure 4-31B). Applying this method to a larger area (topography shown in Figure 4-32A), we are able to map the profile of multiple charge puddles as seen in Figure 4-32B. Individual puddles having an

average lateral dimension of $\langle L \rangle \sim 20 \text{ nm}$ are clearly resolved (the electron-rich puddle outlined by a dashed black box is the same as that shown in Figure 4-31B). Such puddles are prevalent in graphene, and we have used this technique to explore 23 electron-rich charge puddles over an area of 23000 nm^2 for three different graphene samples.

The same perturbations that create graphene charge puddles also act as scattering sites for the Dirac fermions in graphene, leading to quasiparticle interference (QPI) patterns [130]. This can be seen in Figure 4-33A which shows a dI/dV map taken with $V_b = 0.35 \text{ V}$ over the same area shown in Figure 4-32A. Standing wave patterns in electronic LDOS having a smaller feature size than the charge puddles are clearly resolved on top of the smooth background provided by the puddle profile shown in Figure 4-32B. Dispersion in the QPI can be seen in Figure 4-33B, C, which show the interference wavelength decrease as sample-tip bias is increased to 0.6 V and 0.85 V respectively ($V_g = 15 \text{ V}$ were fixed for Figure 4-33A-C). We emphasize that the charge puddles are a separate phenomena from the QPI and that their size scale, $\langle L \rangle \sim 20 \text{ nm}$, is unrelated to the energy-dependent QPI wavelength.

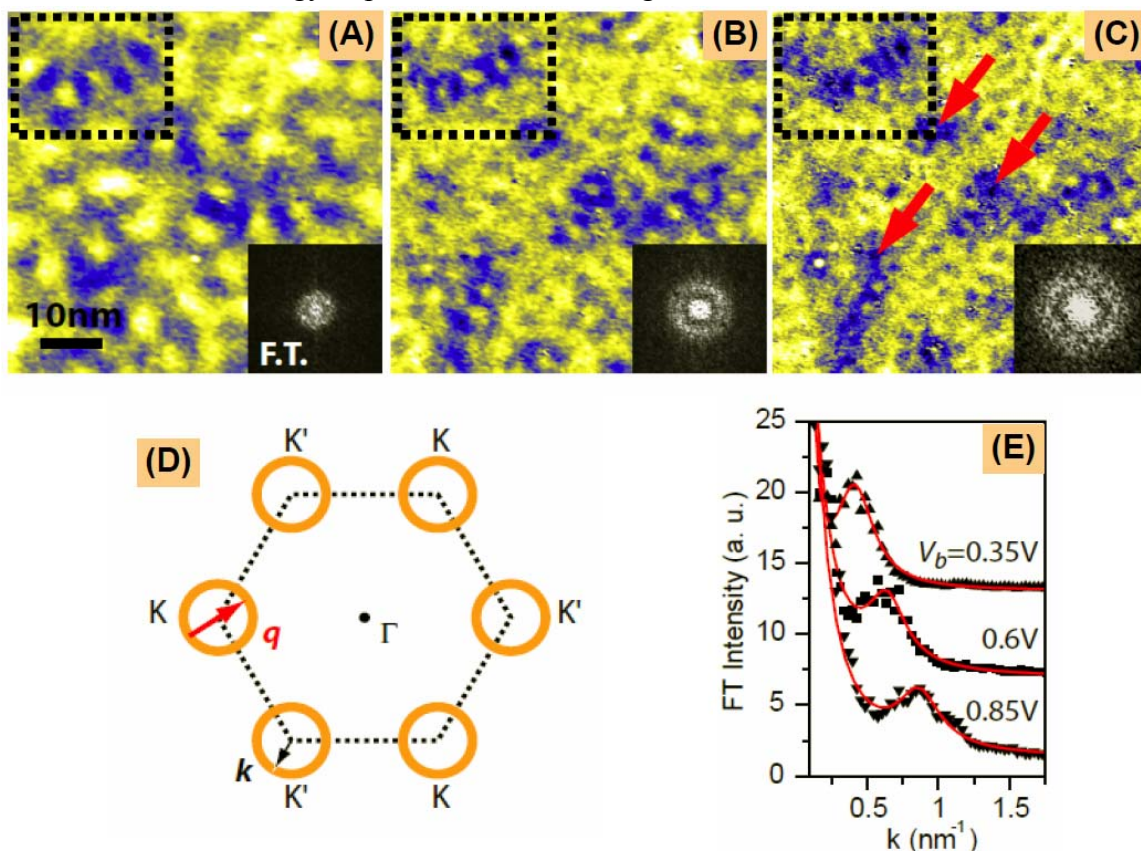


Figure 4-33 - Quasiparticle scattering on a graphene surface. (A-C), dI/dV maps of the same area shown in Figure 4-32 obtained at $V_b = 0.35, 0.6$ and 0.85 V respectively. The tunnel current is held at $I = 50, 60$ and 70 pA respectively and the gate voltage is fixed at $V_G = 15 \text{ V}$ for all three measurements. Lower right insets: 2D Fourier transform of each image. Upper left dashed boxes indicate the same area shown in Figure 4-31. Red arrows in (C) point to localized scattering centers. (D) Schematic of the 2D Brillouin zone of graphene with orange circles indicating constant energy contours for states around the K and K' points near the Fermi energy. The scattering wavevector for an intra-valley back-scattering process is given by q . (E) Radial averaged intensity profiles of the 2D

Fourier transforms shown in (A-C) plotted as a function of k . Red lines indicate Lorentzian fits. Curves are vertically displaced for clarity.

These results raise two fundamental questions: (1) What specifically causes the charge puddles? and (2) how do the graphene fermions scatter from them, thus causing QPI? We now address these questions by first discussing electron scattering from the charge puddles and then by determining the actual origin of the charge puddles (we find it convenient to answer question (2) before answering question (1)).

The observed QPI patterns can be understood as the result of quasiparticle scattering from a disordered potential. This is schematically illustrated in the reciprocal space sketch of Figure 4-33D where constant-energy contours cut through conical graphene bands to produce circles having energy-dependent radius k around the Dirac points at K and K'. Intra-valley scattering processes caused by long-range disorder scatter the electrons across the diameter of a single constant-energy circle via a scattering wave-vector \mathbf{q} (red arrow in Figure 4-33D). This results in $|\mathbf{q}| = 2k$, i.e., electrons are back-scattered. 2D Fourier transforms of the dI/dV maps in Figure 4-33A-C (shown in the insets) convert the observed spatial oscillations to reciprocal space and reveal constant-energy rings of radius $2k$.

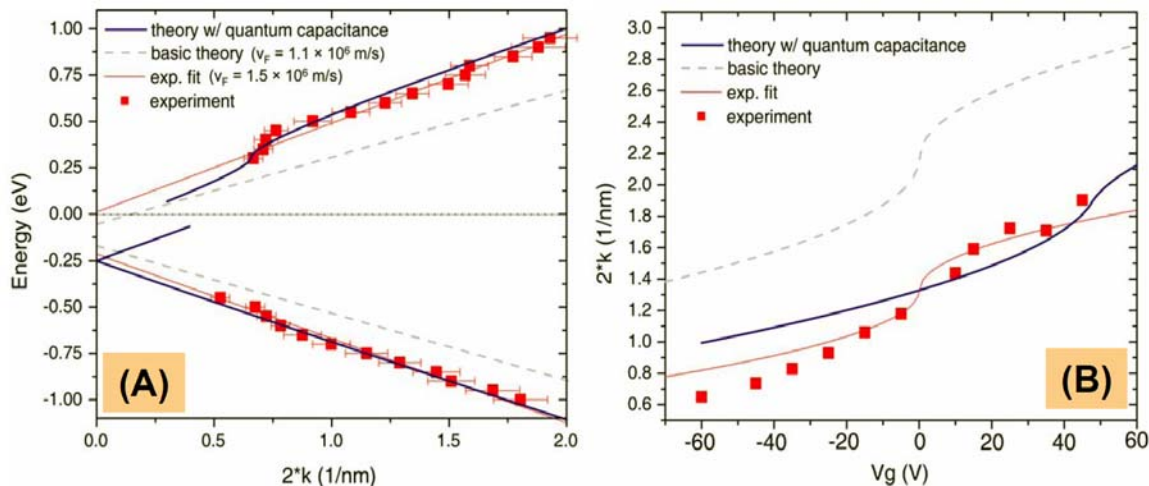


Figure 4-34 – (A) Quasiparticle energy dispersion above and below the Dirac point ($V_D = -0.2$ V, $V_G = 15$ V). Each point is extracted from a Fourier analysis as in Figure 4-33. Solid red lines show fitted linear curves yielding $v_F = 1.5$ and 1.4×10^6 m/s for upper and lower branches. (B) Gate dependence of k as a function of V_g at a constant sample-tip bias of $V_b = 0.75$ V (each point is extracted from a Fourier analyzed dI/dV map). Solid red line shows the calculated dispersion obtained using Eq. (36) and v_F as measured in (A). For both (A) and (B) Grey dashed lines indicate theoretical dispersion for $v_F = 1.4 \times 10^6$ m/s assuming 63 meV offsets due to phonon assisted inelastic tunneling. Blue lines indicates theoretical dispersion relation including quantum capacitance effects, with $\Delta\Phi_{\text{tip-graphene}} = -0.1$ eV, $d_1 = 1$ nm.

Probing the QPI as a function of V_b allows us to map the 2D band structure of graphene [131]. Figure 4-33E shows a radial average of the Fourier transforms in Figure 4-33A-C, and it is clear that the dominant wavevector, $|\mathbf{q}| = 2k$, of the observed QPI (the radius of the ring) varies significantly as a function of V_b . Figure 4-34A plots electron tunnel energy $E = eV_b$ versus $k = q/2$ (red dots) from such analysis and reveals a linear dispersion relation for states above ($eV_b > V_D$) and below ($eV_b < V_D$) the Dirac point

($V_g = 15$ V leads to a fixed $V_D = -0.2$ V for this measurement). Fitting this data with a linear graphene dispersion relation, $E = \hbar v_F k$, we obtain $v_F = 1.5 \pm 0.2 \times 10^6$ and $1.4 \pm 0.2 \times 10^6$ m/s for states above and below the Dirac point, respectively. These values disagree by a significant factor ($\sim 32\%$) from the theoretical value of $v_F = 1.1 \times 10^6$ m/s [129]. A fit using this theoretical factor and considering the inelastic tunneling gap is plotted as a grey dotted line in Figure 4-34A. This seems strange, especially considering that QPI measurements on epitaxial monolayer [132] and bilayer [131] graphene grown on SiC fit well with the expected value of $v_F = 1.1 \times 10^6$ m/s. For an isolated graphene flake on an insulating surface, however, we need to consider the quantum capacitance effects described in Section 4.4.2.1. Namely, Eq. (16) in that section showed that because of shifting in the graphene bands below the STM tip, you do not tunnel into the states in the graphene one might naïvely expect. The blue line in Figure 4-34A shows the dispersion relation we would expect if we include those quantum capacitance effects, using $V_G = +15$ V, $\Delta\Phi_{\text{tip-graphene}} = -100$ meV as the work function difference and $d_1 = 1$ nm as the STM tip height. Note that this curve not only accounts for the steeper linear dispersion, but it fits the “kink” observed at ~ 0.4 eV in the dispersion curve. This correlates with the tip bias where the Dirac point is being pushed across the Fermi energy, and, thus, the graphene is nearly insulating.

The gate-tunability of graphene also provides a unique opportunity to probe the energy dependence of the QPI *without* changing the STM sample-tip bias. QPI patterns obtained in this way for fixed $V_b = 0.75$ V and a changing V_g were Fourier analyzed as above, resulting in a k versus V_g dispersion that is plotted in Figure 4-34B. From the linear band structure of graphene (including the inelastic phonon offset, $\hbar\omega_0 = 63$ meV) we expect this gate-dependent dispersion to have the following form:

$$k = \frac{eV_b - \hbar\omega_0}{\hbar v_F} + \text{sgn}(n)\sqrt{\pi |n|}, \quad n = \alpha(V_g - V_0), \quad (36)$$

where n is the net charge carrier density induced by both the gate (V_g) and the environment (V_0) assuming a simple parallel capacitor model. Here $\alpha = 7.5 \times 10^{10}$ cm $^{-2}$ /V is estimated from the device geometry and $V_0 \approx 0$ V can be obtained from gate-dependent spectroscopic measurement [89]. Using the measured value for v_F obtained from the data in Figure 4-34A, we find that Eq. (36) fits our measured gate-dependent dispersion quite well with no adjustable parameters (Figure 4-34B, solid red line). However, this model did not take into account the quantum capacitance effects. If we consider the quantum capacitance, use the correct value of $v_F = 1.1 \times 10^6$ m/s, and use the workfunction difference and tip height we obtained from the previous fit, we obtain the blue curve in Figure 4-34B, which also lies close to the experimental points. Although this fit is not as good as the one in Figure 4-34A, that could be due to the fact that the tip height changes as the gate is changing. Such a shift in tip height can dramatically alter the band bending below the tip.

One intriguing aspect of our observed QPI is the fact that we see backscattering at all. Theoretical models that take Dirac fermion pseudo-spin into account suggest that

intra-valley backscattering processes are forbidden in monolayer graphene [124, 133] (in sharp contrast to bilayer graphene where intra-valley backscattering processes are allowed [131]). Indeed, intra-valley scattering was recently reported as absent in monolayer graphene epitaxially grown on SiC, and pesudo-spin-suppressed backscattering was provided as an explanation [132]. We note that pesudo-spin-based suppression of backscattering is a first order effect and that backscattering is expected to occur to next leading order. Such hypothetical second-order QPI, however, was shown to lead to a fast decay of the standing waver patterns [134], which is not supported by the clear observation of many oscillations in our data (See Figure 4-33A-C, the oscillation amplitude is $\sim 10\%$ of the total dI/dV signal for all three images). This leads us to speculate that there may be other symmetry-breaking mechanisms at work [135], which certainly deserves further study.

We are now poised to explain the origin of the charge puddles, which is also the origin of the scattering-induced QPI that we observe. We first rule out the hypothesis that topographic corrugations in graphene are a primary cause of the charge puddles. A comparison between the geometry of the charge puddles we observe (Figure 4-32B) and topographic corrugations over the same area (Figure 4-32A) yields no apparent correlation, as the puddles are an order of magnitude larger than the size of the topographic corrugations. We have also computed the curvature of the graphene monolayer characterized by the Laplacian of the topography, $\nabla^2 z(x, y)$. Figure 4-32C shows a map of the curvature over the same surface area as Figure 4-32A. The average feature size in the curvature map is more than an order of magnitude smaller than that of the charge puddles, further ruling out surface corrugation as the cause of the puddles.

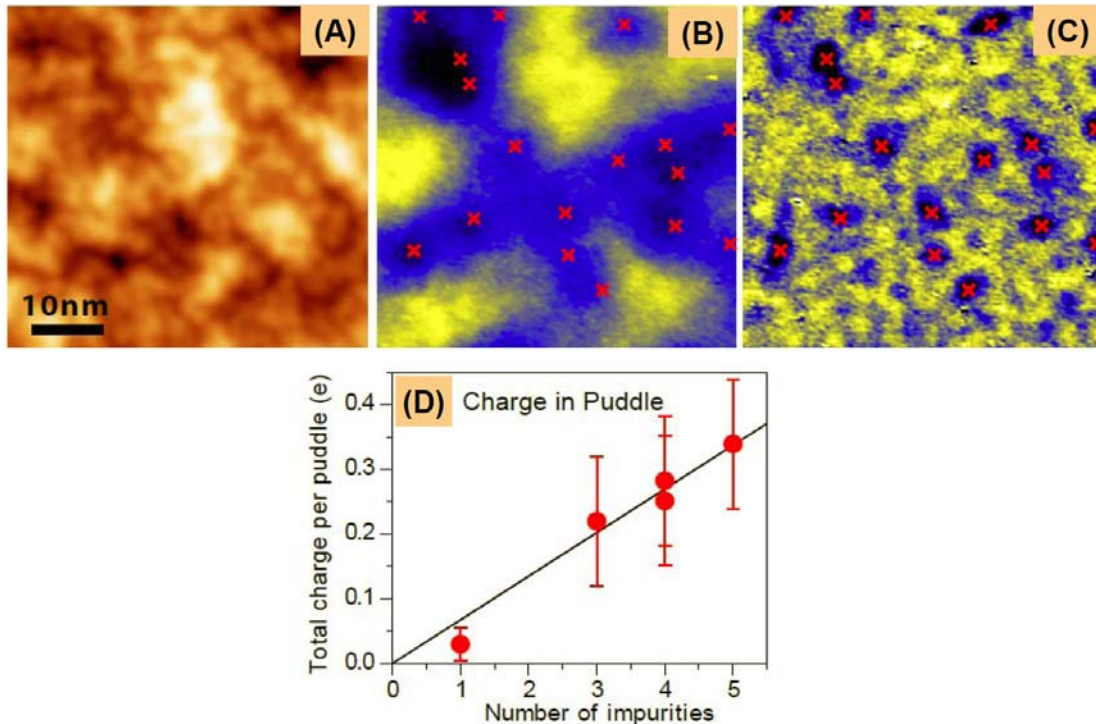


Figure 4-35 - Impurities in Graphene. (A) STM topography of $50 \times 50 \text{ nm}^2$ area of graphene. (B) dI/dV map at bias near Dirac point ($V_b = -0.29 \text{ V}$, $I = 25 \text{ pA}$, $V_G 15 \text{ V}$) shows electron puddles due to charge fluctuations over same region of graphene as (A). Red crosses indicate the location of

quasiparticle scattering center impurities observed in (C). (C) dI/dV map of same area at larger bias ($V_b = 0.75$ V, $I = 80$ pA and $V_G = 60$ V) reveals impurity scattering centers in electron-rich charge density puddles (red crosses). (D) Integrated charge per electron puddle plotted as a function of the number of observed impurities in each puddle (puddles are defined as the electron-rich regions left after subtracting the average background charge density). Linear fit to the data (black line) gives charge per impurity as 0.07 ± 0.03 e (“e” is the charge of an electron).

There is, however, a strong correlation between highly localized features seen in our large bias dI/dV maps and the charge puddles. These localized scattering centers show up as "dots" in the QPI patterns and occur only in electron-rich charge puddles when the electron wavelength is reduced by large bias, as shown by the red arrows in Figure 4-33C. We have observed such localized scattering centers in all of the electron-rich puddles that we have tested. For example, in Figure 4-35A we show STM topography of a different region of the graphene surface that exhibits typical charge puddles in dI/dV maps obtained at sample-tip biases very close to the Dirac point (see Figure 4-35B). When the bias is moved away from the Dirac point, as shown in Figure 4-35C, we clearly see local scattering centers in the electron-rich regions of these charge puddles. Because the scattering centers do not correspond to any clear topographical features, we believe that they arise from individual charged impurities located beneath the graphene. This interpretation is supported by recent experiments on suspended graphene sheets [136].

In order to gain deeper insight into the origin of these subsurface impurities, we performed numerical integration of the charge in five different charge puddles and compared the total amount of charge per puddle to the number of impurities per puddle. In Figure 4-35D we plot the total charge of the puddles as a function of the number of impurities they contain. This data falls roughly on a line, the slope of which allows us to estimate that the average charge contributed by an individual impurity is $\sim 0.07 \pm 0.03$ e. Interestingly, some calculations [137] predict a charge transfer of this order when molecules from air (such as N₂ and H₂O) are physisorbed onto graphene. This finding, combined with the fact that our samples are prepared in ambient conditions, provides further evidence that molecules from air trapped between graphene and the SiO₂ substrate are the likely origin of the charge puddles that we observe in graphene flake nanodevices.

4.4.5.3 Conclusion

This section shows that STM can be used to image the nm-scale charge landscape that the Dirac fermions experience as they move through the graphene. It is shown that, for monolayer graphene placed on SiO₂, charge puddles are induced in the graphene having an average lengthscale of 20 nm arise from charge-donating impurities. Quasiparticle scattering from these charge fluctuations leads to unexpected back-scattering processes that appear to violate pseudo-spin conservation. These findings give new insight into the microscopic processes that limit electron mobility in graphene flakes, and point toward new strategies for improving graphene nanodevice behavior.

4.4.6 STS of adsorbates on graphene

4.4.6.1 Introduction

Graphene impurities provide both a source of mobility-limiting disorder as well as a means to desirably alter graphene electronic structure. Adsorbates on graphene can, for example, induce Coulomb scattering [138, 139], alter electron-phonon interactions [140], shift the chemical potential [138, 139], change the effective dielectric constant [141], and – in cases such as ‘graphane’ [61] – form whole new 2D materials. While these effects have thus far been primarily studied with spatially averaged techniques, understanding the microscopic physics of such behavior requires local-probe exploration of the subnanometer-scale electronic and structural properties of impurities on graphene. Here I describe scanning tunneling microscopy (STM) and spectroscopy measurements performed on individual cobalt (Co) atoms deposited onto backgated graphene devices [26]. It is shown that the electronic structure of Co adatoms can be tuned by application of the device gate voltage, and that the Co atoms can be reversibly ionized. Large screening clouds are observed to form around Co adatoms ionized in this way, and I show that some intrinsic graphene defects also display charging behavior. These results provide new insight into charged impurity scattering in graphene, as well as the possibility of using graphene devices as chemical sensors.

4.4.6.2 Observing Gate-controlled ionization of Co adatoms on graphene using STS

For this study, Co adatoms were first evaporated onto a back-gated graphene/SiO₂ device held inside the STM at 4.2K. Both exfoliated and CVD grown graphene samples were used, with no noticeable difference between the two. Figure 4-36 shows a representative 10×10 nm² STM image of a graphene surface following Co adatom deposition. Co adatoms appear as ~4 Å high dome-like protrusions on the graphene surface (two cobalt adatoms can be seen in Figure 4-36). Two important tests were carried out to ensure that this study was free from erroneous interpretations. First, in order to test for atomic hydrogen contamination in our system (which can lead to dip-like features at the Fermi energy [142]) we also evaporated Co atoms onto a Cu(111) surface. Subsequent dI/dV measurements of 50 Co/Cu(111) adatoms on that surface showed the typical ~5mV wide Kondo feature expected for this system. None of the height abnormalities or spectroscopic artifacts related to hydrogen contamination [142] were observed. Second, after measuring the electronic structure of the Co adatoms on graphene, atomic manipulation was utilized to insure that Co adatoms studied were not bound to defect sites.

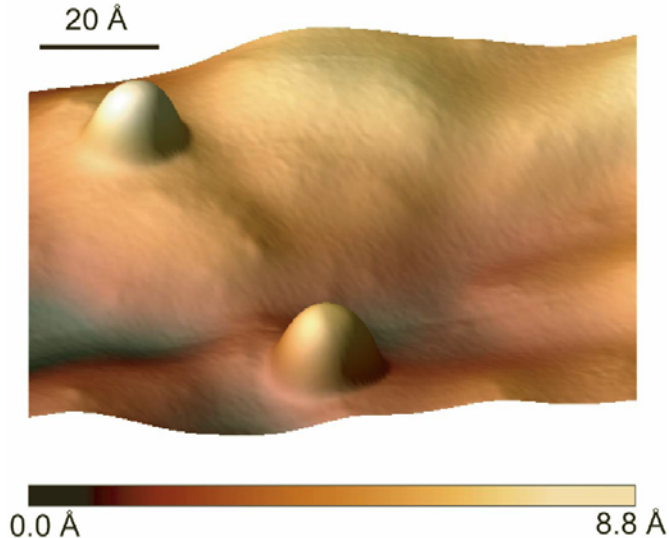


Figure 4-36 - $10 \times 10 \text{ nm}^2$ STM topograph showing two cobalt adatoms resting atop a graphene sheet on a SiO_2 substrate (tunneling parameters: $V_b = -0.25 \text{ V}$, $I = 10 \text{ pA}$, $V_G = 0 \text{ V}$).

dI/dV measurements were performed with the STM tip held over individual Co adatoms in order to measure their energy-dependent local density of states (LDOS). Figure 4-37A shows typical dI/dV spectra obtained from a single Co adatom for different applied back-gate voltages, V_G (changing V_G changes the graphene charge carrier density). Three different types of features are observed in these spectra. The first is a dip observed at the Fermi level (E_F) having a full-width at half maximum (FWHM) of ~ 10 meV (see inset for a higher resolution spectrum). The energy and width of this feature does not vary significantly with V_G . The second feature is a series of resonant peaks in the dI/dV signal marked ‘A’, ‘B’, ‘C’ and ‘D’ in Figure 4-37A. These peaks have a typical FWHM of 25 ± 5 meV. Their behavior differs from the dip at E_F in that their energy locations move in the same direction (and by similar amounts) as the Dirac point voltage (V_D) as V_D is varied by application of V_G (V_D marks the location of a dip seen in the graphene LDOS which is associated with the Dirac point energy [81]). The third feature corresponds to the peak in dI/dV signal marked ‘S’ in Figure 4-37A. The energy of this feature changes as V_G is varied, but it shifts energetically in the opposite direction compared to V_D and disperses significantly faster. Figure 4-37A focuses only on spectra measured for $-60 \text{ V} < V_G < -20 \text{ V}$ since all dispersive features (A, B, C, D, S) shift out of the measurement window ($-0.15 \text{ V} < V_b < +0.15 \text{ V}$) for $-20 \text{ V} < V_G < +60 \text{ V}$. Figure 4-37B summarizes how these spectral features shift in energy as a function of V_G . Also plotted in Figure 4-37B is the gate-dependent variation in Dirac point voltage (V_D) measured on the graphene surface at least 10 nm away from any Co atom.

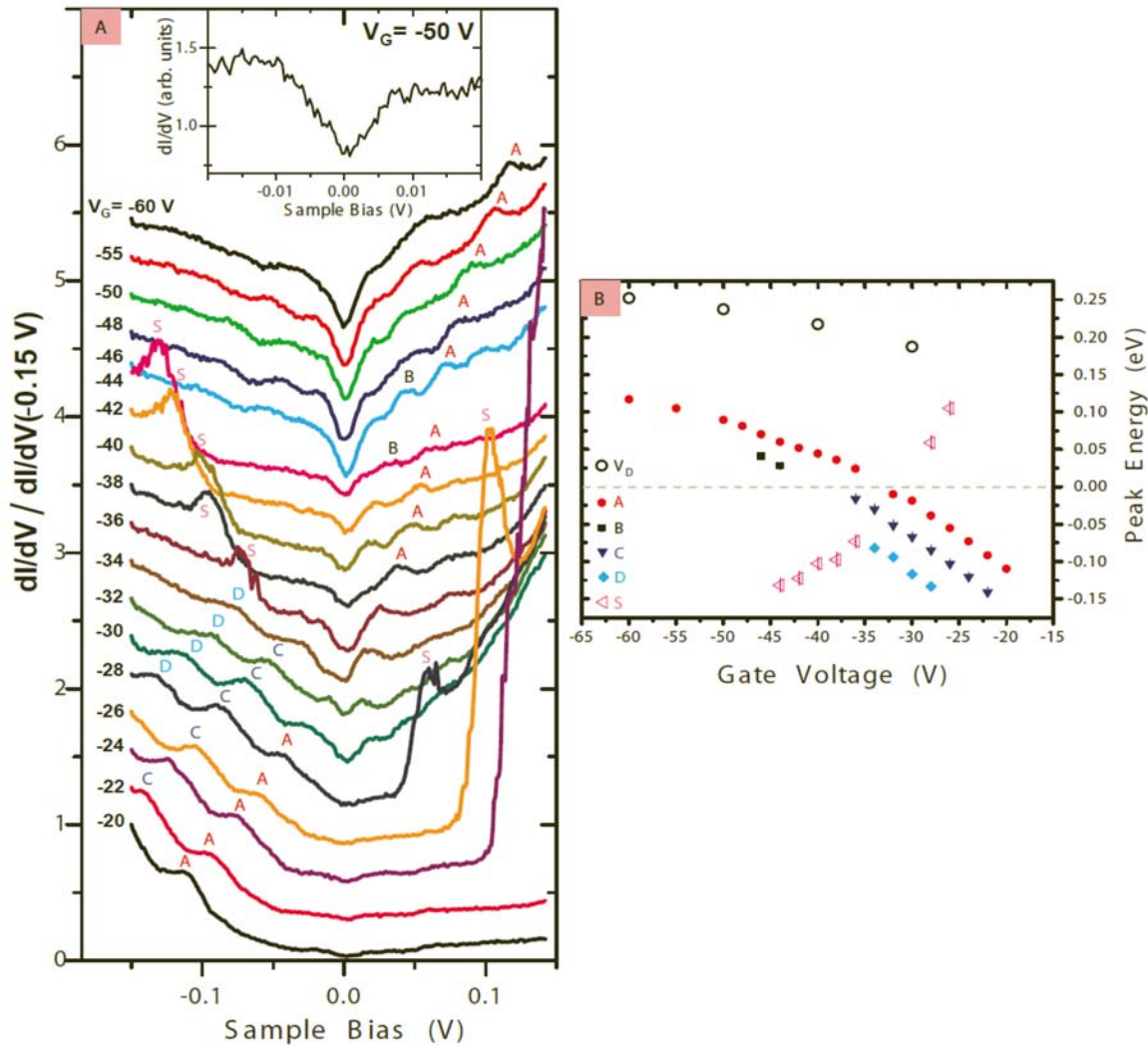


Figure 4-37 - Gate-dependent dI/dV spectra of Co adatom on graphene. (A) dI/dV spectra taken with tip directly above a cobalt adatom on graphene for different back-gate voltages (V_G) (initial tunneling parameters: $V_b = +0.15 \text{ V}$, $I = 22 \text{ pA}$; wiggle voltage $V_{\text{rms}} = 4 \text{ mV}$). Carrier-density-dependent spectral features are labeled ‘A’, ‘B’, ‘C’, ‘D’ and ‘S’. Inset: High resolution dI/dV spectrum of dip-like feature at Fermi level (initial tunneling parameters: $V_b = -0.08 \text{ V}$, $I = 8 \text{ pA}$, $V_G = -50 \text{ V}$; wiggle voltage $V_{\text{rms}} = 1 \text{ mV}$). (B) Gate voltage dependence of dI/dV spectral features observed in (A). Error bars represent uncertainty in the Lorentzian fitting of each spectral feature after a linear background subtraction. Open circles indicate Dirac point voltage (V_D) measured 10 nm from cobalt atom.

In order to better understand how the presence of a Co adatom affects the behavior of graphene, dI/dV measurements were also performed on the bare graphene surface adjacent to a Co adatom. Figure 4-38A shows $dI/dV(V_b)$ and $I(V_b)$ curves measured on graphene $\sim 2.5 \text{ nm}$ away (laterally) from the center of a Co adatom. The dI/dV spectrum shows a $\sim 126 \text{ meV}$ wide gap-like feature at E_F as expected for clean graphene (this is known to arise from inelastic tunneling [81]), but an additional sharp dip is also observed $\sim 220 \text{ meV}$ above E_F . We measured how this new dI/dV feature varies spatially through the use of dI/dV mapping. Figure 4-38B-D show dI/dV maps acquired near a single Co atom with different V_G and V_b . The most striking aspect of these images

is a narrow ring, arising from the spectral dip feature above E_F , that appears centered around the Co adatom. The diameter of this ring is strongly dependent on V_b and V_G . For example, Figure 4-38C,D show the ring diameter increasing as V_G decreases, while Figure 4-38B,D show the diameter increasing as V_b increases.

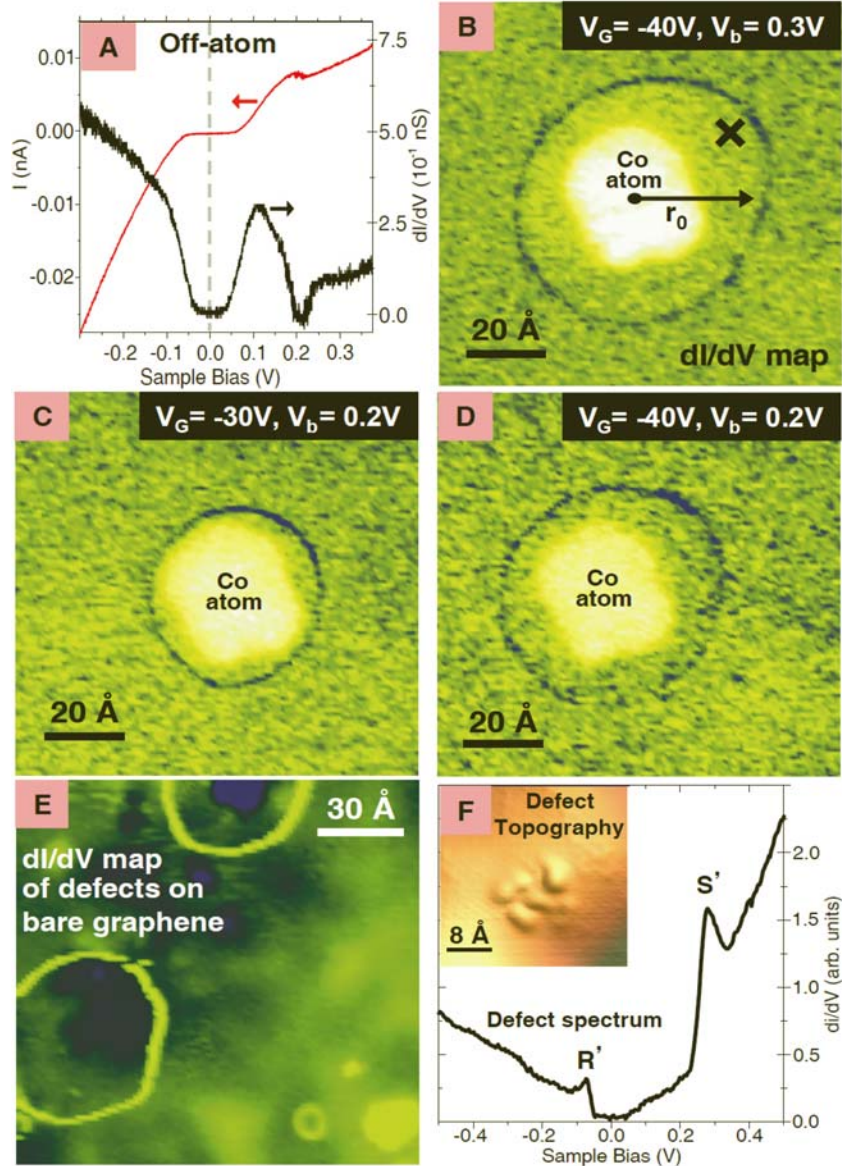


Figure 4-38 - dI/dV conductance measurements of graphene surface near Co adatoms and surface defects. (A) Off-atom dI/dV(V_b) and $I(V_b)$ spectra of graphene surface with tip held a lateral distance $\sim 2.5\text{ nm}$ from the center of a cobalt adatom (initial tunneling parameters: $V_b = +0.4\text{ V}$, $I = 10\text{ pA}$, $V_G = -40\text{ V}$). (B-D), dI/dV maps of a single cobalt adatom and surrounding graphene surface for varying V_b and V_G values. The 'X' in (B) indicates the STM tip position for spectrum shown in (A). (E) dI/dV map of a bare graphene surface (i.e. without cobalt adatoms) that has been annealed at 500 °C in vacuum. Observed ring-like features are centered on defects in the graphene (tunneling parameters: $V_b = +0.7\text{ V}$, $I = 8\text{ pA}$, $V_G = -4\text{ V}$). (F) dI/dV spectrum taken with tip held over defect site found at the center of a defect-induced ring such as those seen in (E). Two prominent features are observed, labeled R' and S' (initial tunneling parameters: $V_b = -0.5\text{ V}$, $I = 5\text{ pA}$, $V_G = -2.5\text{ V}$). Inset: STM topograph of defect site found at the center of a ring-like feature similar to those shown in (E) (tunneling parameters: $V_b = -0.3\text{ V}$, $I = 10\text{ pA}$, $V_G = -60\text{ V}$).

dI/dV maps were also acquired over the bare graphene surface (i.e., in the absence of cobalt adatoms) after annealing to higher temperatures (400–500 °C) as seen in Figure 4-38E. This high annealing temperature tends to introduce defect in graphene/SiO₂ systems. Ring-like features similar to those found around Co adatoms are visible. The inset of Figure 4-38F shows an STM topograph of the center of one of these rings, revealing a defect in the graphene. A dI/dV spectrum taken at the site of such a defect (Figure 4-38F) shows two clear spectroscopic features, R' and S'. R' is observed to disperse in the same direction as V_G when V_G is varied, while S' disperses in the opposite direction. The gate voltage dependence of R' is thus similar to that seen for the Co resonant states A, B, C, D, while the gate dependence of S' is similar to the Co S feature. For fixed V_G, however, the energies of R' and S' (seen for numerous defects) differ from the characteristic energies of the spectral features observed for Co adatoms.

The spectroscopic features we observed for cobalt adatoms and intrinsic graphene defects can be understood within a general impurity physics framework, which I now describe. I start with the dip feature at E_F observed for cobalt adatoms. This is not a conventional band structure feature because it remains pinned to E_F even as E_F is swept through the graphene bandstructure by backgating. One possible origin of this feature is the Kondo effect, which can lead to a resonance at E_F due to spin-screening of a local moment[143]. While cobalt is expected to be magnetic on graphene [144, 145], a Kondo resonance is generally expected to have a strongly gate-dependent width [146], which is not observed here. This opens the possibility that the dip at E_F arises from another origin, such as vibrational inelastic electron tunneling (IET) [11]. As described in Section 4.4.3, IET causes an increase in dI/dV conductance at vibrational energy thresholds for both positive and negative biases, and so can produce dip-like features in dI/dV spectra with a half-width equal to the vibrational mode energy [11]. In order to test this latter possibility, we collaborated with K. Chan and H. Son in Prof. Cohen's group, and they performed *ab initio* calculations of the vibrational energies of a Co adatom on graphene. Those simulations indicated that this system has in-plane vibrational modes of 12 and 27 meV, as well as out-of-plane modes of 17, 40 and 53 meV. The lowest energy mode calculated here is similar in magnitude to the 5 meV half-width of the dip we observe for cobalt adatoms, suggesting a possible IET origin for this experimental feature. It is also interesting to point out that this lowest energy mode is a “marble-in-a-bowl” type mode and could be the reason that the Co adatoms appear dome-like rather than having the typical sharp bump usually observed for adatoms in STM. This observation was pointed out by D. Eigler.

We now turn to the cobalt-induced resonance features marked A, B, C and D in Figure 4-37A,B. We identify these features with the impurity DOS of the combined cobalt/graphene electronic structure because they shift energetically in the same direction as the Dirac point voltage (V_D) as E_F is swept through the graphene bandstructure. Figure 4-39A(i) and B(i) show a sketch of how an impurity-induced DOS feature can be expected to shift as a result of applied gate bias. A likely explanation for these resonances (due to their narrow energy width and spatial localization) is that they arise from a hybridization of cobalt atomic levels with graphene continuum states. Such resonances have been predicted for transition-metal atoms on graphene, [145, 147] but our observed energy level spacings and multiplicity do not precisely match these predictions. A possible explanation for the multiplicity of modes is hybrid electronic-

vibrational (i.e., vibronic) [148] states which are expected to have an energy spacing equal to the energy of a vibrational mode (our experimentally observed energy spacing is on the order of the energies we calculated for the out-of-plane Co/graphene vibrational modes). Lastly I point out that these states might be related to predicted fluctuations in LDOS due to screening of a ‘super-critical’ Coulomb impurity on graphene (i.e. quasi-Rydberg states predicted in an ‘atomic collapse’ scenario) [149].

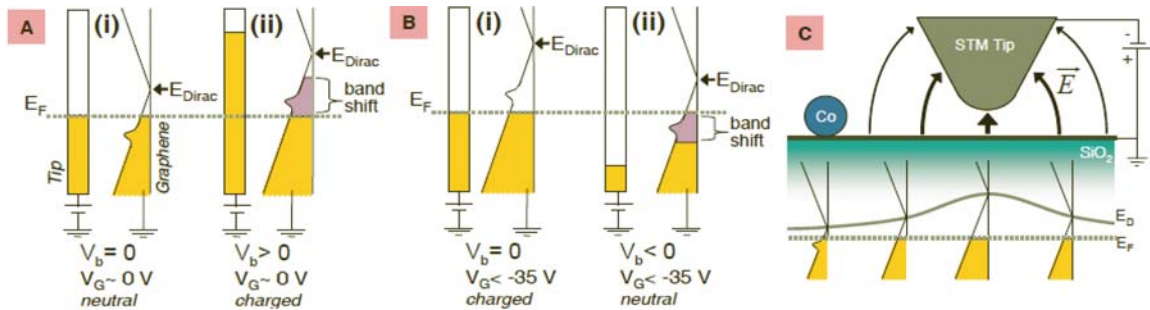


Figure 4-39 - Schematic of tip and backgate-induced ionization of adatom on graphene. (A)(i), For $V_b = 0$ and $V_G \sim 0$ V the adatom impurity DOS feature (i.e., resonance) is below E_F and the adatom is neutral. (A)(ii) When a negative voltage is applied to the STM tip ($V_b > 0$) the graphene bands shift up relative to E_F (i.e. there is a reduction in the local electron density of the graphene). A large enough shift pulls the impurity state above E_F , thus changing the adatom charge state. (B)(i) For $V_b=0$ and $V_G < -35$ V the Co impurity state is above E_F and the Co adatom is charged (ionized). (B)(ii) When a positive bias is applied to the STM tip ($V_b < 0$) the graphene bands shift down relative to E_F . A large enough shift will push the impurity state below E_F , thus returning the cobalt atom to a neutral state. (C) Schematic showing positional dependence of the band-bending induced by an STM tip (considering V_b and workfunction differences). In this figure the Co adatom is neutral, and the gating effect due to the tip at the position of the Co atom is less than in (A,B) where the tip was considered to be directly above the adatom (see Supplementary Materials).

Regardless of their origin, the Co atom DOS features can be either emptied or filled with electrons as they are moved above or below E_F through application of a gate voltage. The energy position of these resonances with respect to E_F determines the ionization state of a Co atom, and the Co ionization state can thus be externally controlled using a gate voltage. This interpretation is supported by the existence of both the S-state and the ring structure surrounding each atom. I first discuss the S-state, which moves opposite in energy compared to both V_D and the resonant peaks when a gate voltage is applied (Figure 4-37A,B). This behavior is the reverse of what is expected for a typical DOS feature, but makes sense in the context of Co atom ionization [150]. Here the application of a tip bias (as well as any difference in tip-sample work functions) causes a local gating of the sample under the tip which is added to the more global gating caused by the backgate electrode, thus inducing the impurity DOS to rise ($V_b > 0$) or fall ($V_b < 0$) with respect to E_F . The Co atom becomes ionized when the tip bias is great enough to cause impurity states to cross E_F , thus creating a screening-induced response in the dI/dV signal (i.e., the S-peak). As shown in Figure 4-39, this mechanism works equally well in the case when the impurity state is placed above E_F by the backgate ($V_G < -35$ V) and when the impurity state is held below E_F ($V_G > -35$ V), except that the S-peak is seen on opposite sides of E_F for these two cases. Such behavior is seen in the data of Figure 4-37A,B where the resonant peaks and S-state lie on opposite sides of E_F and (in the case of state ‘A’) even cross E_F at the same V_G . This ionization framework also explains the

behavior of the R' and S' resonances seen for graphene defects (the R' and S' defect features play the same role as the cobalt A and S features, respectively).

Such ionization behavior can be quantitatively analyzed for our data using a simple double-gate model (i.e., graphene plus backgate plus tip-gate) and accounting for quantum capacitance effects, as described in Section 4.4.2.1. Here we fix the backgate voltage (V_G) and calculate the local band-bending arising from the electric potential difference (as well as the work function difference) between the STM tip and the graphene substrate beneath it (i.e. we calculate the change in the local graphene electronic density due to tip-sample capacitance) [3, 79]. For the case of $V_G = -40$ V we calculate that an applied potential difference of $V_b = -105$ mV will cause impurity ionization for states observed at $V_b = +45$ mV or less (from Eq. (15) and using $\Delta\Phi_{\text{tip-graphene}} = 200\text{meV}$, $d_1 = 6 \text{ \AA}$). This correlates well with our spectroscopy of Co adatoms for $V_G = -40$ V, where we observe an impurity state ('A') at $V_b = +44$ mV and an ionization peak ('S') at $V_b = -100$ mV. Note, however, that $\Delta\Phi_{\text{tip-graphene}}$ and d_1 cannot precisely be known and changing their values by ~30% can easily change the expected threshold of ionization by a factor of 2. Another interesting result of this analysis is that when the STM tip is not atop the Co adatom, the expected gate voltage required to ionize the adatom changes. Thus, while Figure 4-37 seems to indicate that the Co adatoms on graphene ionize at $V_G \sim -35$ V, the actual V_G necessary to ionized the adatoms without the STM tip above them is likely much lower (since the tip tends to hole dope the sample).

The gate-dependent ionization of cobalt atoms also explains the ring structure seen surrounding each atom in dI/dV maps and topography (Figure 4-38). As shown in Figure 4-39C, when the tip is displaced laterally from an atom its electric field can still induce a local gating that shifts cobalt impurity states with respect to E_F , causing ionization (such tip-induced gating has been previously observed in different physical systems [150, 151]). This ionization leads to a change in graphene LDOS surrounding the atom arising from screening charge, and a resulting change in the measured dI/dV at the radius, r_0 , where the ionization takes place. The cobalt atom is ionized when the tip is held at a lateral distance $r < r_0$ for such a bias and gate voltage (i.e., tip inside the ring), whereas for $r > r_0$ the atom is not ionized (i.e., tip outside the ring). The size of r_0 is dependent on V_b , V_G , tip height, and tip shape. For example, if V_G is changed such that the impurity DOS features are further from E_F , then the STM tip will need to be brought closer to the Co adatom to ionize it. This expected behavior corresponds to the experimental behavior shown in Figure 4-38B-D. This type of behavior also explains the appearance of ring structures around graphene defects, as seen in Figure 4-38E,F, indicating that defects can induce localized states (as predicted theoretically [152]) that exhibit gate-induced charging/discharging. Tip-induced ionization rings have previously been seen in systems exhibiting an energy gap (unlike graphene) such as impurities on C_{60} films [150] and dopants in semiconductor systems. [151]

The rings we observe in graphene around cobalt atoms are indicative of a screening cloud that surrounds each charged adatom. We have observed rings with diameters greater than 12 nm (for $V_G < -50$ V), indicating that the screening clouds can be quite large and should likely affect macroscopic transport measurements (charged impurity scattering in general has already been proposed as a major limitation of graphene mobility [138, 153]).

4.4.6.3 Conclusion

This study shows that adatoms, molecules and defects on the graphene surface can become ionized when a back gate voltage is applied to a graphene sheet. The STS measurements here not only allow us to directly observe the localized impurity states and they move across the Fermi energy, but we can see the resulting screening cloud form around the ionized impurity. Thus, this study shows that adsorbates and defects on a graphene surface can essentially become tunable dopants that can be turned on and off. The positioning of localized graphene impurity and defect states either above or below the Dirac point thus can explain asymmetries in graphene electron and hole conduction observed in recent transport measurements [138, 139]. Although often viewed as a problem, such behavior could potentially be used in a graphene chemical sensor. In this scenario, changes in the graphene conductivity at particular back-gate voltages could be correlated with the ionization thresholds of particular chemical species.

REFERENCES

- [1] G. Binnig *et al.*, Helv. Phys. Acta **55**, 726 (1982).
- [2] G. Binnig *et al.*, Physical Review Letters **50**, 120 (1983); J. J. Boland, Physical Review Letters **67**, 1539 (1991); R. M. Feenstra, Physical Review B **44**, 13791 (1991).
- [3] R. M. Feenstra *et al.*, Journal of Vacuum Science & Technology B: Microelectronics and Nanometer Structures **5**, 923 (1987).
- [4] R. M. Feenstra *et al.*, Surface Science **181**, 295 (1987).
- [5] M. F. Crommie *et al.*, 1993), pp. 218.
- [6] S. H. Pan *et al.*, Nature **403**, 746 (2000).
- [7] D. M. Eigler *et al.*, Nature **344**, 524 (1990).
- [8] S.-W. Hla *et al.*, Physical Review Letters **85**, 2777 (2000); R. Yamachika *et al.*, 2004), pp. 281.
- [9] Y. Manassen *et al.*, Physical Review B **61**, 16223 (2000).
- [10] U. Kemiktarak *et al.*, Nature **450**, 85 (2007).
- [11] B. C. Stipe *et al.*, Science **280**, 1732 (1998).
- [12] C. F. Hirjibehedin *et al.*, Science **312**, 1021 (2006).
- [13] R. Wiesendanger *et al.*, Physical Review Letters **65**, 247 (1990).
- [14] M. Julliere, Phys. Lett. A **54**, 225 (1975).
- [15] A. Wachowiak *et al.*, 2002), pp. 577.
- [16] M. Bode *et al.*, Nature **447**, 190 (2007).
- [17] A. Kubetzka *et al.*, Physical Review Letters **94**, 4 (2005).
- [18] L. H. Zhou *et al.*, Nat. Phys. **6**, 187.
- [19] K. S. Novoselov *et al.*, Science **306**, 666 (2004).
- [20] K. S. Novoselov *et al.*, Nature **438**, 197 (2005); Y. Zhang *et al.*, Nature **438**, 201 (2005).
- [21] F. Wang *et al.*, 2008), pp. 206.
- [22] Y. Yayon *et al.*, Physical Review Letters **99**, 067202 (2007).
- [23] Y. B. Zhang *et al.*, Nat. Phys. **4**, 627 (2008).
- [24] V. W. Brar *et al.*, Physical Review Letters **104**, 4 (2010).
- [25] Y. B. Zhang *et al.*, Nat. Phys. **5**, 722 (2009).
- [26] V. W. Brar *et al.*, Nat. Phys., [accepted; DOI: 10.1038/nphys1807; arXiv:1006.1014] (2010).
- [27] J. Bardeen, Physical Review Letters **6**, 57 (1961).
- [28] C. J. Chen, *Introduction to Scanning Tunneling Microscopy* (Oxford University Press, New York, N.Y., 2008).
- [29] J. Tersoff *et al.*, Phys. Rev. Lett. **50**, 1998 (1983).
- [30] I. Horcas *et al.*, Review of Scientific Instruments **78**, 013705 (2007).
- [31] Y. Yayon *et al.*, Physical Review B **73**, 155401 (2006).
- [32] B. E. Kane, Nature **393**, 133 (1998).
- [33] Y. Martin *et al.*, Applied Physics Letters **50**, 1455 (1987).
- [34] D. Rugar *et al.*, Nature **430**, 329 (2004).

- [35] U. Kaiser *et al.*, Nature **446**, 522 (2007).
- [36] M. Bode, Reports on Progress in Physics **66**, 523 (2003); R. Wiesendanger, Reviews of Modern Physics **81**, 1495 (2009).
- [37] P. M. Tedrow *et al.*, Physical Review Letters **26**, 192 (1971).
- [38] S. Heinze *et al.*, Science **288**, 1805 (2000).
- [39] L. Berbil-Bautista *et al.*, Phys. Rev. B **76**, 064411 (2007).
- [40] S. Loth *et al.*, pp. 1628.
- [41] M. Bode *et al.*, J. Vac. Sci. Technol. A-Vac. Surf. Films **15**, 1285 (1997).
- [42] C. Rau *et al.*, Physical Review Letters **47**, 939 (1981).
- [43] J. Delafuera *et al.*, Phys. Rev. B **47**, 13043 (1993); L. Diekhoner *et al.*, Physical Review Letters **90**, 4 (2003).
- [44] O. Pietzsch *et al.*, Physical Review Letters **92**, 057202 (2004).
- [45] O. Pietzsch *et al.*, Physical Review Letters **96**, 237203 (2006).
- [46] P. Ferriani *et al.*, Physical Review Letters **101**, 027201 (2008); F. Meier *et al.*, 2008), pp. 82; A. Kubetzka *et al.*, Phys. Rev. Lett. **94**, 087204 (2005).
- [47] V. Madhavan *et al.*, Science **280**, 567 (1998); J. T. Li *et al.*, Physical Review Letters **80**, 2893 (1998).
- [48] A. J. Heinrich *et al.*, Science **306**, 466 (2004).
- [49] P. Gambardella *et al.*, Science **300**, 1130 (2003).
- [50] G. Kresse *et al.*, Phys. Rev. B **54**, 11169 (1996); G. Kresse *et al.*, Phys. Rev. B **47**, 558 (1993); J. P. Perdew *et al.*, Phys. Rev. Lett. **77**, 3865 (1996).
- [51] L. Niebergall *et al.*, Physical Review Letters **96**, 127204 (2006).
- [52] D. M. Eigler *et al.*, Nature **344**, 524 (1990).
- [53] M. V. Rastei *et al.*, Physical Review Letters **99**, 246102 (2007).
- [54] P. R. Wallace, Physical Review **71**, 622 (1947).
- [55] K. S. Novoselov *et al.*, Science **306**, 666 (2004).
- [56] A. F. Young *et al.*, Nat Phys **5**, 222 (2009).
- [57] L. Ci *et al.*, Nano Research **1**, 116 (2008); H. Hiura, Applied Surface Science **222**, 374 (2004); J. C. Meyer *et al.*, Applied Physics Letters **92**, 123110 (2008); M. Y. Han *et al.*, Physical Review Letters **98**, 206805 (2007).
- [58] A. K. Geim *et al.*, Nature Materials **6**, 183 (2007).
- [59] D. Li *et al.*, Science **320**, 1170 (2008); B. M. Kessler *et al.*, Physical Review Letters **104**, 047001; O. Leenaerts *et al.*, Physical Review B **77**, 125416 (2008); F. Schedin *et al.*, Nature Materials **6**, 652 (2007); S. Stankovich *et al.*, Nature **442**, 282 (2006).
- [60] V. W. Brar *et al.*, Applied Physics Letters **91**, 3 (2007).
- [61] D. C. Elias *et al.*, Science **323**, 610 (2009).
- [62] R. Saito *et al.*, *Physical Properties of Carbon Nanotubes* (Imperial College Press, London, 1998).
- [63] Y. Zhang, in *Physics* (Columbia University, New York, 2006), p. 94.
- [64] D. L. Miller *et al.*, 2009), pp. 924; J. Martin *et al.*, Nat Phys **4**, 144 (2008).
- [65] S. Y. Zhou *et al.*, Nat Phys **2**, 595 (2006).
- [66] S. Reich *et al.*, Physical Review B **66**, 035412 (2002).
- [67] A. Bostwick *et al.*, Nat Phys **3**, 36 (2007).
- [68] M. I. Katsnelson *et al.*, Nat Phys **2**, 620 (2006).

- [69] H. Ohsawa *et al.*, Solid State Communications **61**, 347 (1987); R. C. Tatar *et al.*, Physical Review B **25**, 4126 (1982); A. Bostwick *et al.*, Nature Phys. **3**, 36 (2007).
- [70] T. A. Land *et al.*, Surface Science **264**, 261 (1992).
- [71] M. H. Tsai *et al.*, Physical Review B **45**, 1327 (1992).
- [72] X. Li *et al.*, 2009), pp. 1312.
- [73] A. C. Ferrari *et al.*, Physical Review Letters **97**, 187401 (2006).
- [74] H.-M. Solowan, in *Experimentelle und Angewandte Physik* (Universitat Regensburg, Regensburg, 2010).
- [75] M. F. Crommie *et al.*, Nature **363**, 524 (1993).
- [76] R. Dombrowski *et al.*, Physical Review B **59**, 8043 (1999).
- [77] M. Morgenstern *et al.*, Physical Review Letters **89**, 136806 (2002).
- [78] M. Morgenstern *et al.*, Physical Review Letters **90**, 056804 (2003); M. Morgenstern *et al.*, Physical Review Letters **84**, 5588 (2000).
- [79] S. Luryi, Applied Physics Letters **52**, 501 (1988).
- [80] S. Zhou *et al.*, Chemical Physics Letters **297**, 77 (1998).
- [81] Y. Zhang *et al.*, Nature Physics **4**, 627 (2008).
- [82] M. Green, *Solid State Surface Science* (Marcel Dekker, New York, 1969).
- [83] H. J. Mamin *et al.*, Physical Review B **34**, 9015 (1986); J. J. Paggel, Applied Physics A **59**, 419 (1994); J. M. Soler *et al.*, Physical Review Letters **57**, 444 (1986); E. P. Stoll, Journal of Physics C: Solid State Physics **21**, L921 (1988).
- [84] T. Tiedje *et al.*, Journal of Vacuum Science & Technology A: Vacuum, Surfaces, and Films **6**, 372 (1988).
- [85] J. Yamashita *et al.*, Applied Physics Letters **74**, 2450 (1999).
- [86] N. Agrait *et al.*, Ultramicroscopy **42-44**, 177 (1992); R. J. Colton *et al.*, Journal of Vacuum Science & Technology A: Vacuum, Surfaces, and Films **6**, 349 (1988); H. Kambara *et al.*, Japanese Journal of Applied Physics **45**, 1909; G. Li *et al.*, Nat Phys **3**, 623 (2007); S. Marchini *et al.*, Physical Review B **76**, 075429 (2007); K. Nagaoka *et al.*, Japanese Journal of Applied Physics **45**, L469 (2006); Y. Niimi *et al.*, Physical Review B **73** (2006); G. M. Rutter *et al.*, Science **317**, 219 (2007); O. I. Shklyarevskii *et al.*, Applied Physics A **81**, 1533 (2005); L. Vitali *et al.*, Physical Review B **69**, 121414 (2004).
- [87] D. P. E. Smith *et al.*, Appl. Phys. Lett. **49**, 1641 (1986).
- [88] V. W. Brar *et al.*, Appl. Phys. Lett. **91**, 122102 (2007).
- [89] Y. Zhang *et al.*, Nat Phys **4**, 627 (2008).
- [90] W. Chen *et al.*, Physical Review Letters **80**, 1469 (1998).
- [91] J. C. Meyer *et al.*, Nature **446**, 60 (2007); M. Ishigami *et al.*, Nano Lett **7**, 1643 (2007); E. Stolyarova *et al.*, P Natl Acad Sci USA **104**, 9209 (2007).
- [92] S. Y. Zhou *et al.*, Nat Mater **6**, 770 (2007).
- [93] A. Fasolino *et al.*, Nat Mater **advanced online publication** (2007).
- [94] J. Lambe *et al.*, Phys Rev **165**, 821 (1968).
- [95] P. R. Wallace, Phys Rev **71**, 476 (1947).
- [96] K. S. Novoselov, Nature **438**, 197 (2005); Y. Zhang *et al.*, Nature **438**, 201 (2005); Z. Jiang *et al.*, Phys Rev Lett **98**, 197403 (2007); R. S. Deacon *et al.*, Phys Rev B **76**, 081406 (2007).
- [97] J. Martin *et al.*, arXiv:0705.2180 (2007).
- [98] T. O. Wehling *et al.*, Physical Review Letters **101**, 216803 (2008).

- [99] M. Mohr, Phys. Rev. B **76**, 035439 (2007).
- [100] G. D. Mahan, *Many-particle physics* (Kluwer Academic/Plenum Publishers, New York, 2000), pp. xii.
- [101] J. J. Sakurai *et al.*, *Modern quantum mechanics* (Benjamin/Cummings, Menlo Park, Calif., 1985), pp. x.
- [102] K. Sugawara *et al.*, Phys Rev B **73**, 045124 (2006).
- [103] G. Samsonidze, (Massachusetts Institute of Technology, 2006).
- [104] V. Geringer *et al.*, Applied Physics Letters **96**, 082114.
- [105] J. Lambe *et al.*, Phys. Rev. **165**, 821 (1968).
- [106] B. C. Stipe *et al.*, Science **280**, 1732 (1998).
- [107] C. F. Hirjibehedin *et al.*, Science **312**, 1021 (2006).
- [108] J. A. Stroscio *et al.*, Phys. Rev. Lett. **57**, 2579 (1986).
- [109] E. H. Hwang *et al.*, Phys. Rev. B **77**, 081412 (2008).
- [110] C.-H. Park *et al.*, Phys. Rev. Lett. **102**, 076803 (2009).
- [111] C.-H. Park *et al.*, Nano Letters, published online, (DOI 10.1021/nl902448v) (2009).
- [112] M. Polini *et al.*, Phys. Rev. B **77**, 081411 (2008).
- [113] Y. Liu *et al.*, Phys. Rev. B **78**, 201403 (2008).
- [114] A. Bauer *et al.*, Phys. Rev. B **65**, 075421 (2002); J. Li *et al.*, Phys. Rev. Lett. **81**, 4464 (1998).
- [115] J. Kliewer *et al.*, Science **288**, 1399 (2000).
- [116] B. C. Stipe *et al.*, Science **280**, 1732 (1998).
- [117] L. Bürgi *et al.*, Phys. Rev. Lett. **82**, 4516 (1999).
- [118] L. Vitali *et al.*, Phys. Rev. B **69**, 121414 (2004).
- [119] M. Mohr *et al.*, Phys. Rev. B **76**, 035439 (2007).
- [120] T. O. Wehling *et al.*, Phys. Rev. Lett. **101**, 216803 (2008).
- [121] N. Agraït *et al.*, Ultramicroscopy **42-44**, 177 (1992).
- [122] J. Lambe *et al.*, Phys. Rev. **165**, 821 (1968).
- [123] P. R. Wallace, Phys Rev **71**, 622 (1947).
- [124] T. Ando *et al.*, J Phys Soc Jpn **67**, 2857 (1998).
- [125] S. V. Morozov, Phys. Rev. Lett. **97**, 016801 (2006).
- [126] M. I. Katsnelson *et al.*, Nature Physics **2**, 620 (2006).
- [127] T. Ando, J. Phys. Soc. Jpn. **75**, 074716 (2006); K. Nomura *et al.*, Physical Review Letters **98**, 076602 (2007); E. H. Hwang *et al.*, Physical Review Letters **98**, 186806 (2007); Y. W. Tan *et al.*, Physical Review Letters **99**, 246803 (2007); F. Schedin *et al.*, Nat Mater **6**, 652 (2007); S. V. Morozov *et al.*, Physical Review Letters **100**, 016602 (2008); J.-H. Chen *et al.*, Nature Physics **4**, 5 (2008).
- [128] A. Deshpande *et al.*, arXiv:0812.1073 (2008).
- [129] K. S. Novoselov *et al.*, Nature **438**, 197 (2005); Y. Zhang *et al.*, Nature **438**, 201 (2005).
- [130] Y. Hasegawa *et al.*, Phys. Rev. Lett. **71**, 1071 (1993); M. F. Crommie *et al.*, Nature **363**, 524 (1993); J. E. Hoffman *et al.*, Science **297**, 1148 (2002).
- [131] G. M. Rutter *et al.*, Science **317**, 219 (2007).
- [132] I. Brihuega *et al.*, Phys Rev Lett **101**, 206802 (2008).
- [133] P. L. McEuen *et al.*, Physical Review Letters **83**, 5098 (1999).
- [134] V. V. Cheianov *et al.*, Physical Review Letters **97** (2006).

- [135] T. Pereg-Barnea *et al.*, Physical Review B (Condensed Matter and Materials Physics) **78**, 014201 (2008).
- [136] K. I. Bolotin *et al.*, Solid State Communications **146**, 351 (2008); X. Du *et al.*, Nat Nano **3**, 491 (2008).
- [137] O. Leenaerts *et al.*, Phys Rev B **77** (2008); J. J. Zhao *et al.*, Nanotechnology **13**, 195 (2002).
- [138] J. H. Chen *et al.*, Nat Phys **4**, 377 (2008).
- [139] K. Pi *et al.*, Physical Review B **80**, 075406 (2009).
- [140] J. L. McChesney *et al.*, Physical Review Letters **104**, 136803.
- [141] C. Jang *et al.*, Physical Review Letters **101**, 146805 (2008).
- [142] T. Markus *et al.*, Journal of Physics: Condensed Matter **21**, 053001 (2009).
- [143] J. Kondo, Progress of Theoretical Physics **32**, 37 (1964).
- [144] B. Uchoa *et al.*, Physical Review Letters **101**, 026805 (2008).
- [145] T. O. Wehling *et al.*, Physical Review B **81**, 115427 (2010); M. Yuliang *et al.*, Journal of Physics: Condensed Matter **20**, 115209 (2008).
- [146] D. Goldhaber-Gordon *et al.*, Physical Review Letters **81**, 5225 (1998).
- [147] K. T. Chan *et al.*, Physical Review B **77**, 235430 (2008).
- [148] X. H. Qiu *et al.*, Physical Review Letters **92**, 206102 (2004).
- [149] A. V. Shytov *et al.*, Physical Review Letters **99**, 246802 (2007); V. M. Pereira *et al.*, Physical Review Letters **99**, 166802 (2007).
- [150] N. A. Pradhan *et al.*, Physical Review Letters **94**, 076801 (2005).
- [151] F. Marcinowski *et al.*, Physical Review B **77**, 115318 (2008); K. Teichmann *et al.*, Physical Review Letters **101**, 076103 (2008).
- [152] V. M. Pereira *et al.*, Physical Review Letters **96**, 036801 (2006); T. O. Wehling *et al.*, Physical Review B **75**, 125425 (2007).
- [153] S. Adam *et al.*, Proceedings of the National Academy of Sciences **104**, 18392 (2007).